Stress-strain Response of High-performance Crystalline Aromatic-aliphatic Polyamides

by

Quanpeng Yang

A dissertation submitted in partial satisfaction of the

requirements for the degree of Doctor of Philosophy

in

Mechanical Engineering

at

University of California, Merced

Committee in charge:

Assistant Professor Sachin Goyal, chair
Professor Ashlie Martini, advisor
Assistant Professor Elizabeth Nowadnick
Assistant Professor James Palko

Fall 2022

The dissertation of Quanpeng Yang, titled Stress-strain Response of High-performance Crystalline Aromatic-aliphatic Polyamides, is approved, and it is acceptable in quality and form for publication on microfilm and electronically:

chair _____ Date _____

advisor _____ Date _____

_____ Date _____

_____ Date _____

University of California, Merced

Contents

Contents i

List of Figures iii

List of Tables x

Acknowledgements xi

Curriculum Vita xii

Abstract i

1 Introduction 1
- 1.1 High-performance Polymers . . . 1
  - 1.1.1 Polyamides . . . 2
  - 1.1.2 Aromatic Polyamides . . . 3
  - 1.1.3 Aromatic-aliphatic Polyamides . . . 6
- 1.2 Experimental Methods . . . 6
  - 1.2.1 Processing of Polyamides . . . 6
  - 1.2.2 Experimental Studies on Aromatic-aliphatic Polyamide Crystals . . . 7
  - 1.2.3 Limitations of Experiments on Polyamide Crystals . . . 8
- 1.3 Computational Methods . . . 8
  - 1.3.1 Computational Materials Modeling from First Principles . . . 9
  - 1.3.2 Classical Molecular Dynamics Simulations . . . 10
    - 1.3.2.1 Non-reactive Force Fields . . . 10
    - 1.3.2.2 Reactive Force Fields . . . 11
    - 1.3.2.3 Molecular Dynamics Studies on Aromatic-aliphatic Polyamides 13
    - 1.3.2.4 Limitations of Previous Simulation Studies . . . 14
- 1.4 Dissertation Outline . . . 14

2 Force Field Selection for Molecular Dynamics Simulations of Polyamides 16
- 2.1 Introduction . . . 16
- 2.2 Methods . . . 17

2.2.1 Structural Models . . . 17
2.2.2 Force Fields . . . 22
2.2.3 Simulation Protocol . . . 22
2.3 Results and Discussion . . . 23
2.3.1 Force Field Selection Based on Lattice Parameters . . . 23
2.3.2 Force Field Selection Based on Hydrogen Bonding . . . 24
2.3.3 Force Field Selection Based on Pi-Pi Stacking . . . 26
2.3.4 Force Field Selection Based on Stress-strain Response . . . 27
2.3.5 Force Field Selection Based on XRD Patterns . . . 29
2.4 Conclusions . . . 32

3 Stress-strain Response of PPTA and PAP5 in Chain and Transverse Directions 33
3.1 Introduction . . . 33
3.2 Methods . . . 33
3.3 Results and Discussion . . . 35
3.3.1 Mechanical Properties . . . 35
3.3.2 Chain Direction Strain Response . . . 36
3.3.3 Response to Strain in the Transverse Directions . . . 43
3.4 Conclusions . . . 52

4 Effect of Aliphatic Chain Length on the Stress-Strain Response of Polyamides 53
4.1 Introduction . . . 53
4.2 Methods . . . 54
4.3 Results and Discussion . . . 57
4.3.1 Lattice Parameters of Polyamides before and after Equilibration . . . 57
4.3.2 Explanation of Trend in Low-strain Modulus . . . 57
4.3.3 Explanation of Trend in High-strain Modulus . . . 62
4.3.4 Explanation of Trend in the Transition from Low to High Strain . . . 62
4.3.5 Origin of Odd-even Effect in Stress-strain Response . . . 64
4.3.6 Explanation of Trend in Ultimate Stress . . . 68
4.3.7 Strain Rate Dependence of Stress-strain . . . 70
4.4 Conclusions . . . 73

5 Summary and Future Work 74
5.1 Summary . . . 74
5.2 Effect of Functional Groups on Stress-strain Response . . . 75
5.3 Prediction of Mechanical Properties Using Machine Learning . . . 77
5.4 Concluding Remarks . . . 78

Supporting Information 80

Bibliography 81

List of Figures

1.1 Synthesis of (a) polyamide 6,6 and (b) polyamide 6.[195] Copyright © 2016 by Wiley. 3
1.2 Chemical structures of the most common high-performance polymers.[206] Copyright © 2016 by Nature Portfolio. 4
1.3 Schematic diagram showing the structural modification scenario for reducing the transition temperature and enhancing the solubility of rigid rod-like polymers, such as PPTA.[104] Copyright © 2020 by American Chemical Society 5
1.4 Available elements in the ReaxFF force field. The elements in green are available and those in purple are not yet available[206]. Copyright © 2016 by Nature Portfolio. 11
1.5 ReaxFF development tree, where parameter sets on a common 'branch' are fully transferable with one another. Parameter sets are available in (a) van Duin *et al.* [182], (b) van Duin *et al.* [183], (c) Strachan *et al.* [164, 165], (d) Chenoweth *et al.* [30], (e) Goddard *et al.* [62] and Chenoweth *et al.* [31], (f) Castro-Marcano *et al.* [26] and Kamat *et al.* [85], (g) Vasenkov *et al.* [214], (h) Weismiller *et al.* [193], (i) Mueller *et al.* [121], (j) Agrawalla *et al.* [2], (k) Rahaman *et al.* [145], (l) Monti *et al.* [118], (m) Fogarty *et al.* [57], (n) Raymand *et al.* [148], (o) Pitman *et al.* [140] and Manzano *et al.* [106], and (p) van Duin *et al.* [181] [157]. Copyright © 2016 by Nature Portfolio. 12

2.1 XRD patterns of PPTA from initially-built MD model and experiments. The experimental XRD pattern and the values of the peak angles were taken from Ref. [3, 46, 187] 18
2.2 XRD patterns of PAP5 from initially-built MD model and experiments. The experimental XRD pattern and the values of the peak angles were taken from Ref. [3, 46, 187] 19
2.3 Unit cells of (a) PPTA and (b) PAP5 where lattice dimensions (a, b, and c) are identified on the PPTA snapshot and lattice angles (α, β, and γ) are identified on the PAP5 snapshot. The orthogonal directions (x, y, and z) are also defined with respect to the perspective views of the unit cells. Atom colors correspond to: oxygen, red; nitrogen, blue; carbon, gray; hydrogen, white. The cross-section views on the far right show the crystals from the yz plane. 21
2.4 Comparison of the cumulative error in the lattice parameters for PPTA and PAP5 of seven reactive and two non-reactive force fields. 24

2.5 Comparison of H-bonding (non-bonded, nearest-neighbor N–O) RDFs calculated for (a) PAP5 and (b) PPTA. The reference [46] H-bond lengths (N–O distances) for PPTA and PAP5 are shown as vertical dashed lines. 25
2.6 Comparison of π-stacking RDFs calculated for (a) PAP5 and (b) PPTA. The reference π-stacking distances [46] are shown as vertical dashed lines. 26
2.7 Snapshots of PPTA strained in the z-direction (a) before and (b) after inter-chain slip occurs with the OPLS force field. The black lines connecting aromatic rings highlight the relative positions of chains before and after inter-chain slip. This indicates the sharp drop in stress for some OPLS systems is due to the sudden occurrence of inter-chain slip. The origin of this phenomenon may be that the OPLS force field is less accurate in reproducing the inter-chain distance, i.e., the error in the lattice parameter b for OPLS is larger than that of ReaxFF, as shown in Fig. 2.4. Specifically, the lattice parameter b for OPLS is larger (+0.5 Å) than the experimental value (5.18 Å), while the lattice parameter b for Liu is slightly smaller (–0.14 Å) than the experimental value. 27
2.8 Snapshots of PPTA with the (a) Liu and (b) Vashisth force fields at 8% strain in the z-direction. These figures show that the buckling of the chains in the Liu model is of smaller wavelength than the Vashisth model. In addition, from animations of the Vashisth simulations, it was observed that, starting at ~8% when the buckling occurs, the chains act as springs (alternating contraction and extension), corresponding to the fluctuations in the stress-strain curve in Fig. 2.9b. The origin of this phenomenon may be that the Vashisth force field is less accurate in reproducing the π-stacking interactions, i.e., the error of lattice parameter a for Vashisth is larger than that of Liu, as shown in Fig. 2.4. 28
2.9 Evaluation of the stress-strain curves with the (a) OPLS, (b) ReaxFF Vashisth and (c) ReaxFF Liu force fields for PPTA with simulation box sizes between $1\times1\times1$ and $8\times8\times8$ in x-, y- and z-directions. 29
2.10 XRD patterns of the initially-built structures of PPTA and its structures after equilibration using different ReaxFF force field parameter sets. 30
2.11 XRD patterns of the initially-built structures of PPTA and its structures after equilibration using different ReaxFF force field parameter sets. 31

3.1 Comparison between stepwise stretching and continuous stretching approaches at four different strain rates: (a) 1×10^{8} s^{-1}, (b) 1×10^{9} s^{-1}, (c) 1×10^{10} s^{-1}, and (d) 1×10^{11} s^{-1}. The stress-strain curves obtained from the two approaches are almost the same. The above examples are from simulations of strain of PPTA in the x-direction with the Vashisth force field. 34

3.2 (a) Ultimate stress, (b) failure strain and (c) elastic modulus (calculated from 0 to 2% strain) from simulations of PPTA and PAP5 strained in the chain direction at three different strain rates (1×10^9, 1×10^{10} and 1×10^{11} s^{-1}) using the ReaxFF Liu force field. The error bars reflect the standard deviation calculated from three independent simulations. Also shown are representative data points for PPTA from experiments [28, 38, 49, 99, 147]. 36
3.3 (a-c) Lattice parameters and (d) stress of PAP5 as functions of time during the stretching and relaxation processes. The system was first stretched to 7.5% strain (shaded red) and then allowed to relax by running NPT at 300 K and 1 atm until the system reached 0% strain (shaded blue). The stress and lattice parameters return to their equilibrium values almost immediately after the strain is released. This indicates that the sample is not plastically deformed which indicates that the inflection point (which occurs around 4% strain) is not yield. 38
3.4 Stress-strain behavior (a and b) and RDF profiles and heat maps for H-bonding (c, d, e, and f) and π-stacking (g, h, i, and j) for PPTA (c, d, g, and h) and PAP5 (e, f, i, and j) strained in the x-direction. The RDFs are normalized by the number of bonds per unit cell. Movies S1 and S4 showing the evolution of the stress and RDF distributions as well as the time evolution of the models are available in the Supplemental Information. 39
3.5 Snapshots of (a) PPTA and (b) PAP5 while strained in x-direction with a strain rate of 1×10^9 s^{-1} at 0, 5, 7.5, 10, 12.5 and 20% strains with the Liu force field as viewed from the y-direction. Snapshots correspond to the solid circles on the stress-strain plots in Fig. 3.4. 40
3.6 Position of atoms in the chains projected on the yz plane for (a) PPTA and (b) PAP5, where the centroid of each chain is manually moved to the origin of the yz plane. The hydrogen and oxygen atoms, and the carbon atoms in aromatic rings are excluded in this calculation. 41
3.7 Stress and ring-ring angle as functions of strain in the x-direction for (a) PPTA and (b) PAP5. Ring-ring angle is the average angle between each pair of adjacent rings (the angle between the two green arrows in the inset) from two adjacent sheets. It is a measurement of the coplanarity of rings in the crystal, i.e., smaller angle corresponds to more coplanar. 43
3.8 Stress-strain behavior (a and b) and RDF profiles and heat maps for H-bonding (c, d, e, and f) and π-stacking (g, h, i, and j) for PPTA (a, c, d, g, and h) and PAP5 (b, e, f, i and j) strained in the y-direction. The RDFs are normalized by the number of bonds per unit cell. Movies S2 and S5 showing the evolution of the stress and RDF distributions as well as the time evolution of the models are available in the Supplemental Information. 45
3.9 Snapshots of (a) PPTA and (b) PAP5 while strained in y-direction with a strain rate of 1×10^9 s^{-1} at 0, 5, 7.5, 10, 12.5 and 20% strains with the Liu force field as viewed from the x- and z-directions. Snapshots correspond to the solid circles on the stress-strain plots in Fig. 3.8. 46

3.10 (a) Example snapshots of ring-ring distance before and after slip in the y-direction, (b) ring-ring angle as a quantification of coplanarity of aromatic rings. Slip quantified by ring-ring distance in y-direction, stress, and coplanarity quantified by ring-ring angle as functions of strain in the y-direction for (c) PPTA and (d) PAP5. The slip is quantified as the average distance between each pair of adjacent aromatic rings from two adjacent sheets at each strain with reference to the zero strain. For PPTA, after slip and yield, the chains become more ordered as evidenced by the decrease in ring-ring angle (becoming more coplanar). The structural optimization of PPTA by slip allows subsequent strain hardening. Due to the accommodation of strain by slip, the yield stress of PPTA is lower than that of PAP5. In comparison, slip is not observed for PAP5, therefore the H-bonds accommodate all of the strain resulting in a higher yield stress than PPTA. 47
3.11 Representative snapshot of PPTA strained in the z-direction at 25% strain. Two ring pairs located near peaks (yellow) and between peaks (green) of the buckled chains. The distance between rings at adjacent peaks or valleys of the buckled chains is larger than the equilibrium value, whereas pairs of rings between peaks or valleys have smaller distance than at equilibrium. 48
3.12 RDFs of proximity (a and b) and coplanarity (c and d) of aromatic rings for PPTA (a and c) and PAP5 (b and d). The proximity RDFs are calculated from the distance between every pair of adjacent rings (yellow dotted line in the schematic), and the coplanarity RDFs are calculated from the dihedral angle between every pair of adjacent rings (the angle between the green arrows in the schematic). Smaller proximity and coplanarity are indicators of stronger π-stacking interactions. The results indicate that the ring-ring proximity of PPTA and PAP5 are similar, but PAP5 is more coplanar than PPTA. 49
3.13 Stress-strain behavior (a and b) and RDF profiles and heat maps for H-bonding (c, d, e, and f) and π-stacking (g, h, i, and j) for PPTA (a, c, d, g, and h) and PAP5 (b, e, f, i, and j) strained in the z-direction with Liu force field. The RDFs are normalized by the number of bonds per unit cell. Movies S3 and S6 showing the evolution of the stress and RDF distributions as well as the time evolution of the models are available in the Supplemental Information. 50
3.14 Snapshots of (a) PPTA and (b) PAP5 while strained in z-direction with a strain rate of 1×10^{9} s^{-1} at 0, 5, 7.5, 10, 12.5 and 20% strains with the Liu force field as viewed from the y-direction. Snapshots correspond to the solid circles on the stress-strain plots in Fig. 3.13. 51

4.1 Initial unit cells of (a) PAP5, (b) PAP6, (c) PAP7, (d) PAP8, and (e-f) PPTA. The orthogonal directions (x, y, and z) and lattice constants (a, b, and c) are defined with respect to the perspective view of the PPTA. Atom colors correspond to: oxygen, red; nitrogen, blue; carbon, gray; and hydrogen, white. 56

4.2 (a) Stress-strain curves for 4×4×4 polyamide crystals strained from 0 to 25% strain. The shaded areas reflect standard deviations calculated from three independent simulations. (b) Low-strain and high-strain modulus as functions of the number of non-aromatic carbons in the polymer repeating unit. Low-strain modulus is calculated from the slope of stress-strain curve from 0 to 2% strain. High-strain modulus is calculated from the last 5% strain before failure. Dotted lines are guides to the eye. 58
4.3 Positions of the non-aromatic, backbone atoms in the chains projected on the yz plane, where the centroid of each chain is the origin of the yz plane, for (a) PPTA, (b) PAP5, (c) PAP6, (d) PAP7, and (e) PAP8. Waviness was quantified from the radius of a circle fit to the outline of the 90% innermost non-aromatic carbon atoms and nitrogen atoms. 59
4.4 Waviness of the polymers calculated as the radius of best fit circle (black) and the cross-sectional area of the chains calculated from of the best fit oval (red) of the atom distribution. In both cases, the calculation is based on the positions of the 90% innermost non-aromatic carbon atoms and nitrogen atoms in the yz plane. The error bars reflect standard deviations calculated from three independent simulations. 60
4.5 (a) Positions of atoms in the chains projected on the yz plane for PAP7 as a function of strain, where the origin corresponds to the centroid of each chain. Similar plots for the other polymers are shown in Fig. 4.3. Waviness is quantified as the radius R_0 of a circle encompassing the coordinates of 90% of the inner-most non-aromatic carbon atoms and nitrogen atoms. (b) Low-strain modulus as a function of the waviness at 0% strain. The error bars reflect the standard deviations calculated from three independent simulations. 61
4.6 Stress-strain response of single chain (orange) and crystal (black) forms of (a) PAP6 and (b) PAP7. The single chain is taken from the end of the NPT equilibration simulation of each crystal before stretching. The force per chain is calculated as the total stress multiplied by the cross-sectional area of the simulation box (orthogonal to the strain direction) and then divided by 32 chains for the crystal and 1 for the single chain. Similar trends for PAP5 and PAP8 are shown in Fig. 4.7. The shaded areas reflect standard deviations calculated from three independent simulations. . 62
4.7 Stress-strain response of single chain (orange) and crystal (black) forms of (a) PPTA, (b) PAP5, (c) PAP6, (d) PAP7, and (e) PAP8. The force per chain is calculated as the total stress multiplied by the cross-sectional area of the simulation box (in the strain direction) and then divided by 32 chains for the crystal and 1 for the single chain. The shaded areas reflect standard deviations calculated from three independent simulations. 63
4.8 Representative snapshots of trapezoid and parallelogram structures in the backbones of (a) odd (PAP5) and (b) even (PAP6) polymers and corresponding H-bonds. 65

4.9 Average H-bond length (N-O distance) and inter-chain slip during stretching of (a) PPTA, (b) PAP5, (c) PAP6, (d) PAP7, and (e) PAP8. Data is shown only until failure for each crystal. H-bond length is quantified as the average length of all H-bonds at each strain. Slip is quantified as the change in neighboring ring-ring distance during stretching with respect to 0% strain. Snapshots in (f) show a portion of PAP6 before and after slip occurs. 66
4.10 Stress, inter-chain slip, and dihedral angles as functions of strain of (a) PPTA, (b) PAP5, (c) PAP6, (d) PAP7, and (e) PAP8. Two of the carbons in the NCCC and OCCC dihedrals are aliphatic and one is the amide carbonyl. Data is shown only until failure for each crystal. Illustrations of the ring-ring distance and the dihedral angles are shown in the lower right corner of the figure. The HNCO dihedral angle distributions are similar for the different polymers (158 ± 7°) at low strains. This angle increases slightly with increasing strain before failure, but the change is very small compared to that exhibited by the other dihedral angles (see Fig. 4.7). 67
4.11 Truncated polymer models used to compute the BDE for (a) PPTA and (b) representative aromatic-aliphatic polyamide fragment. X denotes the bond for which the BDE was computed. The gray part of the latter repeat unit was omitted from the DFT calculations because the cleaved bond is not likely to be affected by more distant moieties. 68
4.12 (a) Lattice constant in the H-bonding direction, *b*, for the polymer crystals as a function of strain in the x-direction (chain direction). Data is shown only until failure for each crystal. The shaded areas and errors bars reflect standard deviations from three independent simulations. (b) Ultimate stress and ring-ring angle (averaged over the last 2% before the stress drop for each polymer) as functions of the number of non-aromatic carbons in the polymer repeating unit. The inset schematic defines ring-ring angle. 69
4.13 Stress-strain curves of (a) PPTA, (b) PAP5, (c) PAP6, (d) PAP7, and (e) PAP8 at three different strain rates: 1×10^{8}, 1×10^{9}, and 1×10^{10} s^{-1}. The shaded areas for strain rate 1×10^{9} s^{-1} reflect standard deviations calculated from three independent simulations. Similar trends, including the shoulder at the transition between low and high strain behavior, are observed at all strain rates. The shoulder is more distinct at lower strain rates because the model systems have more time for rearrangements resulting in dihedral angle changes and inter-chain slip. 71
4.14 (a) Low-strain modulus, (b) high-strain modulus, (c) ultimate stress, and (d) ultimate strain of polyamides (PPTA, PAP5 to PAP8) as functions of the number of non-aromatic carbons in the polymer repeating units at three different strain rates: 1×10^{8}, 1×10^{9}, and 1×10^{10} s^{-1}. The error bars at strain rate 1×10^{9} s^{-1} reflect the standard deviation calculated from three independent simulations. Although the ultimate stress and ultimate strain increase with increasing strain rate, consistent with previous studies, [111, 112, 159, 188, 191, 203, 218] the trends with respect to number of non-aromatic carbons are similar at the different strain rates. 72

5.1 Representative chemical structures of polyamides where the X_1 and X_2 can be different functional groups. Different functional groups are expected to have different effects on the mechanical properties of the polyamide. 75
5.2 Potential functional groups in X_1 portion. 76
5.3 Potential functional groups in X_2 portion. 77

List of Tables

2.1 Unit cell lattice parameters for PPTA and PAP5 [46, 134] 19
2.2 ReaxFF parameter sets and the molecular systems for which they were first parameterized are identified by the last name of the first author of the corresponding paper in order of publication date. 22

3.1 Mechanical properties calculated from simulations of strain in the x-direction. For the elastic modulus, low-strain refers to 0-2% strain, high-strain refers to the last 5% strain prior to failure, and all-strain refers to all strain prior to failure. The errors are the standard deviation calculated over three independent repeat simulations. . 37
3.2 Mechanical properties calculated from simulations of strain in the y- and z-directions. 44

4.1 Initial unit cell lattice parameters of the polymers. For PPTA and PAP5, the unit cell lattice parameters were set to match those measured from XRD. [46]. The initial PAP6, PAP7, and PAP8 crystals were created based on the lattice parameters of PAP5 by simply extending the aliphatic chain length and the unit cell in the chain direction (lattice constant c) correspondingly. 57
4.2 Post-NPT unit cell lattice parameters of the polymers. The errors are the standard deviation calculated over three independent repeat simulations. 57

Acknowledgments

First of all, I would like to give my highest respect and gratitude to my advisor Professor Ashlie Martini. She is such a great scientist and educator, who has the wisdom, motivation, and energy to mentor her students and keep them on the right track towards success. The best decision I have made in the past years is to be a student in the Martini group. If someday I will be a professor, I hope I will be as helpful to my students as my advisor Professor Martini has been to me.

I am grateful to my very supportive family especially my father and mother. It is hard for me to imagine the amount of effort they have made for me to have a good education and future. Without the support and understanding from my family, I would not have gone so far regardless how hard I worked. I miss my grandfather who passed away after I just began my Ph.D. journey thousands of miles away from home. Grandfather, you always told me that you had your hope on me. I believe I have not and will never let you down. For the rest of my family, I hope you stay safe and healthy, so I can share more of my time with you.

I would like to thank the former and current members of the Martini group, including Dr. Xiaoli Hu, Dr. Michelle Len, Dr. Arash Khajeh, Dr. Mohammad R. Vazirisereshk, Dr. Azhar Vellore, Dr. Khurshid Ahmad, Dr. Ingrid Padilla Espinosa, Dr. José Cobeña Reyes, Karen Mohammadtabar, Pawan Panwar, Fakhrul Hasan Bhuiyan, Sergio Romero Garcia, Ting Liu, etc. We have benefited so much by learning from each other. I will miss the time we spent together at the meetings, conferences, and parties.

I acknowledge ExxonMobil Research and Engineering Company for financial support of this work as well as for the guidance and brilliant ideas especially from Dr. Wenjun Li, Dr. Spencer T. Stober, Dr. Adam B. Burns, and Dr. Manesh Gopinadhan. This dissertation would not have been possible without the discussions with these experts from ExxonMobil in our monthly meetings for the past three years.

I also acknowledge support for my Ph.D. research from ExxonMobil Research and Engineering Company, the Austrian COMET-Program (Project K2 InTribology1, No. 872176) in collaboration with the Austrian Excellence Center for Tribology (AC2T research GmbH), the National Science Foundation (#CHE 1808213), and the Merced nAnomaterials Center for Energy and Sensing (MACES) supported by the National Aeronautics and Space Administration through grant NNX15AQ01. Simulations were run using the Merced Cluster (by the National Science Foundation Award ACI-1429783), the Pinnacles Cluster (by the NSF-MRI grant #2019144), as well as the Extreme Science and Engineering Discovery Environment (XSEDE, by the National Science Foundation grant ACI-1548562).

Last but not least, I would like to thank Professor Sachin Goyal, Professor Elizabeth Nowadnick, and Professor James Palko for kindly serving as my committee, providing helpful comments and suggestions for my dissertation, as well as escorting me to the final of my Ph.D. journey.

This is not the end but the beginning of a new adventure. I am grateful for having the opportunity to continue exploring on the ocean of knowledge and creativity.

Curriculum Vita

Education

- Ph.D., Mechanical Engineering, University of California, Merced, 2019 to 2022
- M.S., Mechanical Engineering, South China University of Technology, 2017
- B.S., Mechanical Engineering, Guangdong University of Technology, 2013

PROJECTS

Wear Life of MoS_2 at cryogenic temperatures

In collaboration with NASA JPL 07/2022 – 10/2022

- Performed atomic-scale MD simulations to study the wear life and failure mechanisms of MoS_2 dry film at cryogenic temperatures

High Performance Aromatic-aliphatic Polyamides

In collaboration with ExxonMobil 01/2022 – 10/2022

- Performed atomic-scale MD simulations to study the mechanical properties of high-performance polymers PPTA and related aromatic-aliphatic polyamides

Friction of Novel 2D Materials – MXenes

In collaboration with Vienna University of Technology, Austria 04/2021 – 07/2022

- Performed MD simulations to study a new family of 2D materials, MXenes, in terms of their friction and failure mechanisms with different surface terminations

Molecular Dynamics Simulations and Machine Learning for Hydrocarbons

University of California, Merced 01/2022 – 10/2022

- Performed atomic-scale MD simulations for 305 hydrocarbons

- Developed a Python package, PyL3dMD, for descriptors calculation from trajectory output from MD simulations
- Calculated 1444 2D and 156 3D descriptors for these hydrocarbons
- Applied machine learning algorithm to study the temperature dependence of density and viscosity of these hydrocarbons

Atomic-scale Contrast Mechanisms of Super-resolution Atomic Force Microscopy (AFM)

In collaboration with Tao Ye Group at UC Merced 01/2019 – 12/2019

- Combined MD simulations and experiments to study achieve atomic-scale resolution with AFM in water environment

Nanoscale Friction of Hydrophilic and Hydrophobic Self-Assembled Monolayers

In collaboration with Tao Ye Group at UC Merced 01/2019 – 12/2019

- Performed MD simulations and experiments to study the frictional behaviors of self-assembled monolayers (SAMs) with hydrophilic and hydrophobic termination groups

Single Tip Scratching/Indentation Tribometer

George Washington University 01/2018 – 08/2018

- Developed a software in LabVIEW to control the movement of sample platform in x-, y-, and z-directions, as well as data acquisition for pressure and speed

All-weather Chamber

George Washington University 01/2018 – 12/2018

- Developed a software in LabVIEW for instrument operation and data acquisition
- Integrated pressure and temperature sensors, motors, and pumps into the system
- Developed a circuit board for hardware control

Glove Box with Humidity Control

South China University of Technology 06/2015 – 07/2015

- Designed a glove box using AutoCAD for experiments of adhesion force under different humidity constraints
- Coordinated with a manufacturer to manufacture the glove box
- Designed and installed a humidity control system for the glove box.

Handheld Wall Cleaner Design

South China University of Technology 7/2015 – 11/2015

- Designed a novel wall cleaner for bathrooms with power transmitted through a flexible shaft

PTFE-Glass Fiber Composite

South China University of Technology 05/2015 – 08/2016

- Prepared PTFE composite samples with different contents of glass fiber using powder compression molding method
- Performed experiments to study the friction and wear behavior of the PTFE samples sliding against a SiO_2 counterpart

Online Homework System for Mechanical Engineering

South China University of Technology 09/2014 – 06/2016

- Purchased and set up a website server
- Developed a website in ASP for online homework/exam submission and grading
- The system is being used by over 10 colleges for mechanical engineering education

Lubricant Additives Synthesis

South China University of Technology 9/2015 – 01/2017

- Synthesized effective borate lubricant additives to reduce friction and wear
- Experiments were performed to study the improvement of base oils in lubrication performance by the additives

Publications

Refereed Journal Articles

- P Panwar, **Q Yang**, and A Martini. Temperature-Dependent Density and Viscosity Prediction of Hydrocarbons: Machine Learning and Molecular Dynamics Simulations (In preparation)
- P Panwar, **Q Yang**, and A Martini. PyL3dMD: Python LAMMPS 3D Molecular Descriptors (In preparation)
- **Q Yang**, P Grützmacher, S Eder, and A Martini. Effect of Surface Termination on the Balance between Friction and Failure of $Ti_3C_2T_x$ MXenes. (Under review)
- **Q Yang**, W Li, S Stober, A Burns, M Gopinadhan, and A Martini. Effect of Aliphatic Chain Length on the Stress-strain Response of Semi-aromatic Polyamide Crystals. *Macromolecules* 55, 12, 5071-5079, 2022.
- K Ahmad, **Q Yang**, and A Martini. Analysis of Friction Anisotropy on Self-assembled Monolayers Immersed in Water. *Langmuir*. 38, 20, 6273-6280, 2022.
- **Q Yang**, W Li, S Stober, A Burns, M Gopinadhan, and A Martini. Molecular Dynamics Simulation of the Stress–Strain Behavior of Polyamide Crystals. *Macromolecules*. 54, 18, 8289-8302, 2021.
- X Hu, **Q Yang**, W Nanney, T Ye, and A Martini. Simulation of Subnanometer Contrast in Dynamic Atomic Force Microscopy of Hydrophilic Alkanethiol Self-Assembled Monolayers in Water. *Langmuir*. 36, 9, 2240-2246, 2020.
- **Q Yang**, X Hu, W Nanney, T Ye, and A Martini. Nanoscale Friction of Hydrophilic and Hydrophobic Self-Assembled Monolayers in Water. *Tribology Letters*. 68, 1-9, 2020.
- T Lai, Y Meng, **Q Yang**, and P Huang. Evolution and Level Behavior of Adhesion Force by Repeated Contacts of an AFM Colloid Probe in Dry Environment. *The Journal of Adhesion*. 94, 4, 313-333, 2018.
- X Liu, **Q Yang**. A handheld wall cleaner for bathrooms. (Patent No.: ZL 2015 2 1040425.1)
- **Q Yang** and P Huang. Friction and Wear Property of Glass Fiber Filled Polytetrafluoroethylene under Sea Water Lubrication. *Hydromechatronics Engineering*. 44, 18, 12-18, 2016.
- **Q Yang** and P Huang. Online Homework System of Fundamentals of Mechanical Design Based on ASP. *Journal of Guangxi University (Nat Sci Ed)*. 40, 2, 226-231, 2015.

Software Copyright

- P Huang and **Q Yang**. Online Homework System for Mechanical Curriculum. December 12, 2016. 2016SR366930.
- P Huang, W Zhan, and **Q Yang**. Test Paper Generation System for Mechanical Curriculum (Online Version). August 17, 2015. 2015SR158368.
- P Huang, **Q Yang**, and W Zhan. Test Paper Generation System for Mechanical Curriculum (Visual Basic Version). August 17, 2015. 2015SR158433.

Patent

- X Liu, **Q Yang**. A handheld wall cleaner for bathrooms. (Chinese Patent: Authorized - No. ZL 2015 2 1040425.1)

Awards

- Faculty Mentor Program Fellowship, *University of California, Merced* 2022
- Bobcat Fellowship, *University of California, Merced* 2019, 2020, 2021, 2022
- Travel Fellowship, *University of California, Merced* 2019, 2022
- Third Place Poster Award, *The Web Seminar Series on Tribology (WeSST)* 2020
- Summer Fellowship, *Merced nAnomaterials Center for Energy and Sensing (MACES)* 2019, 2020
- First-tier Scholarship, *South China University of Technology* 2016
- Third-tier Scholarship, *South China University of Technology* 2015
- Third-tier Scholarship, *Guangdong University of Technology* 2010

Academic Service

Conference Chair

- STLE Tribology Frontier Conference (Chicago, Illinois, USA) 2019
  - Chair of Tribochemistry session
  - Chair of Biotribology session

Peer Reviewer

- *Tribology Letters* (4), *Sustainability* (6), *International Journal of Environmental Research and Public Health* (3), *Applied System Innovation* (2), *Applied Sciences* (1)

Professional Membership

- Member, *Society of Tribologists and Lubrication Engineers (STLE)*

Conferences

- Gordon Research Conference (Newry, Maine, USA) 07/2022
  - Poster: "Effect of Aliphatic Chain Length on Polyamide Strain Response"
- The Web Seminar Series on Tribology (WeSST) (Online) 06/2020
  - Poster and presentation: "Nanoscale Friction of Hydrophilic and Hydrophobic Self-Assembled Monolayers in Water" (3rd place award)
- STLE Tribology Frontier Conference (Chicago, Illinois, USA) 10/2019
  - Presentation: "Molecular Dynamics Simulations of Amplitude Modulation Atomic Force Microscopy Probing Hydrophilic and Hydrophobic Self-assembled Monolayers in Water"
  - Chair of Tribochemistry session and Biotribology session
- The 73rd STLE Annual Meeting & Exhibition (Minneapolis, Minnesota, USA) 05/2018
  - Presentation: "Molecular Dynamics Simulations of Amplitude Modulation Atomic Force Microscopy Probing Hydrophilic and Hydrophobic Self-assembled Monolayers in Water"
  - Chair of Tribochemistry session and Biotribology session
- The 11th National Conference on Tribology (Chengdu, Sichuan, China) 10/2015
  - Presentation:"Numerical Calculation of Wear Behavior of Pin-on-disk"
- The 5th National Conference on Teaching of Mechanical Engineering (Nanning, Guangxi, China) 07/2015

Stress-strain Response of High-performance Crystalline Aromatic-aliphatic Polyamides

Quanpeng Yang, Ph.D.

University of California, Merced, 2022

Advisor: Professor Ashlie Martini

Aromatic polyamides, the most famous of which is poly(*p*-phenylene terephthalamide) (PPTA), are well-known for their excellent mechanical properties , thermal stability , and chemical resistance. These properties make PPTA ideal for many different uses, including aerospace and military applications where performance-to-weight ratio is critical. However, the processing of PPTA is challenging and expensive due to its solubility in only highly aggressive polar solvents and its high melting temperature (~500 °C). Therefore, it is desirable to design modified systems that improve processability without compromising other properties. It was reported that by introducing aliphatic compound into PPTA, the new polyamides, aromatic-aliphatic polyamides, had improved processability. However, the mechanical properties of these novel polyamides remained unknown. This dissertation seeks to study the mechanical properties of PPTA and four related amatic-aliphatic polyamides, PAP5-PAP8.

First, a ReaxFF force field developed by Liu et al. was identified to be the optimum for our systems after evaluating all of the nine candidate force fields based on crystal structures as well as intermolecular hydrogen-bonding and π-π interactions.

Then the Liu ReaxFF force field was used to simulate stress-strain behavior in the chain and transverse-to-chain directions for PPTA and PAP5. In the chain direction, PAP5 had higher ultimate stress and failure strain than PPTA; however, the stiffness of PAP5 was lower than PPTA at low-strain (0-2%) while the reverse was observed at high-strain (last 5% before failure). This contrast, and differences in the transverse direction properties, were explained by the methylene segments of PAP5 that confer conformational freedom, enabling accommodation of low strain without stretching covalent bonds.

Next, in order to study the aliphatic chain length effect on the stress-strain response, we extended the models pool by varying the numbers of carbon atoms in the aliphatic chain to obtain another three aromatic-aliphatic polyamides, i.e., PAP6, PAP7, and PAP8. Tensile strain was applied to each polymer crystal in the chain direction and the mechanical response was characterized.

The modulus at high strain was similar for all polymers, but the modulus calculated at low strain decreased with increasing aliphatic chain length. The decrease in the low-strain modulus with increasing chain length was attributed to the observation that polymers with longer aliphatic chains were wavier in the quiescent state such that they could accommodate low

strain without deforming covalent bonds. Extension of wavy chains occurred through an intra-chain process for all polymers, quantified by the bond dihedral angles. In addition, for polymers with an even number of non-aromatic carbons, the strain response involved slip between chains within the hydrogen bonded sheets. The ultimate stress of the polymers exhibited an odd-even effect which was explained by differences in hydrogen bonding and ring-ring coplanarity prior to failure; polymers with an even number of carbon atoms had less favorable H-bonding and poorer ring alignment.

The results revealed direct correlations between aliphatic chain length, intra- and inter-chain interactions, and the mechanical properties of polyamide crystals. Overall, the results of this dissertation contribute to establishing the framework of fundamental knowledge needed to design and optimize high-performance polyamides for various applications.

Keywords: molecular dynamics simulation, high-performance polymers, mechanical properties, polyamides, stress-strain, PPTA

Chapter 1

Introduction

1.1 High-performance Polymers

Today, life without polymers is unimaginable, because they have been the main synthetic materials in the 21^{st} century. Polymers are now produced in great variety for film packaging, solid molded forms for automobile body parts and frames of electronic devices, composites for pens and aircraft parts, foams for house and oven insulation, fibers for clothing and furniture, adhesives for attaching things, rubber for wheels and plumbing, paints and other coatings for beauty and elongation of life of other materials, and many other application.[39] Our modern world not have been existing without the presence of polymeric materials. Polymers have become a necessary part in every aspect of our society to improve the quality of human life.

Within different polymers, the family of high-performance polymers are particularly desirable, which are best classified by defining their properties. Generally, high-performance polymers possess superior properties allowing them to be used in severe conditions. Specifically, these polymers exhibit excellent mechanical strength per unit weight, high thermal stability (continuous use temperatures above 150 °C, combined with low flammability), chemical resistance (also at elevated temperatures) as well as good electrical properties (e.g., as insulators). Among this variety of polymers, there are structural materials used as reinforcing fibers or as the matrix in the production of high-performance composites, and functional materials for applications such as adhesives, substrates for optical discs, membranes or orientation layers for liquid-crystal displays.[94, 95, 135] These properties can be used to define the structural principles of this new class of polymers.[32, 33]

The quest for high-performance polymers began in the early 20^{th} century to meet the demands of the military, aerospace, machine-building and electronics industries, among many other industrial applications.[205] Within the last decades the needs of other industries, especially electronics, automobile, and machine-building, have resulted in innovation and development directed towards high-performance polymers.[74] Without these new materials many of today's technologies, e.g., electronics, would not have been possible. The market

for high-performance polymers will always be characterized by relatively small-volume and highly value-added products. Applications provide high rewards but require close cooperation with the customer to optimize the materials and processing technologies for specific purposes. For future technologies, high-performance polymers will still remain as a key item.

The very structural principles that provide the above discussed outstanding combinations of properties, however, also cause many problems with respect to processability. The melting or dissolving of stiff chains results in only a small change of entropy. Hence, these polymers have high melting points and are only sparingly soluble. Typical examples of high-performance polymers are polyamides.

1.1.1 Polyamides

Polyamides are an important class of high-performance polymers. They usually exhibit high impact or tensile strengths, electrical insulation, heat resistance, abrasion resistance, and also depending on the exact structure—biocompatibility, as well as tunability of these properties. These excellent properties make polyamides of interests for broad applications in different sectors including automotive, electrical, and textile industries.[1, 107, 155] The monomers of polyamides are connected through amide bonds, which can form hydrogen bonds (H-bonds) between adjacent polymer chains. Polyamides can be synthesized via polycondensation reactions of dicarboxylic acids and diamines, via polycondensation of amino acids or via ring-opening polymerization of cyclic amides, resulting in polyamides of AB- and AABB-types, respectively.[1, 107, 155, 195] The number of carbon atoms between the amide bonds describes the number after the prefix polyamides. Two of the most famous petroleum-based polyamides are Nylon-6,6 (polyamide 6,6, or PA66) and Nylon-6 (polyamide 6, PA6, polycaprolactam, or Perlon) (Fig. 1.1). Polyamide 6,6 is obtained via polycondensation of adipic acid and hexanediamine, which was developed by Carothers at DuPont in 1936,[22, 45, 161, 163] while polyamide 6 is obtained via ring-opening polymerizatio of ϵ-caprolactam, which was developed by Paul T. Schlack at IG Farben in 1937.[70] Both polyamides have been popular on the polymers market for decades. Besides, there are also a great deal of fossil-based polyamides and polyamide composites with diverse structures, including linear, cycloaliphatic, aromatic, hyperbranched, dendritic, and many other compounds.[107, 156]

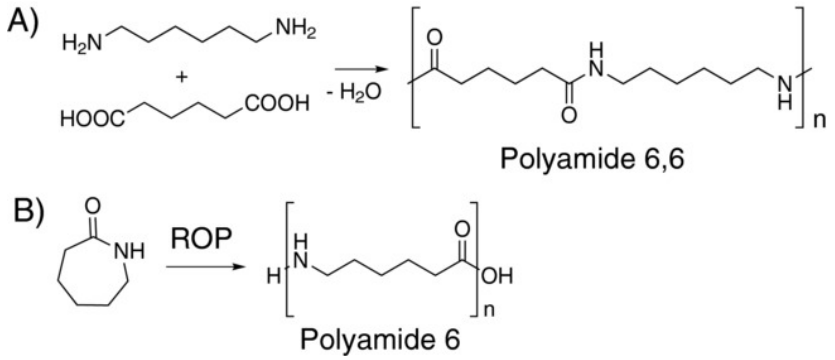

Figure 1.1: Synthesis of (a) polyamide 6,6 and (b) polyamide 6.[195] Copyright © 2016 by Wiley.

1.1.2 Aromatic Polyamides

Early studies showed that the thermal stability of a polymer could be increased by corporation of aromatic segments into it. [75] For this reason, many studies have been focusing on aromatic compositions. Therefore, high-performance polymers usually contain large numbers of aromatic units in their structures. Some high-performance aromatic polymers, such as aromatic polyamides, polyimides, polyesters, polysulfones, polytriphenylamine and heterocyclic polymers, have been used for commercial applications (Fig. 1.2).

Wholly aromatic polyamides (aramids) are considered to be high-performance materials due to their outstanding properties including thermal, chemical, and mechanical resistance. Their properties originate from their aromatic structure and amide linkages, which result in stiff rod-like macro molecular chains that interact with each other through highly aligned and strong H-bonds. [59] These bonds create effective crystalline micro domains, resulting in a high-level cohesive energy and intermolecular packing. [59] The most famous commercial aromatic polyamides is poly(*p*-phenylene terephthalamide) (PPTA), which is also trademarked as Kevlar® and Twaron®. PPTA is used in advanced technologies and has been transformed into high-strength and flame resistant fibers and coatings, with applications in the aerospace and armament industry, bullet-proof body armor, protective clothing, sport fabrics, electrical insulation, asbestos substitutes, and industrial filters, among others. [159] PPTA has been well known for decades and attracting more interests than other high-performance polymers because of its superior properties, such as excellent thermal stability, high mechanical strength (superior strength-to-weight ratio and flexibility) [159], thermal stability (thermal decomposition temperature of 500 °C) [201], and chemical resistance (to acid, alkali and organic solvent) [10, 24, 36, 37, 43, 73, 90, 93, 162, 201, 206]

These excellent properties originate from the atomic-scale structure of the PPTA fibers. X-ray diffraction (XRD) has shown [133] that PPTA fibers consist of a highly crystalline arrangement of extended PPTA chains aligned along the fiber axis with strong intermolecular H-bonds, which govern chain packing and melting behavior. [46, 67, 99, 112] Owing to their

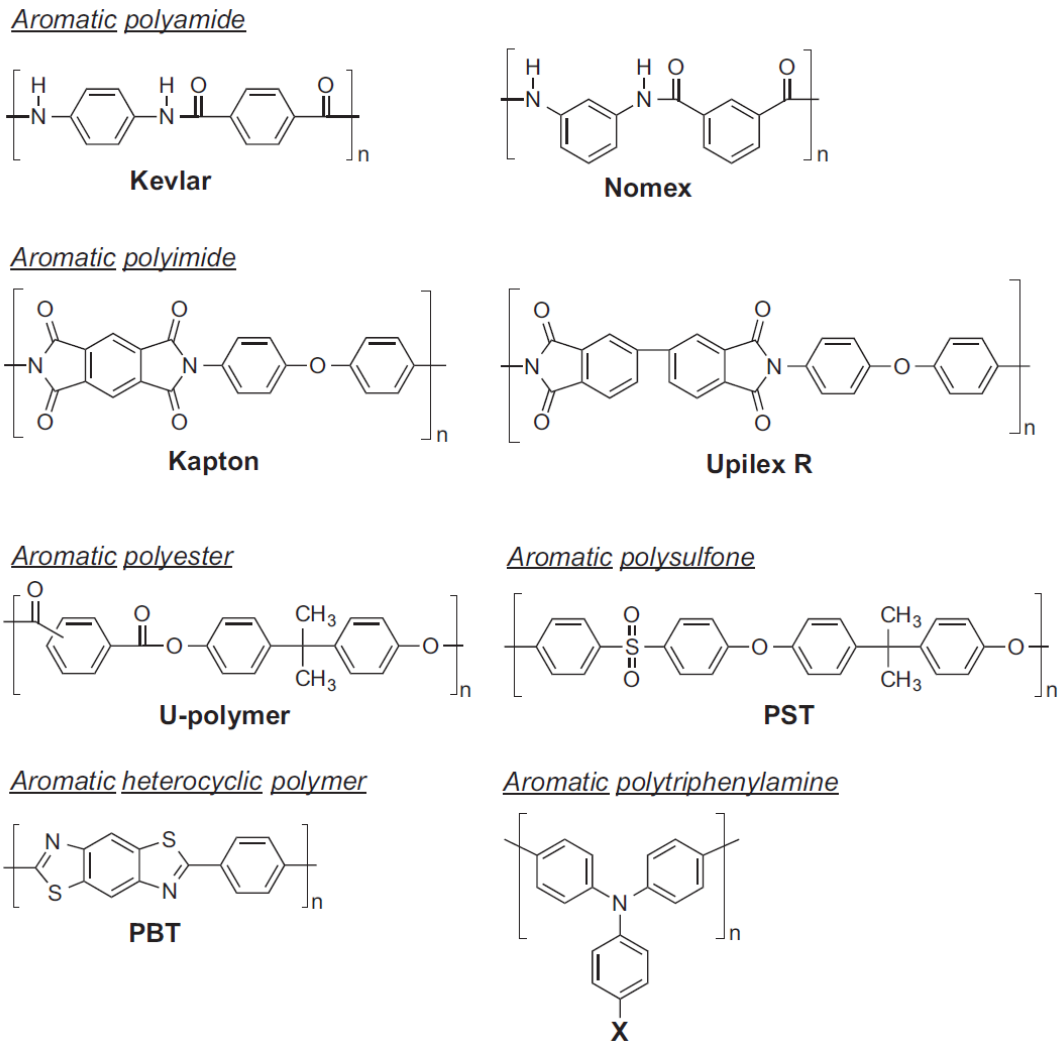

Figure 1.2: Chemical structures of the most common high-performance polymers.[206] Copyright © 2016 by Nature Portfolio.

chemical structure, aromatic polyamides, including PPTA, are highly crystalline and cannot be transformed by conventional methods like extrusion or injection because they do not melt. This is because their decomposition temperature is below their melting temperature. [59] In addition, they are sparingly soluble in common organic solvents and, accordingly, can only be transformed upon solution. Expanding the applications of aromatic polyamides involves increasing polymer solubility and processability without weakening the excellent chemical, thermal, and mechanical properties.

Research efforts are therefore underway to take advantage of their properties, enhance their processability and solubility, and incorporate new chemical functionalities in the polyamide backbone or lateral structure, so that their applicability is expanded and remains on the forefront of scientific research. To achieve this goal, there is interest in diminishing the cohesive energy through lowering the interchain interactions as a way of improving the solubility. In addition to using meta substitution in the main chain phenylene residues, this can be achieved by reducing the H-bond effectiveness through the introduction of bulky side groups to the main chain, by employing non-symmetric monomers, or by introducing flexible linkages to the polymer backbone. Fig. 1.3 is a schematic diagram showing the structural modification scenario for reducing the transition temperature and enhancing the solubility of rigid rod-like polymers, such as PPTA. Much work has been done in these areas, and most published papers claim polyamides with increasing solubility and processability. [8, 11, 104]

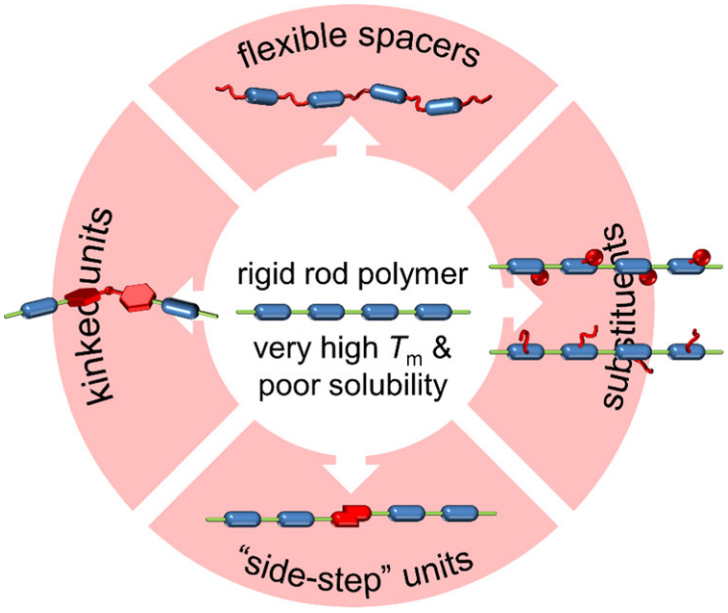

Figure 1.3: Schematic diagram showing the structural modification scenario for reducing the transition temperature and enhancing the solubility of rigid rod-like polymers, such as PPTA.[104] Copyright © 2020 by American Chemical Society .

1.1.3 Aromatic-aliphatic Polyamides

As mentioned above, although PPTA has many advantages, it has limitations as well. One main drawback is difficulty in processing because it is only soluble in highly aggressive polar solvents, such as concentrated sulfuric acid, making processing challenging, expensive, and environmentally unfriendly, and directly limit its broader application. [44, 54, 55, 59, 81, 217] Melt processing of PPTA is impossible because of its inaccessible melting point, so the primary processing route is currently solution processing. Regardless, it is desirable to design modified systems that improve processability without compromising other properties. Extensive research has been conducted to develop materials with properties comparable to PPTA but with potentially better processability. [120] The high melting temperature of PPTA is a result of its rigid and extended conformation, which is due to the rigidity of the aromatic polyamide backbone and strong intermolecular interactions—hydrogen bonding (H-bonding) and π-stacking. [17, 40, 46, 151, 177] To lower the melting temperature, a variety of methods have been attempted using chemical modification, including introducing bulky and packing-disruptive groups into the polymer chain or as side-groups, incorporating flexible groups into the polymer backbone, and using meta-oriented or asymmetrically substituted monomers. [5, 41, 69, 88, 101, 104, 212, 219] The enhanced solubility of PPTA in common organic solvents and lowered melting temperature of it is achieved using diamines, diacids, or both, that contain flexible ether linkages, bulky substructures, trifluoromethyl groups, substructures with rigid sp^3 carbons, amide–imide compounds, linear aliphatic and non-linear rigid alicyclic structures, or a mixture of thereof. [59] One such approach is to combine the rigidity of aromatic compounds and the flexibility of aliphatic compounds to create so-called aromatic-aliphatic polyamides. [7, 13, 46, 96, 120, 136, 152, 153, 202, 203]

1.2 Experimental Methods

1.2.1 Processing of Polyamides

There are two main routes to prepare polymer fibers: melt processing and solution processing.[97]

In melt processing, the polymer is heated over its melting temperature in an inert atmosphere, followed by extrusion the liquid polymer through a spinneret. By immediate cooling a phase transition occurs and the polymer solidifies. In this way, the polymer fibers can be obtained with a uniform structure. By stretching, very thin fibers can be obtained with a diameter less than 50 μm and a wall thickness of ~5 μm. The spinning rate is very high and can be over 1000 meters/minute.

The solution processing method involves a polymer and a latent solvent.[25] A latent solvent is a good solvent for a polymer at a high temperature, but a nonsolvent at a low temperature. The polymer solution can remain thermodynamically stable at high temperatures. Liquid-liquid demixing of the solution can be caused by the loss of solvent power as a result

of lowering the temperature. Further cooling will lead to crystallization or vitrification of the demixed solution.

In polyamides, such as PPTA, the presence of a stiff aromatic backbone leads to thermal degradation before melting. Therefore, melt processing is intractable, so the primary route is solution processing. Specifically, the polymer is spun from a solvent, which usually is concentrated H_2SO_4.[86, 97] Solution spinning and heat treatment results in the formation of yarns with extended chain crystals having tensile modulus and tensile strength greater than 100 and 2.3 GPa, respectively.[137, 201] However, from an environmental and economic viewpoint, the usage of H_2SO_4 in the spinning process of PPTA is disadvantageous. In contrast to wholly aromatic polyamides, the presence of flexible methylene segments between successive amide groups in aromatic-aliphatic polyamides results in melt-processable polymers, with melting temperatures in the range of 200–320 °C.[19, 46]

1.2.2 Experimental Studies on Aromatic-aliphatic Polyamide Crystals

To identify aromatic-aliphatic polyamides with properties comparable to PPTA (potentially with better processability), there has been increasing interest in understanding the effects of the structure and intermolecular forces within PPTA on its mechanical behavior [162]. Northolt *et al.* [133] showed through XRD that the microstructure of PPTA fibers consists of a highly crystalline arrangement of extended PPTA chains aligned along the axis of the fiber. Various experiments have been used to investigate these structure-property relationships for PPTA single fibers, including elastic loop [49, 65], transverse compression [29, 160], axial tension [29] and torsion [29] tests. These measurements have been complemented by material and surface characterization tools including scanning electron microscopy, transmission electron microscopy [49] and XRD [146]. These studies revealed that the orientation of crystallite, the rigidity of molecular chains, the density of defects, as well as the degree of molecular order are the main factors affecting the mechanical properties of PPTA. [49]

Clearly, it is of interest to develop polyamides by processing directly from the melt state using melt processing to obtain material properties comparable to those of aromatic polyamides. To achieve this goal, the rigidity of aromatic compounds can be combined with the flexibility of aliphatic compounds. Although the introduction of flexible aliphatic compounds will cause a reduction in the thermal and mechanical properties, this class of aromatic–aliphatic polyamides can be used to bridge the gap between aromatic polyamides and aliphatic polyamides in terms of processing and properties.[220] Employing this method, Morgan, Kwolek and Gaymans synthesized polyamides containing various aromatic and aliphatic compounds.[60, 120] It was observed that the melting temperature increases with increasing aromaticity but decreases with increasing chain length of the aliphatic diacid.[60, 120] Takayanagi and co-workers [169] modified the synthesis methods reported by Morgan and Kwolek. They reported the synthesis of segmented block-co-polyamides having varying aromatic segments combined with PA6 and PA66 units. Using the phosphorylation reaction route, Krigbaum and co-workers synthesized fully aromatic block copolyamides.[92] The phase behavior of these block copolymers in solution with dimethylacetamide (DMAc) was investigated in the presence of LiCl

(3 wt%).[92] Picken and co-workers reported the synthesis of lyotropic rigid-coil poly(amide-block-aramid)s, where segmented block copolymers were prepared using PPTA and PA66 in NMP/$CaCl_2$.[82, 149, 186] In industrial applications, the polyamide poly(nonamethylene terephthalamide) (PA 9-T) has been commercialized as GENESTAR by Kuraray as an engineering thermoplastic, which shows the potential of aromatic-aliphatic polymers.[179] More recently, it was found that the mechanical properties (tensile strength, ultimate strain, and Young's modulus) of aromatic-aliphatic polyamides were lower than PPTA. [52, 220]

1.2.3 Limitations of Experiments on Polyamide Crystals

However, there are challenges associated with studying the mechanical properties of polyamide crystals experimentally. [162] First, it is expected that even minor changes in the molecular structure of the aromatic-aliphatic polyamides might significantly affect mechanical behavior. For example, longer spacer lengths for a given aromatic amide system leads to a reduction in H-bonds density which will lower the melting temperature. [120] However, experimentally studying this relationship for polyamide crystals is difficult and time-consuming, and requires sensitive equipment. [38, 142, 162] In addition, experimental studies of the mechanical properties of PPTA in the directions transverse to the fiber axis focused only on compressive behavior [49, 65, 160] due to the difficulties associated with applying tensile strain in the transverse direction. [172] Further, obtaining large single crystal materials is challenging (slow evaporation of solvent is used to get large single crystals for modulus measurements [9, 122, 197]), and the morphology of the polymers is complicated due to the presence of amorphous contributions (e.g., non-crystalline regions and defects). These facts necessitate both delicate handling and sensitive equipment. [38, 142] Finally, it is difficult with experimental techniques to distinguish the relative contributions of intramolecular (e.g., covalent bonds) interactions and intermolecular interactions (e.g., H-bonding and π-stacking) to bulk mechanical properties. [173] Design of new materials requires insight into the relative contributions of intramolecular interactions and intermolecular interactions, i.e., H-bonding between amide groups and interactions between the π-manifolds of the aromatic rings (π-stacking or π-π stacking). [173].

1.3 Computational Methods

With the rapid development of high technologies in all areas, advanced materials science has arrived at a point of time where there is needs for a precise control of the properties of products, as well as for design of new materials to meet specific demands.[68] In parallel with this need, researchers have realized that these needs can only be met with efficiency by achieving a via the understanding of how atomic, molecular, and mesoscopic features affect macroscopic behavior. Quantum mechanical calculations provide a method to understand and to predict the interactions between atoms and molecules and to model chemical reactions on the atomic scale. Methods based on statistical mechanics and on continuum mechanics can use this information as input to investigate the mesoscopic and macroscopic behavior. In the

last decades, important theoretical and algorithmic theories of condensed matter and quantum chemistry were developed significantly. Together with the revolution that has occurred in computer technology, these advances enable us to solve problems of practical interests and importance. Computational methods have significantly changed the form of scientific research. As a result, scientists now have the ability to predict material properties without doing actual experiments. Computational methods such as density functional theory (DFT) calculations, molecular dynamics (MD) simulations, Monte Carlo simulations, and coarse grained simulations are used to bridge the gap between fundamental materials science and materials engineering, since they provide insight into material properties and behavior at the atomistic scale under controlled conditions. [162]

1.3.1 Computational Materials Modeling from First Principles

"Materials modeling" is the development and use of mathematical models for describing and predicting certain properties of materials at a quantitative level. When we specify that the model is "from first principles" (ab initio), we refer to the choice of a bottom-up modeling strategy, to understand and predict certain properties without relying on empirical parameters. This is possible if we can identify a fundamental theory of materials that is general, flexible and reliable. Luckily, such a theory does exist and is called quantum mechanics.

The use of quantum mechanics in the study of material properties goes through the solution of the complicated Schrödinger equation. The complexity of the mathematical problem is so formidable that even a single particle Schrödinger equation is a complex second order differential equation in three dimensions. So there is no general mathematical way to solve such equations in a closed form.

Therefore, modern computational modeling of materials from first principles relies on a variety of theoretical and computational techniques. The common denominator of such techniques is that they are based upon DFT. DFT is a very effective technique for studying molecules, nanostructures, solids, surfaces and interfaces, by directly solving approximate versions of the Schrödinger equation. DFT was born in an extraordinary 1964 paper published by Hohenberg and Kohn in 1964 in the journal Physical Review, entitled "Inhomogeneous Electron Gas" [77]. Using this theory, the properties of a many-electron system can be determined by using functionals, i.e., functions of another function. In the case of DFT, these are functionals of the spatially dependent electron density. In other words, understanding the properties of a gas of electrons was the key to the development of reliable ab initio models of materials.

The material properties that can be calculated using DFT include: equilibrium structures, vibrational properties and vibrational spectra, binding energies of molecules and cohesive energies of solids, ionization potential and electron affinity of molecules, band structures of metals and semiconductors. [61]

The concept of predicting material properties is meaningful because computational methods based on the first principles of quantum mechanics are entirely general, and can be applied to any combination of atoms. This concept can be especially useful in the optimization

and design of new materials. The use of DFT for "materials discovery" has been gaining popularity during the past decade, [64, 87] and can be expected to become more widespread as the calculations become more accurate and less time-consuming.

1.3.2 Classical Molecular Dynamics Simulations

The accuracy and speed of DFT method allow the geometries, energies, and vibrational energies to be predicted quite accurately for small molecules. However, DFT is not yet practical for studying the dynamic properties of larger molecules because of its expensive computation which limiting them to few nanometers system size and simulation times of tens to hundreds of picoseconds. Consequently, it is useful to have accurate models to quickly evaluate the forces and other dynamical properties such as stress-stress response of polymers.

MD simulations using forces calculated from empirical potentials is commonly called classical MD simulations. [47] Unlike the bottom-up approach in DFT, classical MD simulations use a top-down approach, i.e., extracting empirical laws by fitting experimental measurements, instead of calculating "from first principles". Classical MD simulations play an important role between more accurate but computationally intensive DFT studies that are restricted to a few hundred atoms and coarse grained simulations that have to be extensively parameterized. [47, 48]

The ability of MD simulations to accurately describe material properties depends on the empirical model force field, which is a collection of equations and associated constants designed to reproduce molecular geometry and selected properties of tested structures. In other words, a model is described by the force field as a series of charged points (atoms) linked by springs (bonds). With a force field, it is possible to describe the time evolution of bond lengths, bond angles and torsions, as well as the non-bonding van der Waals and elecrostatic interactions between atoms. There are two general types of force fields, one is reactive and the other is non-reactive. With non-reactive force fields, bonds can be stretched and twisted but not be broken, while reactive force fields can capture the formation and scission of chemical bonds. Previous simulations of PPTA have used both reactive and non-reactive force fields, as discussed below.

1.3.2.1 Non-reactive Force Fields

Popular non-reactive force fields include AMBER [23], CHARMM [16], COMPASS (condensed-phase optimized molecular potentials for atomistic simulation studies) [167], PCFF (Polymer Consistent Force Field) [168], OPLS (Optimized Potentials for Liquid Simulations) [50], CVFF (Consistent Valence Force Field) [42], and Dreiding [109].

The non-reactive Dreiding [109] force field was used to reproduce the molecular packing structure of PPTA polymer crystal [129]. Another non-reactive force field, COMPASS [167], was also used to study the properties of PPTA crystals. [66, 67] One of those studies focused on the effects of microstructural and topological defects, such as chain ends, inorganic-solvent impurities, chain misalignment and sheet stacking faults on the strength, ductility and stiffness

of PPTA crystals. [66] In another COMPASS simulation study [67], the effect of torsion on the tensile properties of PPTA crystals was investigated.

1.3.2.2 Reactive Force Fields

Non-reactive force fields are more computationally efficient than reactive but the bonding state of atoms is not captured such that covalent bonds cannot be broken or formed during the simulation.

ReaxFF [182] is an empirical force field that employs a bond-length/bond-order/bond-energy relationship to obtain a smooth transition between bonded and nonbonded systems, thus allowing reactions to happen during MD simulations. During an MD simulation, the bond orders are updated every iteration, and the calculation of the system potential energy takes the bond-order into account. ReaxFF also considers nonbonded interactions for each pair of atoms, including van der Waals and Coulomb terms. ReaxFF also includes a geometry dependent polarizable charge calculation. These charges are updated in every iteration.

Since first developed in 2001 [182], hundreds of papers have been published on the development of ReaxFF parameteriazations for materials in a wide range of elements (see available elements in Fig. 1.4). As shown in Fig. 1.5, there are currently two major ReaxFF branches of parameter sets that are not transferable with each other: the combustion branch and the aqueous branch. The big database of ReaxFF parameter sets enables researchers to choose the best available parameter set for their systems to perform MD simulations.

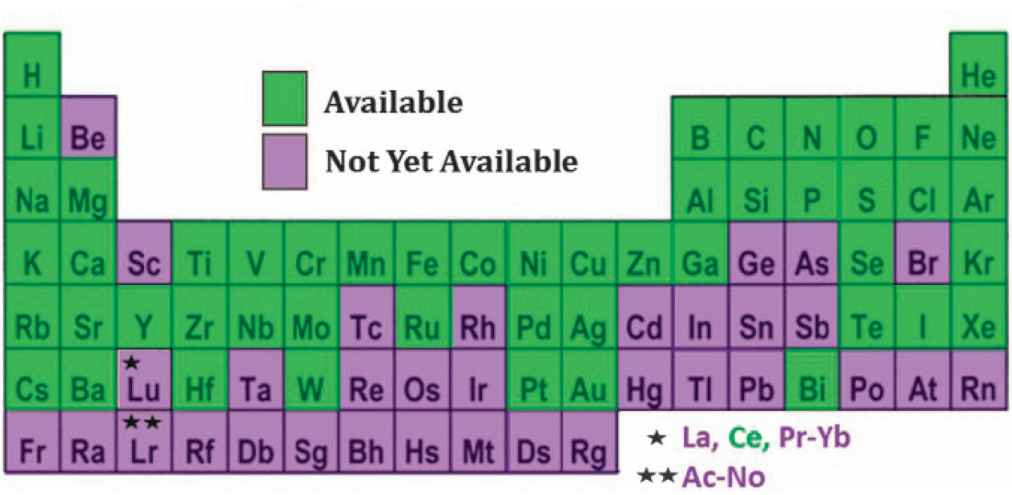

Figure 1.4: Available elements in the ReaxFF force field. The elements in green are available and those in purple are not yet available[206]. Copyright © 2016 by Nature Portfolio.

ReaxFF has been used to model high-performance polymers such as PPTA. The tensile response of PPTA crystals with defects was studied [208] using a ReaxFF parameter set developed

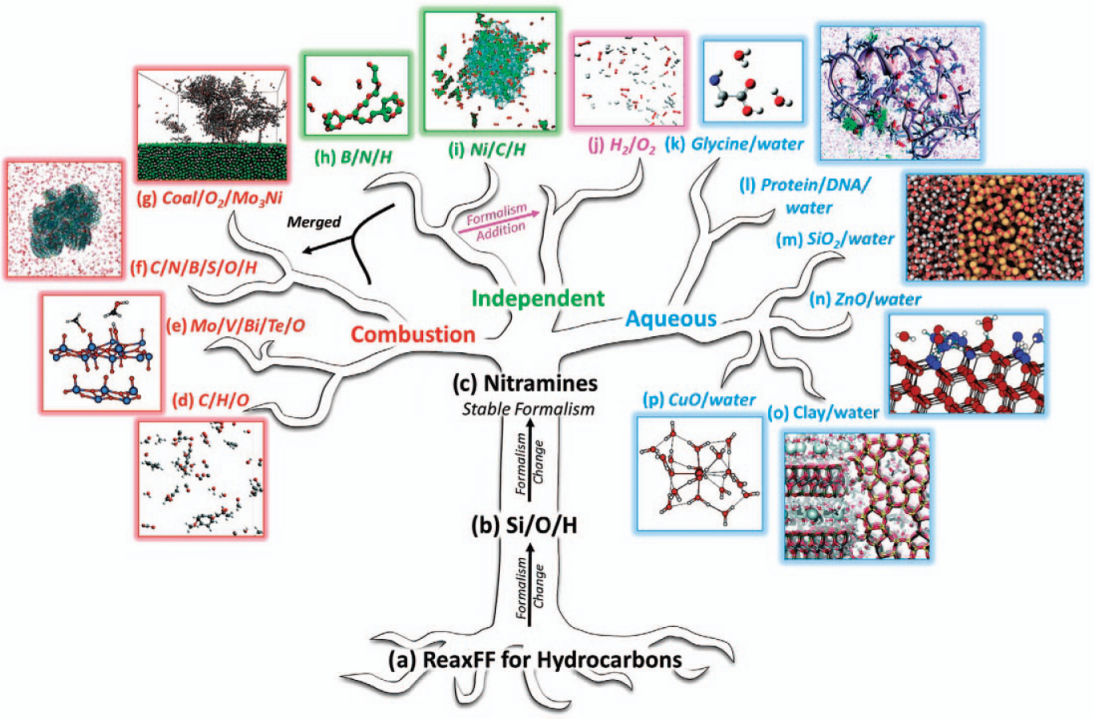

Figure 1.5: ReaxFF development tree, where parameter sets on a common 'branch' are fully transferable with one another. Parameter sets are available in (a) van Duin *et al.* [182], (b) van Duin *et al.* [183], (c) Strachan *et al.* [164, 165], (d) Chenoweth *et al.* [30], (e) Goddard *et al.* [62] and Chenoweth *et al.* [31], (f) Castro-Marcano *et al.* [26] and Kamat *et al.* [85], (g) Vasenkov *et al.* [214], (h) Weismiller *et al.* [193], (i) Mueller *et al.* [121], (j) Agrawalla *et al.* [2], (k) Rahaman *et al.* [145], (l) Monti *et al.* [118], (m) Fogarty *et al.* [57], (n) Raymand *et al.* [148], (o) Pitman *et al.* [140] and Manzano *et al.* [106], and (p) van Duin *et al.* [181] [157].

by Budzien *et al.* [20] A ReaxFF parameter set developed by Liu *et al.* [102] was used to study the mechanical properties of PPTA in the presence of defects [112], the influence of strain rate and temperature on the mechanical strength [111], and the effects of axial and transverse compression on the residual tensile stress of PPTA. [35]

These simulation-based studies have revealed important connections between intermolecular and intramolecular interactions and the material properties of PPTA. Simulations have shown that H-bonds form in the radial plane (parallel to the flat aromatic rings) and repeat along the chain axis forming "sheet-like" structures. [67, 130] The interaction strength between adjacent PPTA chains is further increased by "inter-sheet" π-stacking. [67] This stacking mechanism contributes to the long-range, highly ordered structures observed in PPTA fibers. [103] Such simulations support the hypothesis that the excellent mechanical properties of PPTA fibers originate from the strong intermolecular interactions (H-bonding and π-stacking). In a study using ReaxFF, the effect of H-bonding on PPTA properties was quantified by numerically "turning off" the H-bond interactions in the force field, and a small decrease (1%) in tensile modulus was measured in the chain direction, but in the transverse directions, modulus and strength were reduced significantly (by 40% and 69%, respectively). [34]

1.3.2.3 Molecular Dynamics Studies on Aromatic-aliphatic Polyamides

MD simulations have been successfully applied to study aromatic-aliphatic polyamide crystals, including the role of aliphatic and aromatic groups on intermolecular interactions, free volume, and glass transition temperature [27, 104], the origin of melting, and the influence of methylene segments on crystal packing and chain conformation. [46] Specifically, Chantawansri *et al.* [27] investigated the molecular influence on glass transition temperature (T_g) of cycloaliphatic, aromatic-aliphatic polyamides, and aliphatic polyamides by atomistic modeling. They found that both the chain rigidity and the extent of free volume can influence on the glass transition temperature of polymers. Both the cycloaliphatic and aromatic-aliphatic polyamides are more rigid than the aliphatic polyamides due to the presence of aromatic ring structures along the polymer backbone. Besides, they found that H-bonding can affect the chain rigidity and free volume by affecting the molecular packing. In another study, by Long *et al.*,[104] three kinds of aromatic-aliphatic polyamides with different pendent groups, termed as P-PAH (dimethyl-), P-PEPH (methylphenyl-), and P-DPMPH (diphenyl-), were designed and prepared via aromatic nucleophilic substitution polycondensation. As illustrated by MD simulation, chain conformations of P-PAH and P-DPMPH presented characteristic random-coil structures of amorphous polymers, while P-PEPH with asymmetric methylphenyl pendants showed a partial helical conformation, showing a positive effect to form intra-/intermolecular H-bonds. It was found that the glass-transition temperature and the thermal stabilities of the synthetic SaPAs were improved with increasing content of the phenyl pendents. Meanwhile, P-PEPH and P-DPMPH exhibited much higher mechanical properties than P-PAH. On the one hand, P-PEPH and P-DPMPH possessed a higher rigidity and larger bulk size of the pendent groups; on the other hand, the π-stacking interaction effectively dominantly enhanced the molecular interaction. In addition, the influence of flexible methylene

segments on molecular conformation have been pursued by a combination of experimental and MD simulation methods by Deshmukh *et al.* [46] The measurements showed that all aromatic–aliphatic polyamides synthesized in this study are of a semicrystalline nature and have a similar degree of crystallinitiy. The shift in the carbonyl peak with increasing number of methylene units suggests a weakening in the H-bonding with respect to PPTA. Understanding the relationship between chemical structure and the emergent physical properties will enable chemists to synthesize polymers with desired thermo-mechanical properties.

1.3.2.4 Limitations of Previous Simulation Studies

Although many different force fields have been used for MD simulations of PPTA to study various aspects of this material. For example, one previous study compared two force fields (PCFF [168] and ReaxFF Liu [102]) for their ability to model PPTA structure and mechanical response to strain. [112] It was found that the PCFF and ReaxFF Liu force fields give similar results, except that PCFF can only be used for situations where primary bonds are not expected to rupture. Regardless, there has been no direct comparison of a comprehensive set of force fields, including multiple reactive and non-reactive models, in the ability of faithfully reproducing the mechanical response of PPTA and related aromatic-aliphatic polyamides. Only when an accurate force field and suitable methods have been identified, can MD simulations be used with confidence to investigate the effect of structural features that underlie the material properties of aromatic-aliphatic polyamides. Further, since intermolecular interactions play an important role in the mechanical response of PPTA, force field comparisons should include evaluation of the ability to model H-bonding and π-stacking patterns. Finally, the accuracy of MD simulations is highly dependent on the suitability of the force field for the specific material system being studied, so generalizability must be assessed by evaluating homologous material systems.

Deshmukh *et al.* [46] showed that the length of the methylene segments in aromatic-aliphatic polyamides affects the polymer conformation and structure. In their work, aromatic-aliphatic polyamides, prepared from *p*-phenylene diamine and aliphatic diacids, were referred to as PAPX, where X was the number of carbon atoms in the diacid monomer. They also showed that methylene units in PAP5 weakened the H-bonds and altered the topology of the H-bonding sheets relative to PPTA. However, the effect of these conformational differences between PPTA and PAP5 were only investigated on the processability but not yet on mechanical properties. Further, MD simulations have not been used to understand the effect of the length of flexible aliphatic compounds on the mechanical properties of semi-aromatic polyamide crystals.

1.4 Dissertation Outline

This dissertation consists of five chapters:

In Chapter 1 (this chapter), the background of high-performance polymers (such as aromatic polyamides and semi-aromatic polyamides), and computational methods (DFT, MD

simulations) for studying these topics were introduced.

Chapter 2 described the selection of suitable force field for the polyamides studied in this study in terms of the lattice parameters, H-bonding, π-π stacking, stress-strain response, and XRD patterns. In addition, a suitable size of the system models were determined based on the stress-strain response as well.

The stress-strain response of PPTA and PAP5 in the chain and transverse directions using the optimal system size and force field selected in the previous section was shown in Chapter 3.

Chapter 4 extended the number of polyamides to study the effect of aliphatic chain length on the stress-strain response of polyamides. In this section, we compared the stress-strain response of PPTA and four related aromatic-aliphatic polyamides, i.e., PAP5, PAP6, PAP7, and PAP8, in the chain direction.

In Chapter 5, this study was summarized. In addition, the next steps for this research were proposed, including the effect of functional groups on the stress-strain response as well as prediction of mechanical properties using machine learning techniques.

Chapter 2

Force Field Selection for Molecular Dynamics Simulations of Polyamides

2.1 Introduction

MD simulations are a natural complement to experiments since they provide insight into material properties and behavior at the atomistic scale under controlled conditions. [162] MD simulations can help not only to interpret complicated experimental results, but also guide the development of new experimental methods. The ability of these simulations to accurately describe material properties depends on the empirical model force field for atomic interactions. There are two general types of force fields, reactive and non-reactive. With non-reactive force fields, bonds can be stretched and twisted but not be broken, while reactive force fields can capture the formation and breaking of chemical bonds. Previous simulations of PPTA have used both reactive and non-reactive force fields, as discussed below.

The non-reactive Dreiding [109] force field was used to reproduce the molecular packing structure of PPTA polymer crystal [129]. Another non-reactive force field, COMPASS (Condensed-phase Optimized Molecular Potentials for Atomistic Simulation Studies) [167], was also used to study the properties of PPTA crystals. [66, 67] One of those studies focused on the effects of microstructural and topological defects, such as chain ends, inorganic-solvent impurities, chain misalignment and sheet stacking faults on the strength, ductility and stiffness of PPTA crystals. [66] In another COMPASS simulation study [67], the effect of torsion on the tensile properties of PPTA crystals was investigated.

PPTA has also been modeled using ReaxFF [182], a reactive force field. The tensile response of PPTA crystals with defects was studied [208] using a ReaxFF parameter set developed by Budzien et al. [20] A ReaxFF parameter set developed by Liu et al.[102] was used to study the mechanical properties of PPTA in the presence of defects [112], the influence of strain-rate and temperature on the mechanical strength [111], and the effects of axial and transverse compression on the residual tensile stress of PPTA. [35]

These simulation-based studies have revealed important connections between intermolec-

ular and intramolecular interactions and the material properties of PPTA. Simulations have shown that H-bonds form in the radial plane (parallel to the flat aromatic rings) and repeat along the chain axis forming "sheet-like" structures. [67, 130] The interaction strength between adjacent PPTA chains is further increased by "inter-sheet" π-stacking. [67] This stacking mechanism contributes to the long-range, highly ordered structures observed in PPTA fibers. [103] Such simulations support the hypothesis that the excellent mechanical properties of PPTA fibers originate from the strong intermolecular interactions (H-bonding and π-stacking). In a study using ReaxFF, the effect of H-bonding on PPTA properties was quantified by numerically "turning off" the H-bond interactions in the force field, and a small decrease (1%) in tensile modulus was measured in the chain direction, but in the transverse directions, modulus and strength were reduced significantly (by 40% and 69%, respectively). [34]

The MD simulations of PPTA summarized above have used many different force fields to study various aspects of the material. One previous study compared two force fields (PCFF [168] and ReaxFF Liu [102]) for their ability to model PPTA structure and mechanical response to strain. [112] It was found that the PCFF and ReaxFF Liu force fields give similar results, except that PCFF can only be used for situations where primary bonds are not expected to rupture. However, there has been no direct comparison of a comprehensive set of force fields, including multiple reactive and non-reactive models. Further, since intermolecular interactions play an important role in the mechanical response of PPTA, force field comparisons should include evaluation of the ability to model H-bonding and π-stacking patterns. Finally, the accuracy of MD simulations is highly dependent on the suitability of the force field for the specific material system being studied, so generalizability must be assessed by evaluating homologous material systems.

Therefore, to ensure the MD simulations being able to faithfully reflect the reality a suitable force field should be carefully selected. In this chapter, we used PPTA and PAP5 as model systems to compare the performance of candidate force fields aiming at identifying the optimum force field for the polyadmides of our interests. First, several force fields (both non-reactive and reactive) were compared to identify the most accurate model of the static structures of PPTA and PAP5. This analysis included both unit cell lattice parameters, H-bonding and π-stacking distances, as well as XRD patterns. Different model sizes were also compared to identify the smallest possible system capable of accurately modeling these material properties. Then, using the reactive and non-reactive force fields that best captured the static structures of the materials, simulations were run to characterize the response of the polymer crystals to tension in the chain and transverse directions.

2.2 Methods

2.2.1 Structural Models

The aromatic polyamide models were initially constructed using Materials Studio [12], with unit cell lattice parameters measured based on experimental XRD patterns [3, 46, 187]. The

unit cell lattice parameters of PPTA and PAP5 are listed in Table 2.1. The atomic positions were then adjusted manually in Materials Studio to match the model-predicted XRD patterns with the experimental XRD patterns as shown in Fig. 2.1 and 2.2 for PPTA and PAP5, respectively. The XRD patterns from simulation models were calculated using "Scattering" in "Forcite Analysis" with a cutoff distance of 50 Å and an X-ray wavelength of 1.54 Å. Note that the XRDs from MD models and experiments are not identical since the MD models are perfect crystalls without any defects which are commonly existing in experimental specimens. However, the XRDs are reasonably similar to each other in terms of the main peaks such as 20.5 ° vs. 20.5 ° and 22.6 ° vs. 23.0 ° for PPTA in Fig. 2.1. Similarly, it is 7.15 ° vs. 7.16 ° and 21.1 ° vs. 21.2 ° for PAP5 in Fig. 2.2.

The initial density of PPTA was 1.50 g/cc, consistent with the experimentally measured densities in the range of 1.44-1.48 g/cc. [159, 201] The chemical formulas and atomic-scale models of PPTA and PAP5 unit cells are shown in Fig. 2.3a and Fig. 2.3b, respectively. The chain direction was aligned with the x-axis, and the H-bonding and π-stacking directions were aligned with the y- and z-axes, respectively.

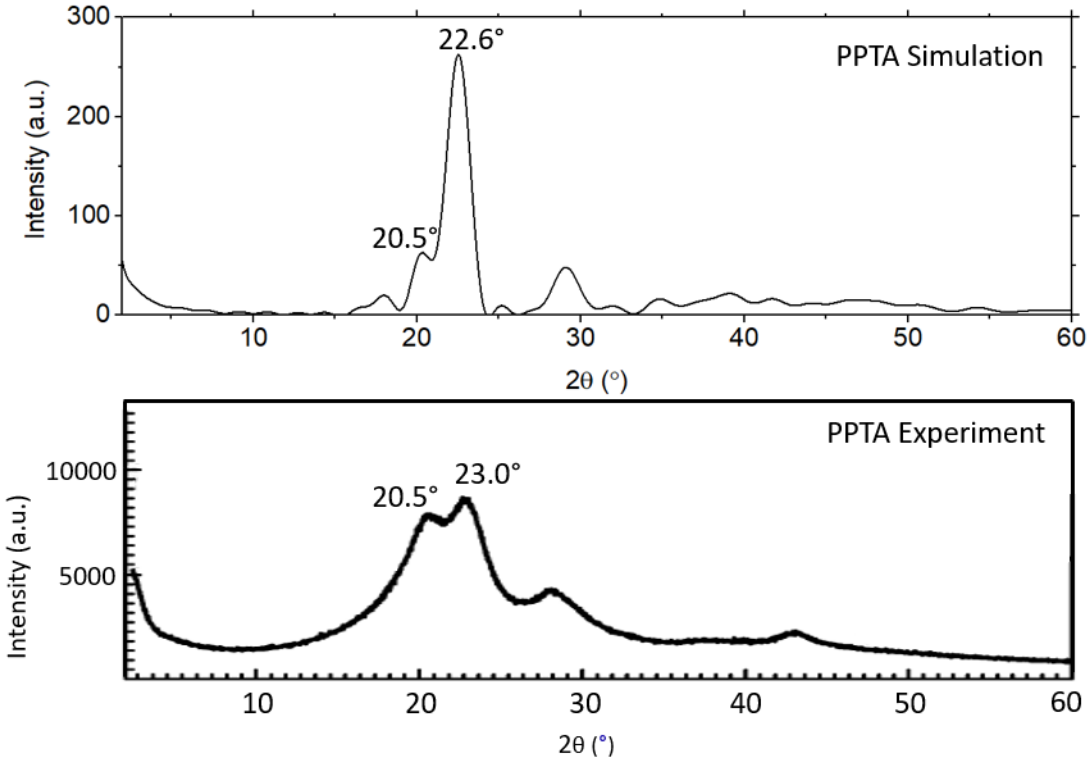

Figure 2.1: XRD patterns of PPTA from initially-built MD model and experiments. The experimental XRD pattern and the values of the peak angles were taken from Ref. [3, 46, 187]

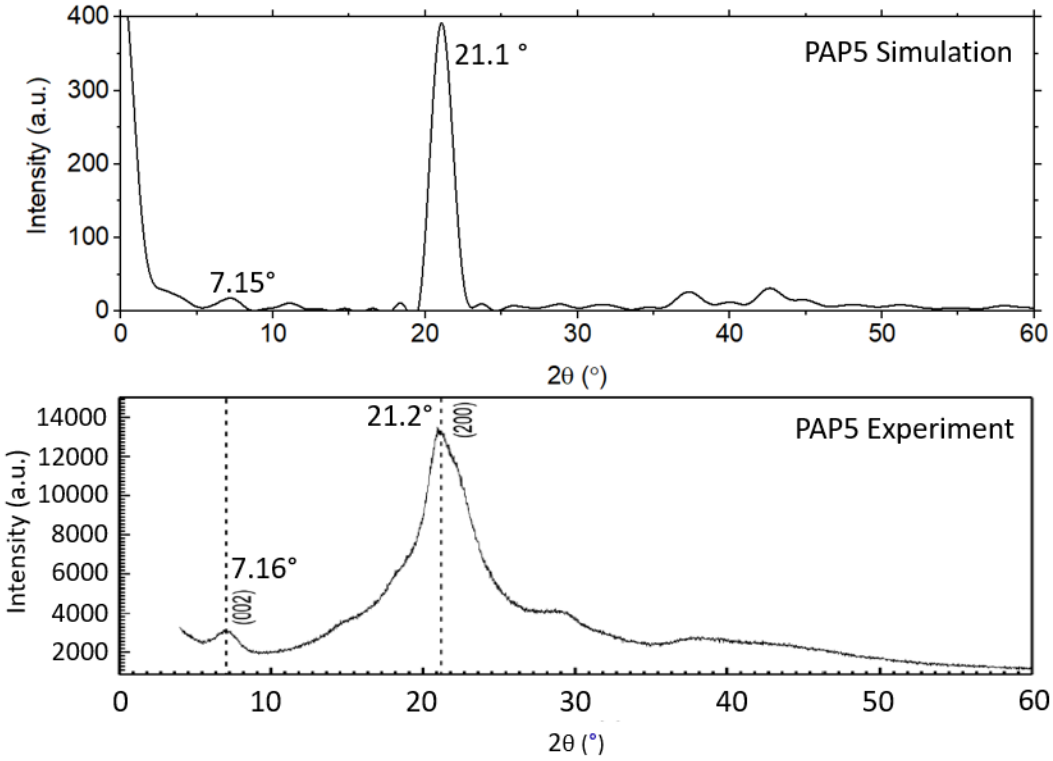

Figure 2.2: XRD patterns of PAP5 from initially-built MD model and experiments. The experimental XRD pattern and the values of the peak angles were taken from Ref. [3, 46, 187]

Polymer	a (Å)	b (Å)	c (Å)	α (°)	β (°)	γ (°)
PPTA	7.87	5.18	12.9	90	90	90
PAP5	8.50	4.70	24.8	90	85	90

Table 2.1: Unit cell lattice parameters for PPTA and PAP5 [46, 134]

The foundational element of the crystalline structure is the unit cell. PPTA and PAP5 have orthorhombic and monoclinic (pseudo-orthorhombic) crystal structures, respectively, but both [46, 133, 134, 162, 173] with two molecular chains per unit cell, one at the center and the other at the corner of the cell viewed in the yz plane, see Fig. 2.3. [46, 134, 162, 173] The main differences between their unit cell structures are: (1) PAP5 has four monomers in its c-axis repeat unit, whereas PPTA has only two; (2) the terephthalic acid monomer of PPTA is replaced by a diacid monomer with three methylene groups to form PAP5, so there are five carbon atoms and two -NH- groups between two adjacent aromatic rings in each PAP5 monomer, while there is only one carbon and one -NH- group between the two adjacent aromatic rings in each PPTA monomer; (3) the unit cell length c of PAP5 is almost twice that of PPTA (56 atoms in PPTA and 108 atoms in PAP5); and (4) there is a slight tilt of β in the unit cell of PAP5 while all lattice angles are 90° for PPTA.

After the unit cell was built, it was replicated by $N_x \times N_y \times N_z$ ($1\times1\times1$, $4\times4\times4$, $6\times4\times4$, $8\times4\times4$, $6\times6\times6$, and $8\times8\times8$) in the x-, y- and z-directions to create simulation cells with a range of sizes. Note that the models with periodic boundary conditions in all three directions represent ideal crystalline polymers with infinite chain length and no defects or chain ends. This is an approximation of a physical crystalline polymer that will have finite length chains with defects and chain ends. However, the simulation methods developed here for an ideal crystal can be extended in future work to more realistic model structures.

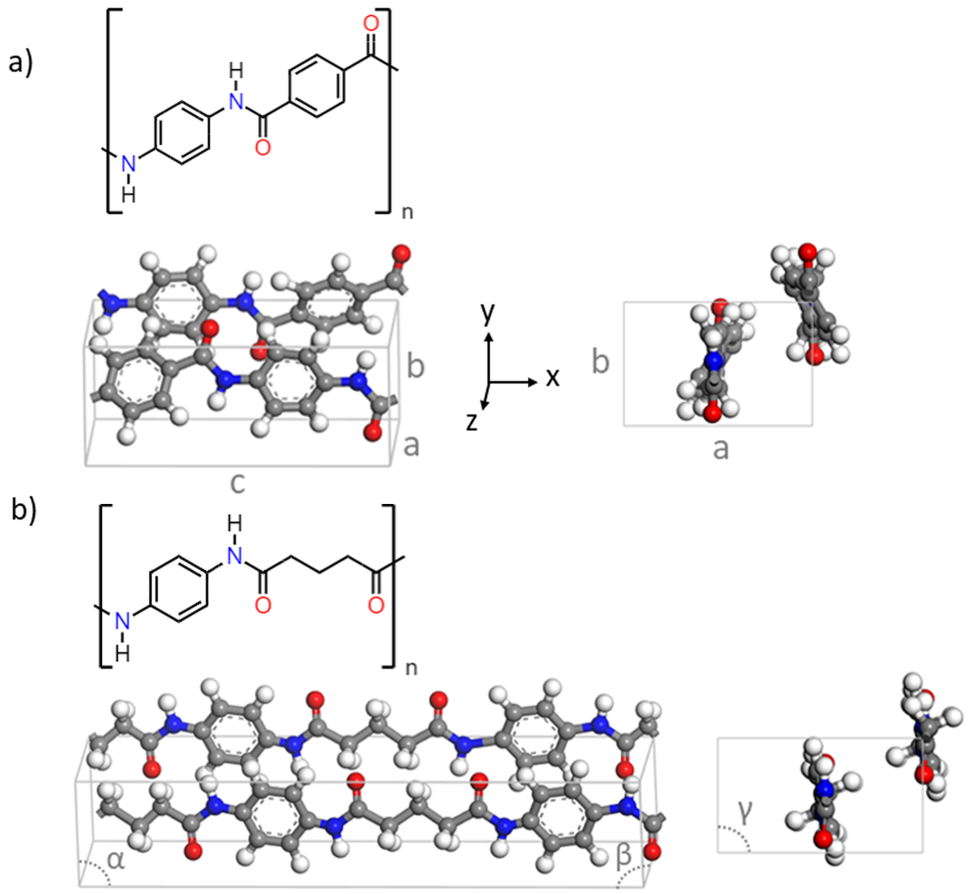

Figure 2.3: Unit cells of (a) PPTA and (b) PAP5 where lattice dimensions (a, b, and c) are identified on the PPTA snapshot and lattice angles (α, β, and γ) are identified on the PAP5 snapshot. The orthogonal directions (x, y, and z) are also defined with respect to the perspective views of the unit cells. Atom colors correspond to: oxygen, red; nitrogen, blue; carbon, gray; hydrogen, white. The cross-section views on the far right show the crystals from the yz plane.

2.2.2 Force Fields

Two non-reactive force fields were tested: OPLS [50] and CVFF [42]. Seven different ReaxFF parameterizations were tested as well, chosen because they include all of the elements in our model systems (oxygen, nitrogen, carbon, and hydrogen). Each ReaxFF parameter set is referred to subsequently by the last name of the first author of the paper in which it was first reported, including Zhang [213], Budzien [20], Kamat [85], Mattsson [108], Liu [102], Wood [196], and Vashisth [185]. Each of these was parameterized for different molecular systems, as summarized in Table 2.2.

Force Field	Material System for Parameterization
Zhang (2009) [213]	Thermal decomposition of hydrazines
Budzien (2009) [20]	Thermomechanical properties of pentaerythritol tetranitrate
Kamat (2010) [85]	Laser-induced incandescence of soot
Mattsson (2010) [108]	Polyethylene and poly(4-methyl-1-pentene)
Liu (2011) [102]	Polyethylene and energetic materials
Wood (2014) [196]	Decomposition of the high-energy-density material α-HMX
Vashisth (2018) [185]	Cross-linking of polymers

Table 2.2: ReaxFF parameter sets and the molecular systems for which they were first parameterized are identified by the last name of the first author of the corresponding paper in order of publication date.

2.2.3 Simulation Protocol

All of the MD simulations in this study were carried out using an open source MD simulation package LAMMPS (Large-scale Atomic/Molecular Massively Parallel Simulator). [141] Software OVITO (Open Visualization Tool) [166] was used for model visualization. The MD time step was 0.25 fs for all simulations. Temperature and pressure were controlled using a Nosé-Hoover thermostat [79] and barostat [80] with damping parameters of 25 fs and 250 fs, respectively. The cut-off distance for Lennard-Jones and electrostatic interactions was 1.5 nm for non-reactive force fields. For the ReaxFF force fields the default cut-offs were used (in LAMMPS, nbrhood_cutoff was 0.5 nm and hbond_cutoff was 0.75 nm). First, the replicated simulation cell was energy minimized. Then, simulations were run in the NPT (constant number of atoms, pressure and temperature) ensemble for 125 ps (until the lattice parameters reached steady-state) at 300 K and 1 atm. The dimensions of the simulation cell were averaged after steady-state was reached, i.e., over the last 12.5 ps (50 frames) of the NPT simulation, to calculate the system lattice parameters.

For a subset of the force fields, simulations were run to calculate stress-strain behavior, following the method developed in our previous work for crystalline cellulose. [200] After equili-

brating the simulation cell in the NPT ensemble, the system was stretched in one direction (x-, y-, or z-direction) through successive small steps (0.25% strain). After applied deformation, the simulation cell was equilibrated in an NPT ensemble with the stretching direction fixed and the perpendicular directions relaxed for 2.5, 0.25 or 0.025 ps. The relaxation time was determined by the strain step increment (0.25%) divided by the prescribed strain rate. Therefore, the relaxation times modeled here corresponded to overall strain rates of 1×10^{9}, 1×10^{10} or 1×10^{11} s^{-1}. This process was repeated until the total strain reached 25%. The step-wise strain method has been used in previous studies [51, 199, 200, 204, 210] to minimize unphysical mechanical response that may arise due to insufficient time for the atoms to respond to rapid changes in the system size at high strain rates. Note that we also tested a continuous strain rate approach [178] and the results were almost the same (Fig. 3.1).

The stress values at each strain increment were calculated by averaging over the last 10% of the equilibration with that strain increment applied. The same procedure was performed in the three orthogonal directions, x (chain), y (H-bonding) and z (π-stacking). The bulk mechanical properties were then estimated from the resultant stress-strain curves. The elastic modulus was calculated by applying a linear fit to the stress-strain data from 0-2% strain. This calculation was performed over different ranges of strain, as discussed later. The failure strain was the strain where the first polymer chain breaks (the sharp drop of stress-strain curve), which is only possible for the reactive potentials. The ultimate stress was taken from the stress at failure strain. These simulations were repeated three times independently with different random velocity seeds assigned for the atoms in the initial structure before NPT simulation.

2.3 Results and Discussion

2.3.1 Force Field Selection Based on Lattice Parameters

The average value of each lattice parameter (a, b, c, α, β, γ) for the $4\times4\times4$ models of PPTA and PAP5 was determined for each force field. The error was then calculated from the difference between the average lattice parameters in our MD simulation and those reported in the literature measured from XRD reported in Ref. [46]. $Error = \left|\frac{1}{N}\sum l_{MD} - l_{XRD}\right|$, where l is one of the lattice parameters and N is the number of simulation frames averaged. The error for the six lattice parameters for all force fields tested is summarized in Fig. 2.4.

The error analysis shows that most of the force fields tested were able to reproduce the lattice parameters of PPTA with reasonable accuracy (less than 25% cumulative error). For both PPTA and PAP5, with many of the force fields, the largest error was for the a parameter. This is likely due to the limitations of those force fields to accurately capture π-stacking. The exceptions were Liu (largest error for PPTA was α), Wood (largest error for PAP5 was γ), CVFF and OPLS (largest error for PPTA was b and for PAP5 was γ). Also, for most of the force fields, the error was larger for PAP5 than PPTA. Based on this analysis, the Kamat, Liu, Vashisth and OPLS force fields were identified as the most accurate in terms of both PPTA and PAP5 lattice parameters.

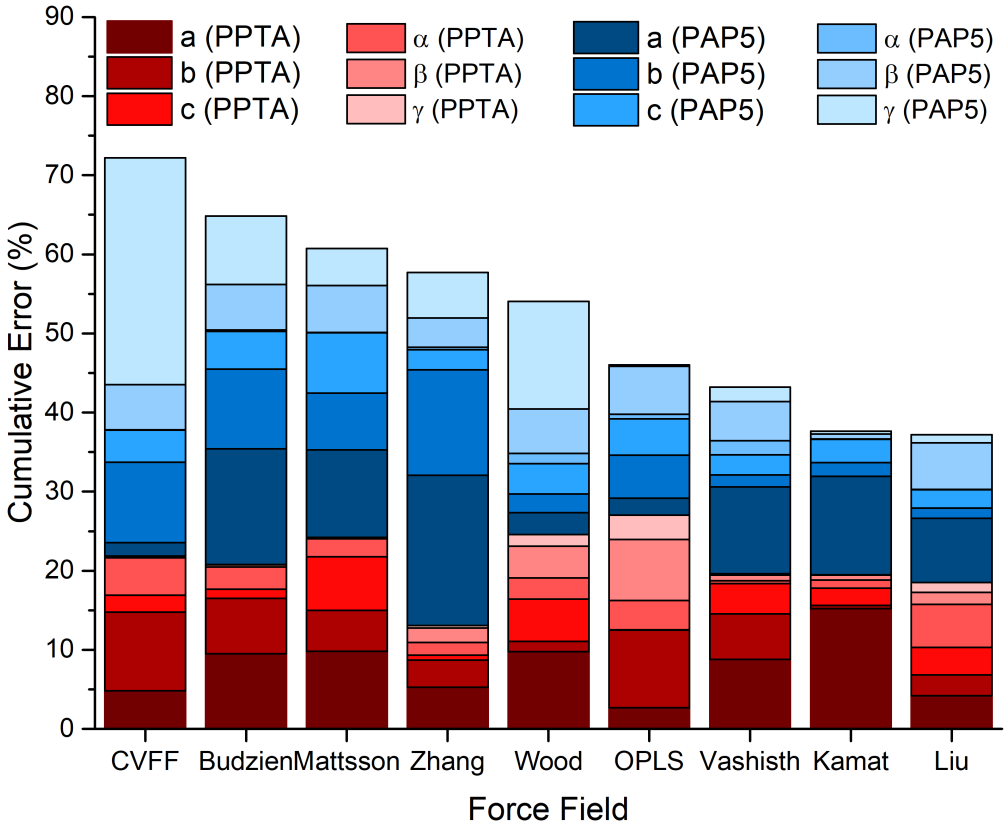

Figure 2.4: Comparison of the cumulative error in the lattice parameters for PPTA and PAP5 of seven reactive and two non-reactive force fields.

2.3.2 Force Field Selection Based on Hydrogen Bonding

Since H-bonding and π-stacking have been found to play important roles in the mechanical properties of polyamides, [46, 67, 99, 112] an appropriate force field should be able to capture these non-bonded interactions accurately. To test this, the radial distribution functions (RDFs) of interatomic distances were calculated for all force fields, except CVFF, which exhibited the least accurate lattice parameters, and was excluded from subsequent analysis. OPLS is the sole non-reactive force field considered henceforth. H-bond length was quantified from RDFs of the non-bonded, nearest-neighbor N–O distance. This definition is widely used [46, 112] because the position of the H atom in N–H···O is difficult to determine experimentally. The reference N–O distances for PPTA and PAP5 were reported to be 3.0 and 2.9 Å in Ref. [46] and [133], calculated from experiments and simulations. The reference N–H···O angle (H-bond angle) for PPTA was reported to be 160°, [133] which is consistent with our results for PPTA (158°) and PAP5 (161°) after equilibrium. Although H-bond strength is determined

by both distance and angle, here we primarily use the N–O distance to quantify H-bonding. π-stacking was measured as the distance in the z-direction (π-stacking-direction) between the centers of two adjacent aromatic rings. The reference value is 3.9 Å for both PPTA and PAP5. [46]

The H-bonding RDFs (N–O distance) calculated for PPTA and PAP5 with each force field are shown in Fig. 2.5. The reference values are identified by vertical dashed lines. The accuracy of the force fields is evaluated by comparing the reference distance to the position of the peak of the RDF. For PPTA, the Wood force field is reasonably accurate, albeit with a wide peak, indicating more variation in atom-atom distances within the model system, i.e., the effect of cumulative error. Also, Budzien and Mattsson slightly overpredict the H-bond distance while Zhang, Vashisth and Liu slightly underpredict it. There is a similar trend in the force fields for PAP5. Based on qualitative analysis of the position of the RDF peaks (closer to the reference value is more accurate) and width of the peak (narrower peaks correspond to less variation from bond-to-bond within the polymers), the best force fields in terms of H-bonding for PAP5 are OPLS, Wood, Zhang, Vashisth, and Liu.

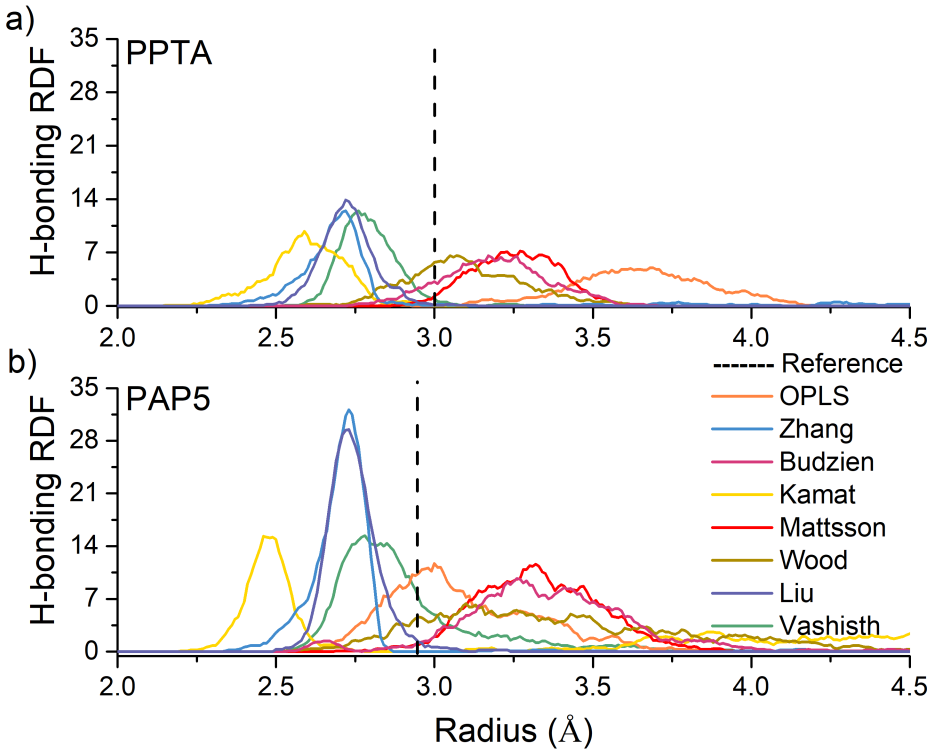

Figure 2.5: Comparison of H-bonding (non-bonded, nearest-neighbor N–O) RDFs calculated for (a) PAP5 and (b) PPTA. The reference [46] H-bond lengths (N–O distances) for PPTA and PAP5 are shown as vertical dashed lines.

2.3.3 Force Field Selection Based on Pi-Pi Stacking

The RDFs for π-stacking in PPTA and PAP5 are shown in Fig. 2.6. The force fields are again evaluated based on the position and width of RDF peaks. Note that the position of the π-stacking RDF peak also reflects the accuracy of the lattice parameter a. As such, force fields that underpredicted the π-π stacking distance also had large error in their prediction of a (see Fig. 2.4). For PPTA, the RDF peaks of Liu and OPLS are the closest to the reference value. For PAP5, Wood and Liu are the most accurate, with relatively narrow peaks.

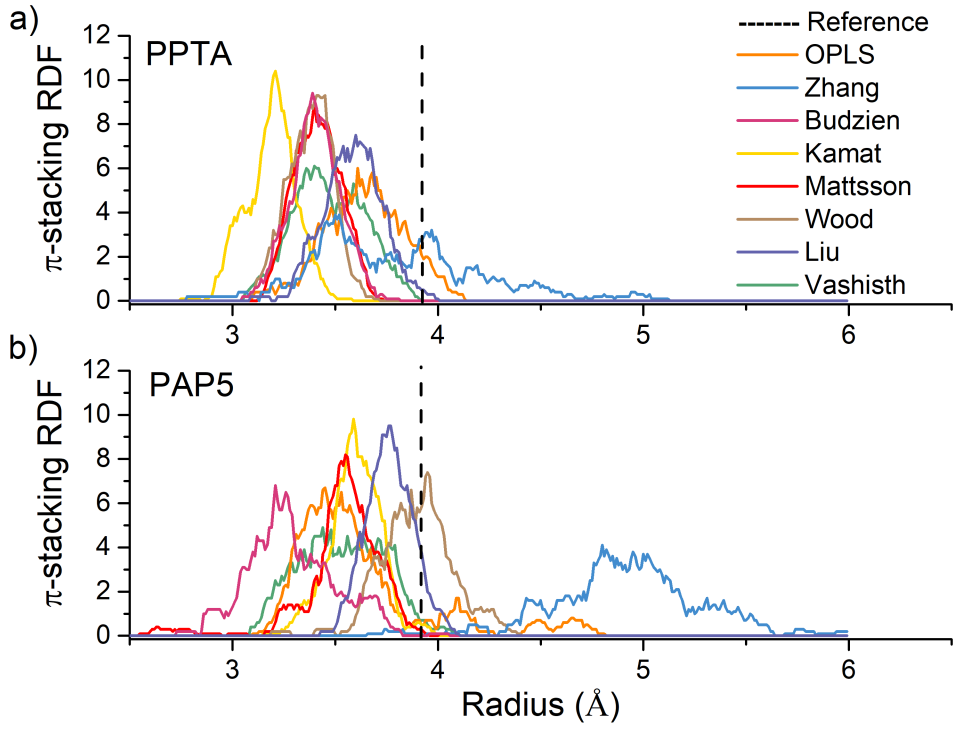

Figure 2.6: Comparison of π-stacking RDFs calculated for (a) PAP5 and (b) PPTA. The reference π-stacking distances [46] are shown as vertical dashed lines.

Based on the evaluation of the various force fields in terms of their ability to accurately reproduce the unit cell lattice parameters, preferred H-bonding and π-stacking distances, as well as XRD patterns, the Liu or Vashisth parameter sets within the ReaxFF formalism performed best. Therefore, the Liu and Vashisth ReaxFF force fields were selected for the stress-strain simulations, discussed below. Stress-strain simulations were also performed with the commonly employed, non-reactive OPLS force field for comparison.

2.3.4 Force Field Selection Based on Stress-strain Response

First, it is necessary to determine the appropriate system size for these simulations to minimize finite size effects while maintaining computational efficiency. The goal is to identify the smallest model that can be used (to maximize computational efficiency) without simulation artifact that may occur if the model is too small due to the unphysical topology of the simulation, e.g., if the model system is too small, a molecule may interact with its own image across the periodic boundary. The stress-strain simulations were run for PPTA with system sizes ranging from 1×1×1 to 8×8×8 with strain applied in the x-, y- and z-directions at a strain rate of 1×10^{9} s^{-1}.

The results for the OPLS, Liu and Vashisth force fields are shown in Fig. 2.9. It can be seen that, for the Liu and Vashisth force fields, the curves start to converge at 4×4×4, which suggests that a system size of 4 × 4 × 4 is big enough to minimize finite size effects (this size model was also used in previous mechanical studies of cellulose nanocrystals [200]). However, for OPLS, although the stress-strain curves in the x-direction start to converge at 1 × 1 × 1, there is no obvious convergence in the data with increasing system size for strain in the y- and z-directions. The sharp drop in stress for some OPLS systems is due to the sudden occurrence of inter-chain slip (Fig. 2.7). The fluctuations in the stress-strain curve for some Vashisth systems in the z-direction starting is due to the occurrence of chain buckling (Fig. 2.8). Regardless, this analysis indicates that a minimum size of 4 × 4 × 4 should be reliable for stress-strain simulations.

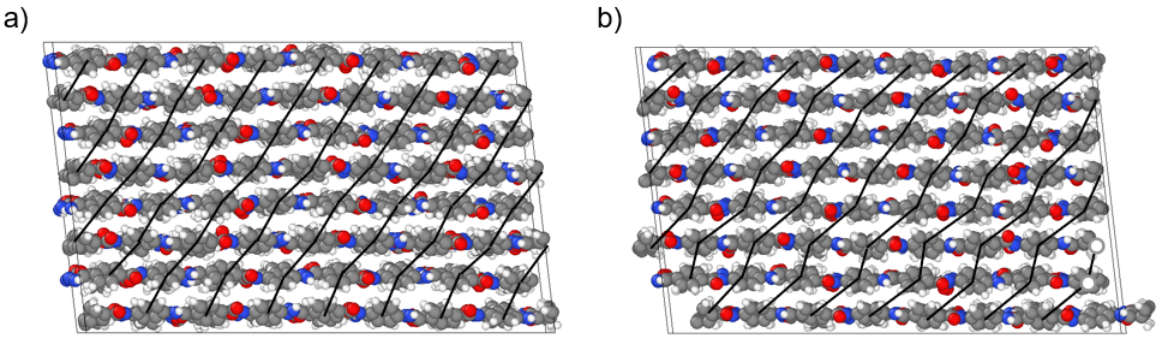

Figure 2.7: Snapshots of PPTA strained in the z-direction (a) before and (b) after inter-chain slip occurs with the OPLS force field. The black lines connecting aromatic rings highlight the relative positions of chains before and after inter-chain slip. This indicates the sharp drop in stress for some OPLS systems is due to the sudden occurrence of inter-chain slip. The origin of this phenomenon may be that the OPLS force field is less accurate in reproducing the inter-chain distance, i.e., the error in the lattice parameter *b* for OPLS is larger than that of ReaxFF, as shown in Fig. 2.4. Specifically, the lattice parameter *b* for OPLS is larger (+0.5 Å) than the experimental value (5.18 Å), while the lattice parameter *b* for Liu is slightly smaller (–0.14 Å) than the experimental value.

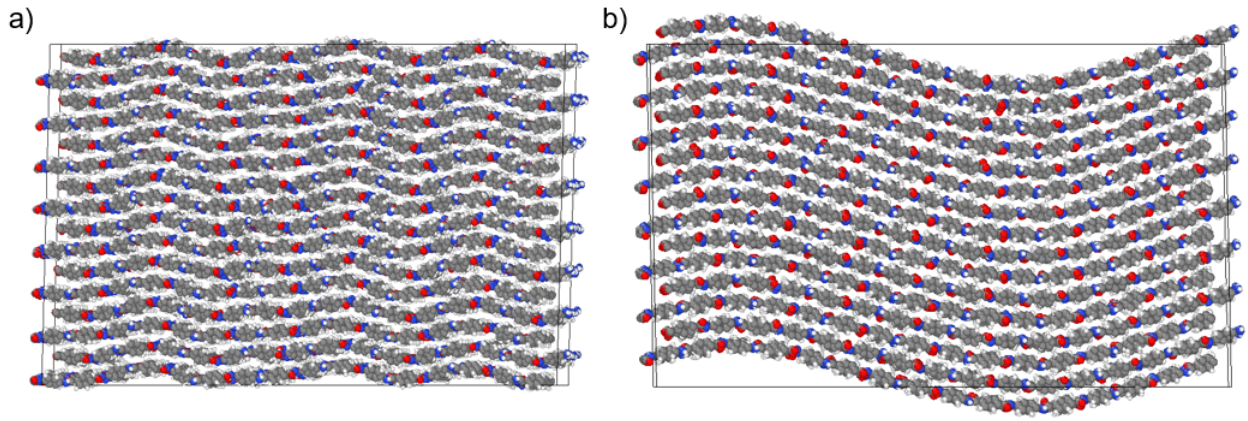

Figure 2.8: Snapshots of PPTA with the (a) Liu and (b) Vashisth force fields at 8% strain in the z-direction. These figures show that the buckling of the chains in the Liu model is of smaller wavelength than the Vashisth model. In addition, from animations of the Vashisth simulations, it was observed that, starting at ~8% when the buckling occurs, the chains act as springs (alternating contraction and extension), corresponding to the fluctuations in the stress-strain curve in Fig. 2.9b. The origin of this phenomenon may be that the Vashisth force field is less accurate in reproducing the π-stacking interactions, i.e., the error of lattice parameter a for Vashisth is larger than that of Liu, as shown in Fig. 2.4.

One obvious difference between the reactive (Liu and Vashisth) and non-reactive (OPLS) force fields is that, in the simulation of strain in the x-direction (chain-direction) the stress drops after ~10% strain with the reactive force fields, but not with OPLS. This is because non-reactive force fields cannot capture breaking covalent bonds [207]. Therefore it is not possible to model ultimate properties using OPLS force field, particularly for strain in the polymer chain direction where material failure must occur through breaking of covalent bonds.

In contrast, ReaxFF utilizes a bond order approach to describe the chemical bonds. Also, ReaxFF models H-bonding with a specific energy functional term [30, 182, 207], which is particularly important for capturing weak H-bonding that is quite common in organic systems. Therefore, using ReaxFF, it is possible to study crystallite failure mechanisms involving primary (covalent) and/or secondary (hydrogen) bond rupture. [112] This indicates that a reactive force field should be used to analyze the mechanical properties of PPTA and PAP5. [162]

Comparing the Liu and Vashisth force fields in Fig. 2.9, the stress-strain trends in the y-direction are similar. However, there are fluctuations in the stress response to strain in the z-direction with some of the larger box sizes with the Vashisth force field, whereas all results with the Liu are quite stable. Recall also that the cumulative error of lattice parameters in Fig. 2.4 was lowest for the Liu force field. Therefore, the $4 \times 4 \times 4$ model and the ReaxFF Liu force field were used in the subsequent investigation of the stress-strain response of PPTA and PAP5.

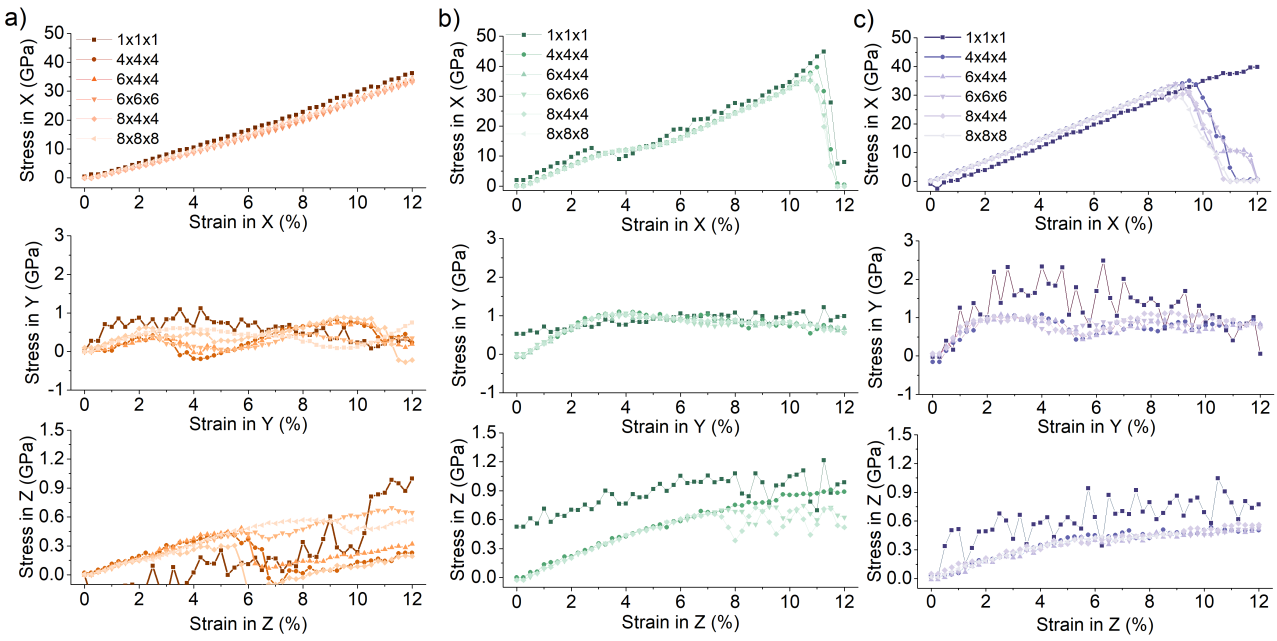

Figure 2.9: Evaluation of the stress-strain curves with the (a) OPLS, (b) ReaxFF Vashisth and (c) ReaxFF Liu force fields for PPTA with simulation box sizes between $1 \times 1 \times 1$ and $8 \times 8 \times 8$ in x-, y- and z-directions.

2.3.5 Force Field Selection Based on XRD Patterns

To further confirm the selected force field was the optimum for reproducing the crystals of the models polyamide systems, we also compared XRDs of PPTA and PAP5 after equilibration using different ReaxFF force field parameter sets as shown in Fig. 2.10 and 2.11. The location and height of each peak of the XRD pattern of both PPTA and PAP5 equilibrated using the ReaxFF Liu force field was the closest to the XRD pattern of the initially-built models (manually tuned to match experimental XRDs as mentioned in earlier). Obviously, the ReaxFF Liu force field had the best performance in reproducing the atomistic crystalline structures of the polyamides in this study.

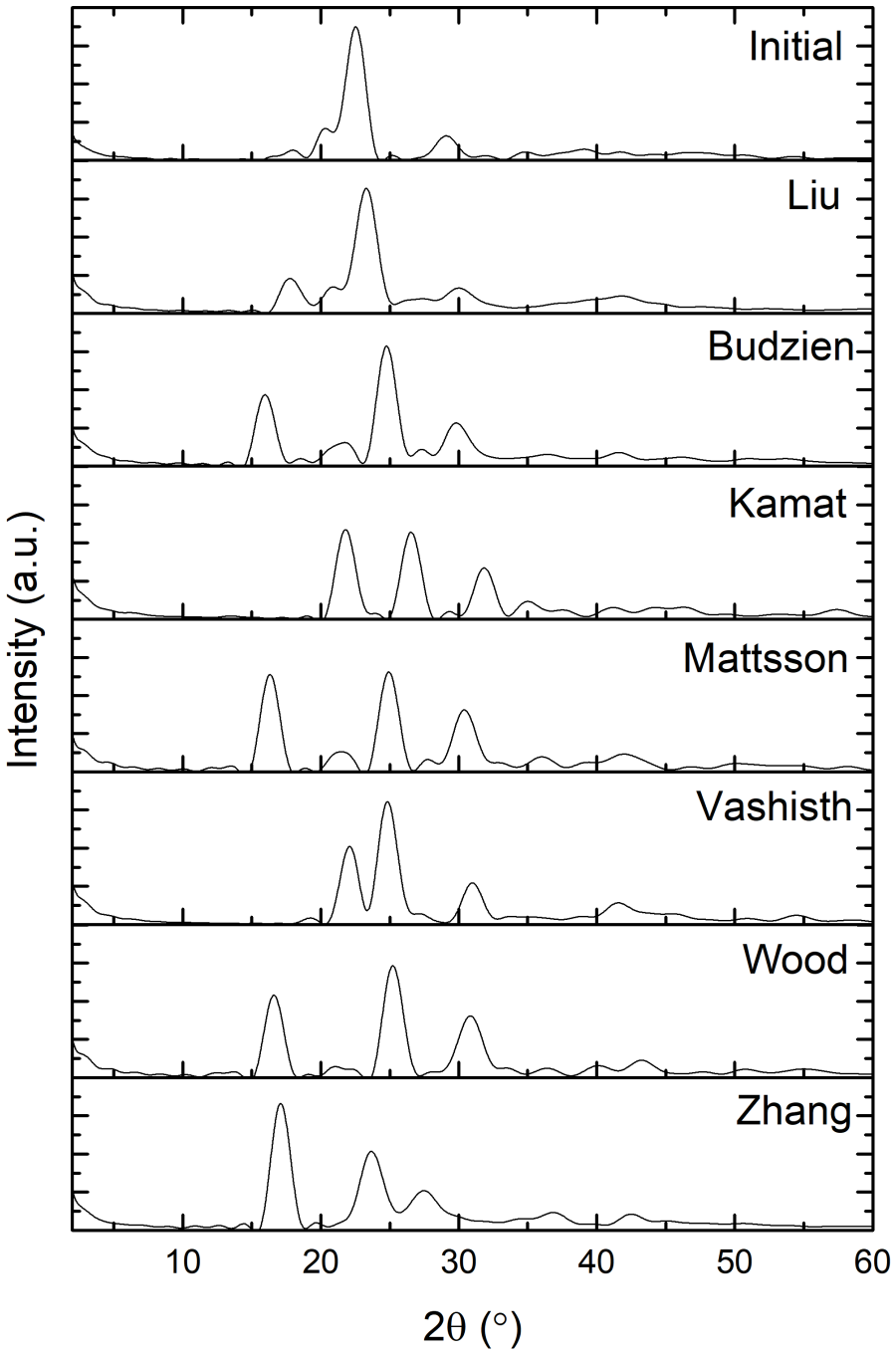

Figure 2.10: XRD patterns of the initially-built structures of PPTA and its structures after equilibration using different ReaxFF force field parameter sets.

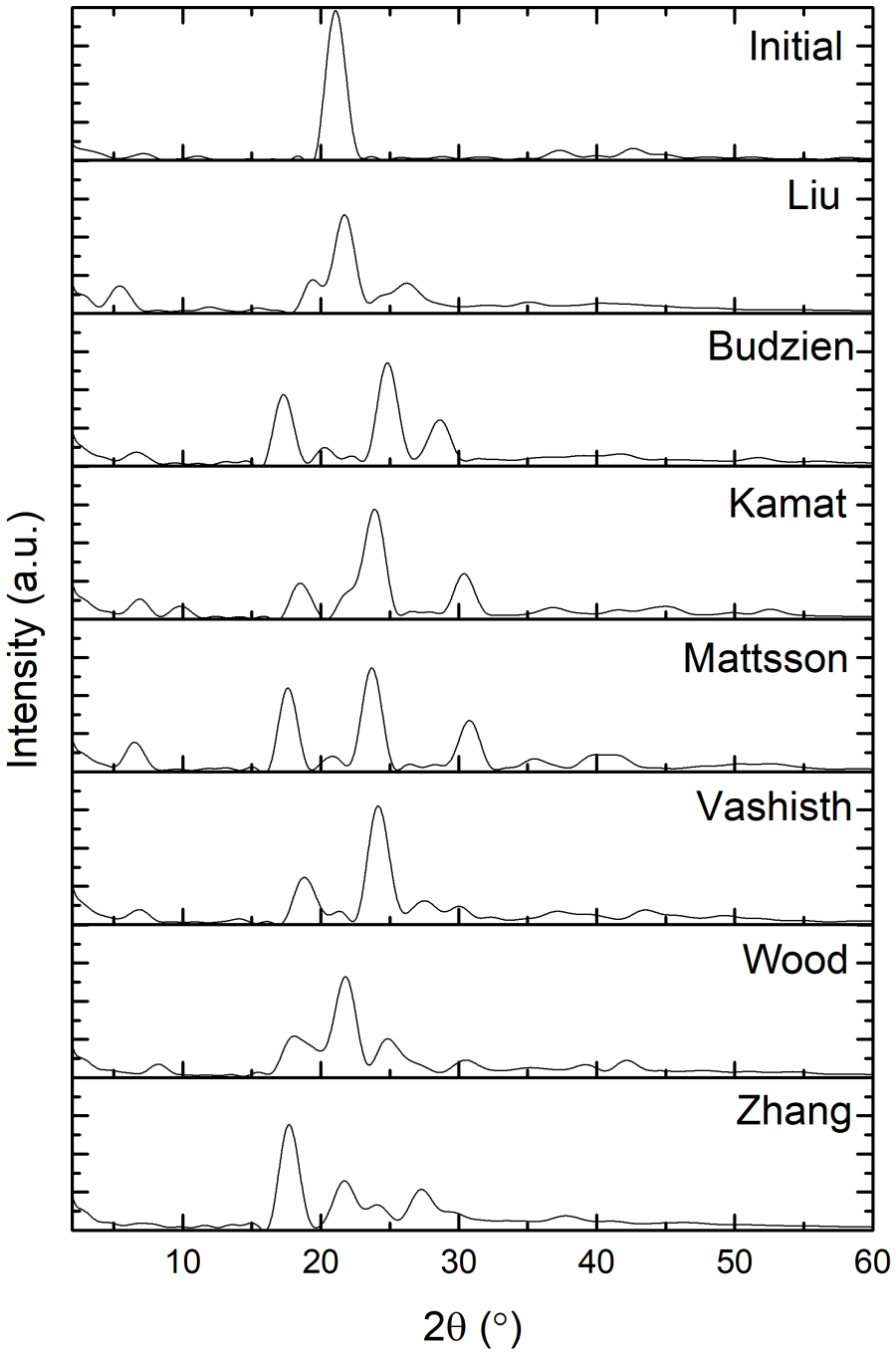

Figure 2.11: XRD patterns of the initially-built structures of PPTA and its structures after equilibration using different ReaxFF force field parameter sets.

2.4 Conclusions

MD simulations were used to study two polyamides, PPTA and PAP5. To ensure accurate modeling of these materials, seven different reactive and two non-reactive force fields were evaluated based on their ability to reproduce the unit cell lattice parameters of the polymer crystals, H-bonding and π-stacking distances within the crystal structure, as well as XRD patterns of the equilibrated structures. The results indicated that the ReaxFF force field developed by Liu was best for studying structure-property relationships of PPTA and PAP5.

Overall, this study demonstrated the importance of force field selection for accurate modeling of polyamides. The force field evaluation also emphasized that models that accurately capture the commonly studied PPTA may not necessarily be suitable for polyamides generally. However, the fact that one of the force fields was suitable for both PPTA and PAP5 suggests that it may be suitable for other polyamides as well.

This study has also established a protocol for selecting an appropriate force field for performing MD simulations of crystalline polymers (and even more generally, crystalline materials) to understand their stress-strain response and mechanical properties.

Chapter 3

Stress-strain Response of PPTA and PAP5 in Chain and Transverse Directions

3.1 Introduction

To enable design of materials with mechanical properties comparable to PPTA, it is necessary to understand the relationships between polymer structure and mechanical behavior. Toward this goal, we used MD simulations to study the molecular scale mechanisms underlying the mechanical response of PPTA and PAP5. Since the suitable force field and model size have been identified as analyzed in Chapter 2, MD simulations can now be performed with confidence to study the mechanical properties of the high-performance polyamides of our interests. In this chapter, the optimum reactive force field, ReaxFF Liu, as identified in Chapter 2 was used to correlate the mechanical response of the materials to changes in H-bonding and π-stacking patterns, as well as how this behavior differed between PPTA and PAP5, by performing stress-strain simulations along the chain and transverse to chain directions.

3.2 Methods

All of the stress-strain simulations were carried out using LAMMPS [141] using the ReaxFF Liu force field [102]. Software OVITO [166] was used for model visualization. The MD time step was 0.25 fs for all simulations. Temperature and pressure were controlled using a Nosé-Hoover thermostat [79] and barostat [80] with damping parameters of 25 fs and 250 fs, respectively. For the ReaxFF force fields the default cut-offs were used (in LAMMPS, nbrhood_cutoff was 0.5 nm and hbond_cutoff was 0.75 nm). First, the unit cell was replicated from $1 \times 1 \times 1$ to $4 \times 4 \times 4$. Next, the replicated simulation cell was energy minimized. Then, simulations were run in the NPT (constant number of atoms, pressure and temperature) ensemble for 125 ps (until the lattice parameters reached steady-state) at 300 K and 1 atm for equilibration.

After equilibrating the simulation cell in the NPT ensemble, the system was stretched in one direction (x-, y-, or z-direction) through successive small steps (0.25% strain). After ap-

plied deformation, the simulation cell was equilibrated in an NPT ensemble with the stretching direction fixed and the perpendicular directions relaxed for 2.5, 0.25 or 0.025 ps. The relaxation time was determined by the strain step increment (0.25%) divided by the prescribed strain rate. Therefore, the relaxation times modeled here corresponded to overall strain rates of 1×10^{9}, 1×10^{10} or 1×10^{11} s^{-1}. This process was repeated until the total strain reached 25%. The step-wise strain method has been used in previous studies [51, 199, 200, 204, 210] to minimize unphysical mechanical response that may arise due to insufficient time for the atoms to respond to rapid changes in the system size at high strain rates. Note that we also tested a continuous strain rate approach [178] and the results were almost the same (Fig. 3.1).

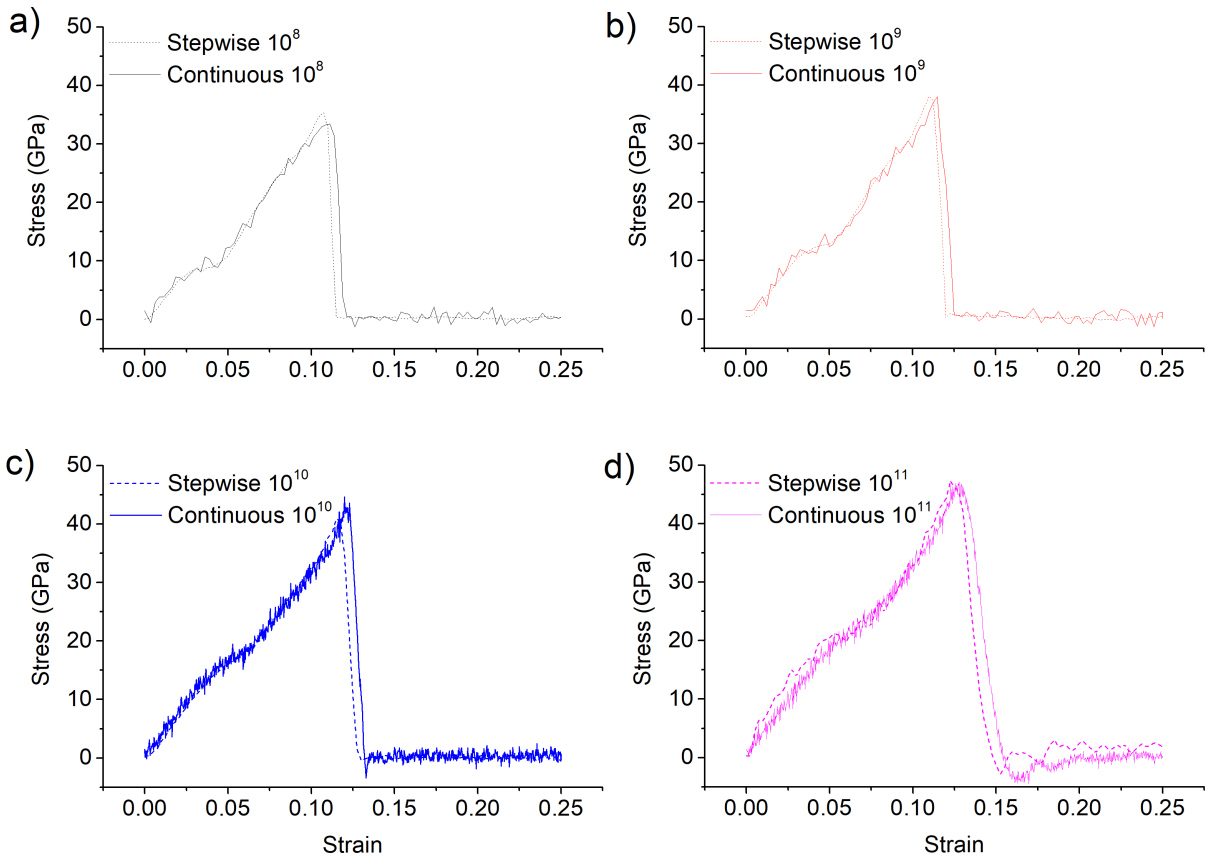

Figure 3.1: Comparison between stepwise stretching and continuous stretching approaches at four different strain rates: (a) 1×10^{8} s^{-1}, (b) 1×10^{9} s^{-1}, (c) 1×10^{10} s^{-1}, and (d) 1×10^{11} s^{-1}. The stress-strain curves obtained from the two approaches are almost the same. The above examples are from simulations of strain of PPTA in the x-direction with the Vashisth force field.

The stress values at each strain increment were calculated by averaging over the last 10%

of the equilibration with that strain increment applied. The same procedure was performed in the three orthogonal directions, x (chain), y (H-bonding) and z (π-stacking). The bulk mechanical properties were then estimated from the resultant stress-strain curves. The elastic modulus was calculated by applying a linear fit to the stress-strain data from 0-2% strain. This calculation was performed over different ranges of strain, as discussed later. The failure strain was the strain where the first polymer chain breaks (the sharp drop of stress-strain curve), which is only possible for the reactive force fields. The ultimate stress was taken from the stress at failure strain. These simulations were repeated three times independently with different random velocity seeds assigned for the atoms in the initial structure before NPT simulation.

3.3 Results and Discussion

3.3.1 Mechanical Properties

Fig. 3.2 shows the mechanical properties (elastic modulus, ultimate stress, and failure strain) of PPTA and PAP5 calculated from simulations of strain in the x-direction (chain-direction) run at three different strain rates (1×10^{9}, 1×10^{10} and 1×10^{11} s^{-1}) with the ReaxFF Liu force field. For PPTA, the values obtained from simulations are compared to properties reported from previous experimental studies [28, 38, 49, 99, 147]. In general, the magnitude of strain-rate-dependent mechanical properties can appear larger when computed by molecular simulation. This is because the inherently small time scales accessible by molecular simulation lead to very high strain rates (typically > 10^{8} s^{-1}). [103, 159, 175, 218] For example, it was reported that chain direction mechanical properties of PPTA increase with strain rate, [111, 159, 188, 191, 218] consistent with the results in Fig. 3.2. This strain-rate-dependence has been attributed to the intermolecular slippage and plastic flow that occurs at low strain rates, resulting in more energy dissipation. [162] In addition, our model systems are infinite chain-length and free of defects (e.g., chain ends, stacking faults, or impurities), in contrast to physical materials. It has been reported that chain end defects and different defect distribution patterns could reduce the ultimate stress and failure strain, and that the axial modulus increases with increasing chain length. [112] Moreover, in higher order structures such as fibrils, where the morphology is more complicated, chain and/or crystal misorientation might affect material properties. For all these reasons, the simulation-predicted mechanical properties are higher than values obtained from physical experiments.

Although we do not have experimental data for PAP5, the simulations enable comparison of PPTA and PAP5 at high strain rates. Like PPTA, the magnitudes of the ultimate stress and failure strain increase with increasing strain rate. However, at any strain rate, PAP5 has larger failure strain and ultimate stress than PPTA, but a smaller elastic modulus. Although the OPLS force field cannot simulate mechanical failure due to bond breakage, it was used to calculate elastic modulus and showed higher stiffness for PPTA than PAP5 (223 ± 8 GPa for PPTA and 120 ± 3 GPa for PAP5), confirming the direction and relative magnitude of the trend observed from ReaxFF. These results indicate that the methylene units in the PAP5 reduce stiffness but

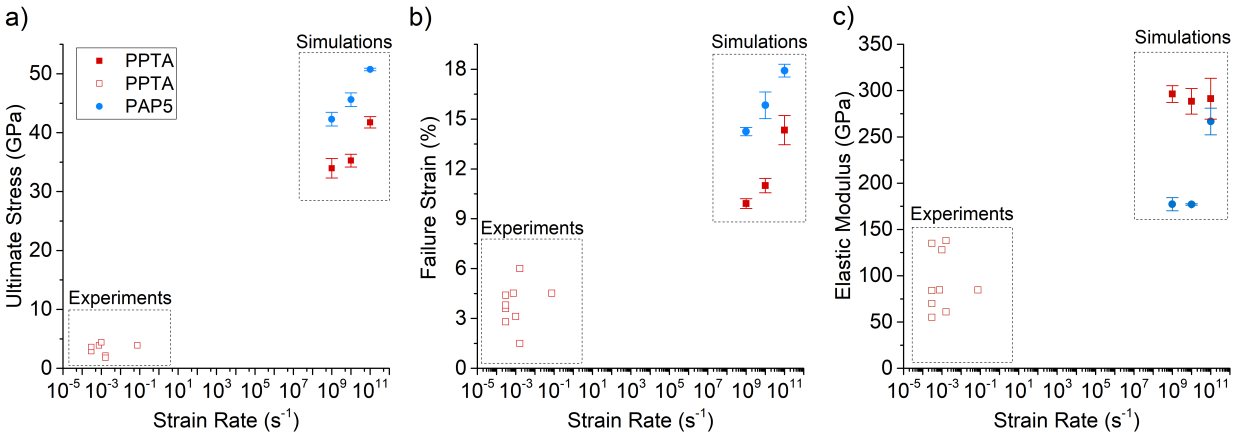

Figure 3.2: (a) Ultimate stress, (b) failure strain and (c) elastic modulus (calculated from 0 to 2% strain) from simulations of PPTA and PAP5 strained in the chain direction at three different strain rates (1×10^{9}, 1×10^{10} and 1×10^{11} s^{-1}) using the ReaxFF Liu force field. The error bars reflect the standard deviation calculated from three independent simulations. Also shown are representative data points for PPTA from experiments [28, 38, 49, 99, 147].

increase the failure strain. However, as discussed later, the elastic response of PAP5 is strain dependent, so the stiffness calculation depends on the strain range for which the linear fit is performed. These trends are investigated next.

3.3.2 Chain Direction Strain Response

Figs. 3.4a-b show the stress-strain behavior of PPTA and PAP5 for strain up to 25% in the x-direction at a strain rate of 1×10^{9} s^{-1}. The corresponding mechanical properties are summarized in Table 3.1. The mechanical properties of PPTA predicted by our simulations are similar to the range of results reported in previous MD simulation studies with ReaxFF: elastic modulus 325-360 GPa, ultimate stress 32-35 GPa, and failure strain ~10%. [34, 35, 112, 208]

Consistent with Fig. 3.2, failure stress and strain are larger for PAP5 than PPTA. However, the elastic modulus comparison is more complicated. The stress-strain curve for PPTA (Fig. 3.4a) has only one linear regime from zero strain to its failure strain at ~10%. In contrast, the stress-strain curve for PAP5 (Fig. 3.4b) can be separated into two linear regimes: low-strain (0 to ~4%) and high-strain (~5 to ~14%). Analysis of the lattice parameters during strain showed that γ increased sharply at this inflection point, indicating a structural transition, specifically, a contraction in the cross-sectional area (yz plane). This contraction also resulted in a strengthening of the H-bonding, quantified by a small decrease of the average H-bond length from 2.82 Å before the transition to 2.75 Å after the transition. The inflection point between these two regimes does not indicate yield, as confirmed by simulations in which the system was strained to 7.5% and then allowed to relax in the NPT ensemble at 300 K and 1 atm without constraints. When

Properties in the x-direction	PPTA	PAP5
All-strain modulus (GPa)	362±9	310±3
Low-strain modulus (GPa)	293±18	174±3
High-strain modulus (GPa)	375±5	436±10
Failure strain (%)	9.9±0.3	14.3±0.3
Ultimate stress (GPa)	34.0±1.6	42.3 ± 1.1

Table 3.1: Mechanical properties calculated from simulations of strain in the x-direction. For the elastic modulus, low-strain refers to 0-2% strain, high-strain refers to the last 5% strain prior to failure, and all-strain refers to all strain prior to failure. The errors are the standard deviation calculated over three independent repeat simulations.

the constraint was released, the stress dropped to zero and the lattice parameters returned to their original pre-strain values in approximately 10 ps (Fig. 3.3). This indicates that the deformation is elastic and PAP5 crystals exhibit two linear elastic regimes before failure.

If the two elastic regimes in Fig. 3.4b are considered separately, the low-strain modulus is 174 GPa and the high-strain value is 436 GPa. Although PPTA exhibits some strain hardening, there is no sharp inflection point and the increase of modulus with strain is much lower than that observed for PAP5. As a result, the modulus of PAP5 is smaller than that of PPTA at low strain but the opposite is observed at high strain.

The RDFs for intermolecular H-bonding and π-stacking within PAP5 and PPTA at different strains are shown in Figs. 3.4c-j. The H-bonding RDF peak of PPTA (Figs. 3.4c-d) shifts to larger radii as the chains are being strained. However, the H-bonding RDF peak of PAP5 (Figs. 3.4e-f) first shifts to smaller radii at low strains then shifts to larger radii at higher strains. Regarding the π-stacking RDFs, for PPTA, the peak position changes very little with strain, but the peak widens. For PAP5, the π-stacking RDF first shifts to the left at low strains and then becomes narrower as it is strained.

Snapshots from the simulations of PPTA and PAP5 at the strains identified in Fig. 3.4 are shown in Fig. 3.5. The snapshots show that both PPTA and PAP5 respond elastically at low strain followed by chain breaking at high strain. However, there are differences between PAP5 and PPTA observed as well. Specifically, it can be seen that, at zero strain, the PPTA is fully extended and then the chains are stretched as strain is applied. In contrast, the PAP5 chains have a wavy structure at zero strain. The waves are removed by extension at low strain and then the covalent bonds themselves begin to stretch at larger strain.

The conformations of PPTA and PAP5 reflect two polymer conformations commonly reported in the literature [78, 84, 98, 105, 116, 119, 131, 132, 143, 154, 170, 173, 180, 190, 198]: extended and wavy. Note that a variety of different terms have been used to describe these two conformation in the literature, but here the terms extended and wavy will be used. A wavy conformation is due to the methylene groups acting as spacers between the hydrogen-bonded

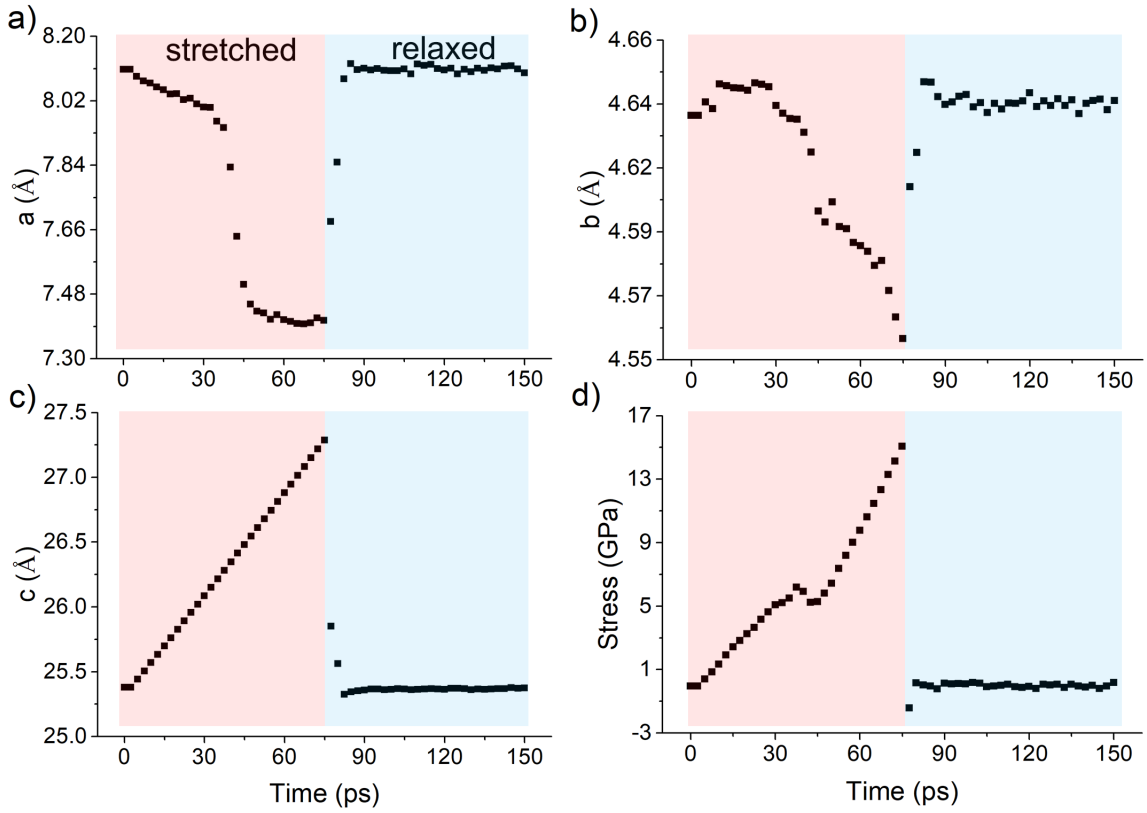

Figure 3.3: (a-c) Lattice parameters and (d) stress of PAP5 as functions of time during the stretching and relaxation processes. The system was first stretched to 7.5% strain (shaded red) and then allowed to relax by running NPT at 300 K and 1 atm until the system reached 0% strain (shaded blue). The stress and lattice parameters return to their equilibrium values almost immediately after the strain is released. This indicates that the sample is not plastically deformed which indicates that the inflection point (which occurs around 4% strain) is not yield.

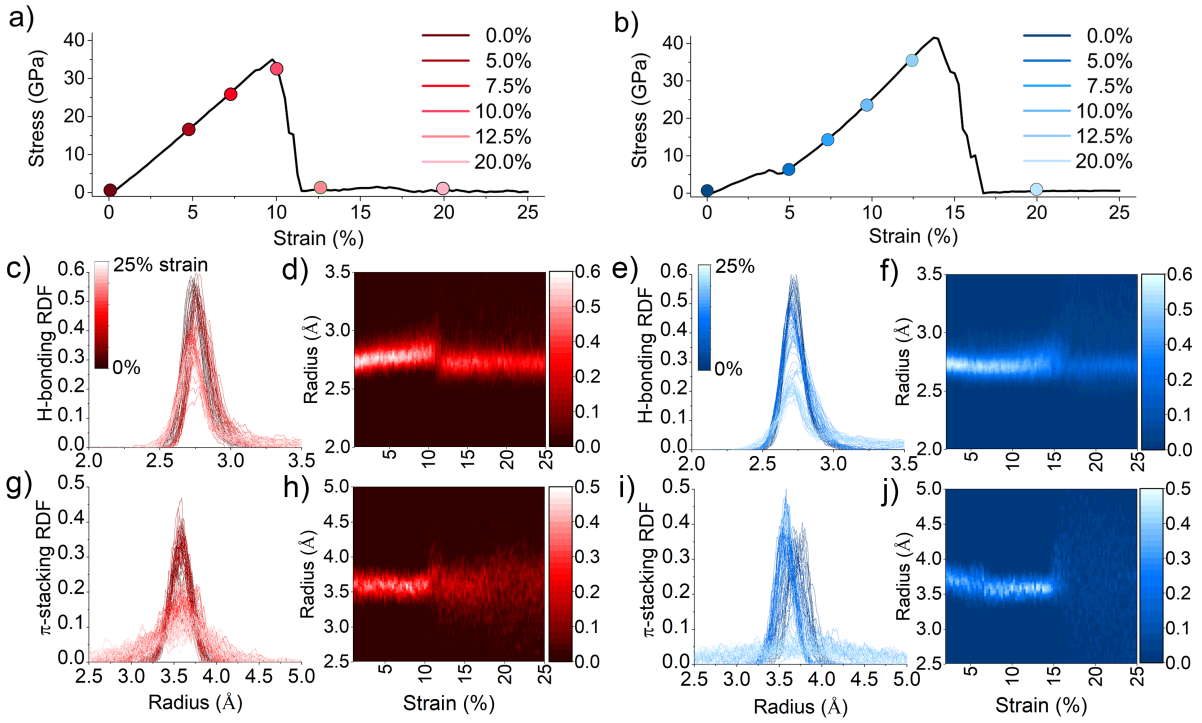

Figure 3.4: Stress-strain behavior (a and b) and RDF profiles and heat maps for H-bonding (c, d, e, and f) and π-stacking (g, h, i, and j) for PPTA (c, d, g, and h) and PAP5 (e, f, i, and j) strained in the x-direction. The RDFs are normalized by the number of bonds per unit cell. Movies S1 and S4 showing the evolution of the stress and RDF distributions as well as the time evolution of the models are available in the Supplemental Information.

amide groups, which increases the conformational freedom of the polymer chains. [46, 71] A previous investigation of twenty-five different polymers (including polyethylene (PE) and poly tetrafluoroethylene (PTFE)) revealed that, at low strain, the polymer conformations are closely related to the force required to stretch them. [154].

It has been shown that polymers with a loose wavy conformation exhibit a much lower stiffness than polymers with extended conformations because extended conformations have stronger H-bonds between adjacent chains. [98, 154, 170] Another study examined the relationship between the elastic modulus, molecular conformation and flexibility of the chains of PPTA and related polymers. [173] They found that PPTA chains are fully extended, resulting in a high elastic modulus. The same study compared the extended and wavy forms of polyethylene oxybenzoate (PEOB) and found that the former had a much higher elastic modulus due to its extended conformation. [173]

To quantify waviness and its evolution with strain, we identified the positions of the backbone atoms in each chain in the yz plane. This analysis excluded the H and O atoms, and the

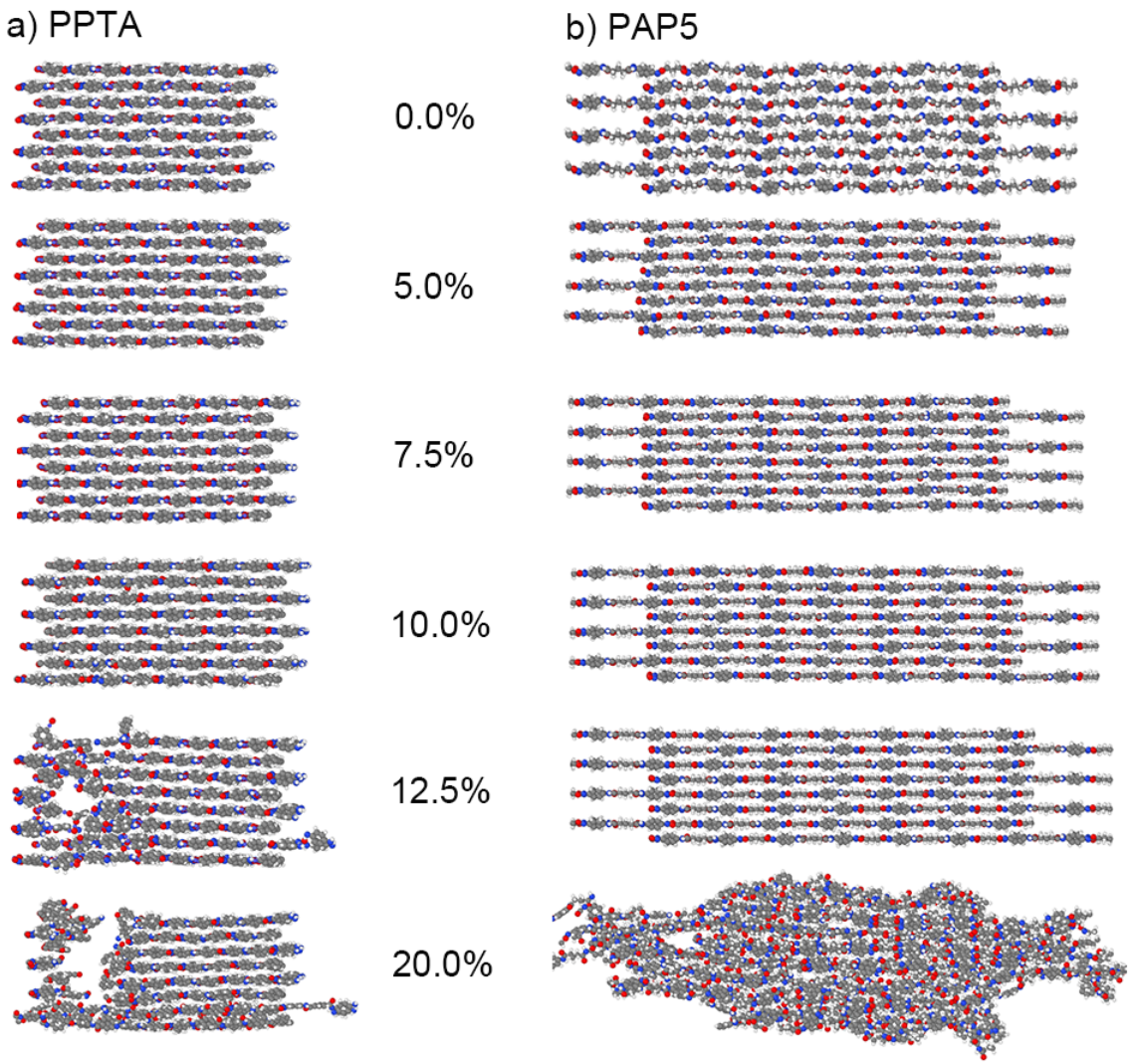

Figure 3.5: Snapshots of (a) PPTA and (b) PAP5 while strained in x-direction with a strain rate of 1×10^{9} s^{-1} at 0, 5, 7.5, 10, 12.5 and 20% strains with the Liu force field as viewed from the y-direction. Snapshots correspond to the solid circles on the stress-strain plots in Fig. 3.4.

C atoms in the aromatic rings. The results are shown in Fig. 3.6. In this figure, all the chains in the crystal are aligned by relocating their centroid to the origin of the yz plane at each strain.

At zero strain, the size and shape of the distributions of atoms in PPTA and PAP5 are different. The PPTA atoms fall into two, relatively small circular regions ($|y| < 1$ Å and $|z| < 0.75$ Å). In contrast, the PAP5 atom distribution is much more spread out ($|y| < 0.75$ Å and $|z| < 1.25$ Å), showing that the atoms are further from the chain axis, i.e., exhibiting a wavy conformation. The PAP5 atom distribution is also asymmetric, indicating there is some rotation of methylene units in the yz plane; this is not observed for the PPTA.

Once strain is applied, the size and shape of the atom distribution for the PPTA changes little, consistent with its extended conformation which accommodates strain by stretching covalent bonds. However, the distribution of atoms in PAP5 becomes smaller and more symmetric with increasing strain. This indicates that strain is initially accommodated by elongation and rotation of the wavy chains.

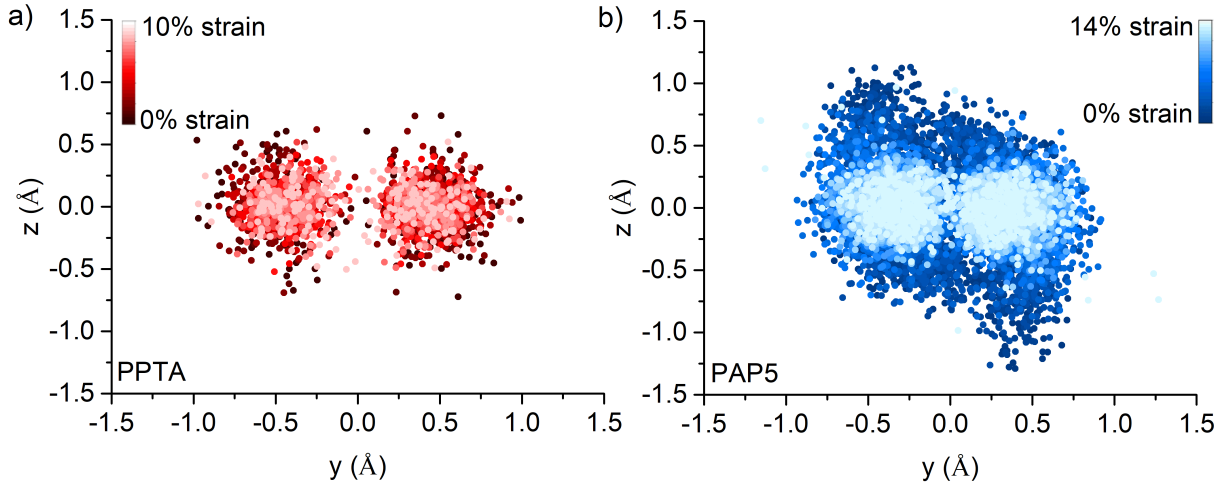

Figure 3.6: Position of atoms in the chains projected on the yz plane for (a) PPTA and (b) PAP5, where the centroid of each chain is manually moved to the origin of the yz plane. The hydrogen and oxygen atoms, and the carbon atoms in aromatic rings are excluded in this calculation.

The initial waviness of the PAP5 explains its smaller low-strain stiffness since less force is needed to elongate and rotate the methylene segments in PAP5 than to strain the covalent bonds within the extended chains of PPTA. This can be confirmed by the H-bonding and π-stacking RDFs in Figs. 3.4c-j. The H-bonding RDF peak position for PAP5 moves to the left (indicating stronger intermolecular interactions due to more ordered chains) with increasing strain as the waviness is removed. In contrast, for PPTA, the H-bonding peak position moves to the right and broadens (indicating weaker intermolecular interactions due to the loss of H-bond registry) as the covalent bonds within the chains are strained. A similar trend can be

found in the π-stacking RDFs at low strain in Figs. 3.4g-j, where the peak for PAP5 shifts to the left and becomes narrower (strengthening π-stacking interactions) as the wavy chains are extended.

The difference between the initial conformations of PAP5 and PPTA also explains the larger failure strain of PAP5 than PPTA. Specifically, the larger failure strain is due to the initial waviness of PAP5, which enables it to accommodate the initial strain by extension of the wavy chains such that stretching of covalent bonds does not begin until higher strains.

After the initial 5% strain, the conformations of PPTA and PAP5 are similar. Therefore, differences in their high-strain stiffness and ultimate stress, both of which are larger for PAP5 than PPTA, cannot be directly explained by the waviness argument. It has been reported that amide bonds contribute significantly to the chain direction elastic modulus of materials such as cellulose and polyamides. [53, 171]. Also, the amide group C–N bond has been identified as the weakest bond in the polymer chain backbone of PPTA, [112] consistent with the observation that failure of both PPTA and PAP5 in the chain direction occurred through breaking of the C–N bond. Therefore, C–N bond is expected to be the limiting factor of the overall strength of PPTA and PAP5. The average C–N bond length in PPTA is 1.44 Å and is 1.43 Å for PAP5 at failure strain, suggesting that the C–N bonds in PAP5 may be slightly stronger than those in PPTA.

A higher degree of chain alignment (less conformational freedom) is known to increase tensile strength and elastic modulus in polymers [53] and the high degree of alignment of PPTA has been attributed to intermolecular H-bonding. [99, 112, 113, 160, 209] From the analysis of the coplanarity of aromatic rings in the PPTA and PAP5 crystals at each strain (Fig. 3.7), it can be seen that, before failure, the ring-ring angle increased slightly (less aligned) with strain in PPTA but decreased (more aligned) in PAP5 as the chains transitioned from wavy to extended before plateauing in the high-strain regime. This phenomenon contributes to the sharp increase in the modulus of PAP5 in the high-strain regime.

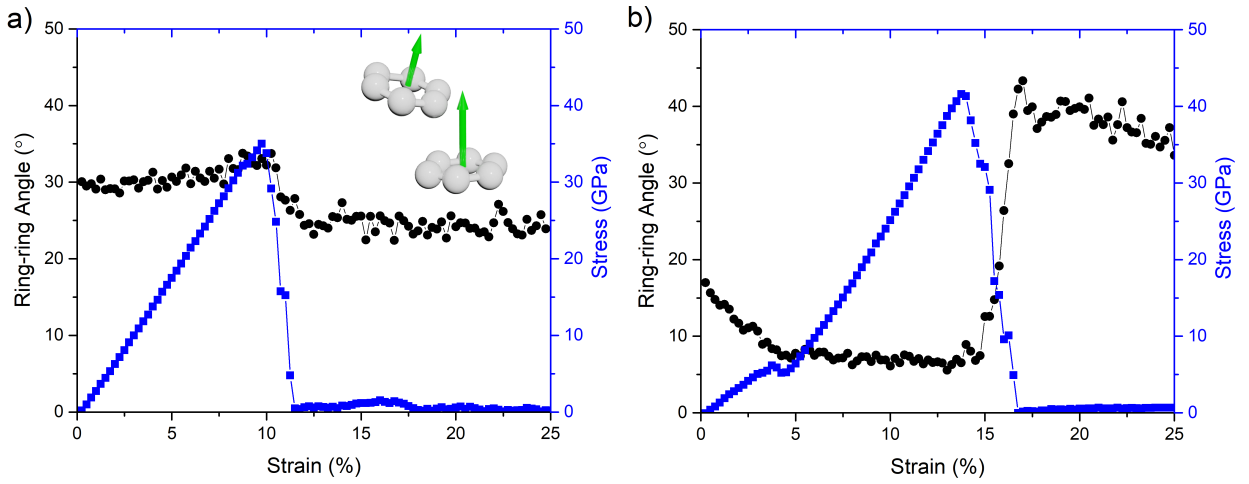

Figure 3.7: Stress and ring-ring angle as functions of strain in the x-direction for (a) PPTA and (b) PAP5. Ring-ring angle is the average angle between each pair of adjacent rings (the angle between the two green arrows in the inset) from two adjacent sheets. It is a measurement of the coplanarity of rings in the crystal, i.e., smaller angle corresponds to more coplanar.

3.3.3 Response to Strain in the Transverse Directions

The mechanical properties of PPTA and PAP5 exhibit anisotropy, as shown in Fig. 2.9. The elastic modulus and ultimate stress in the x-direction (chain-direction) are expected to be much higher than those in transverse directions since intramolecular covalent bonds resist strain in the x-direction but do not contribute to material properties in the y- and z-directions (directions aligned with H-bonding and π-stacking, respectively). Such anisotropy in mechanical properties has been reported for many other high-performance fibers [72] and explained by the high degree of chain orientation in the axial direction. [201] The mechanical properties of PPTA and PAP5 calculated from simulations of strain in the transverse directions are summarized in Table 3.2. The elastic modulus of PPTA in the transverse directions were calculated to be 8 GPa and 60 GPa in the y and z directions, respectively, consistent with the range of 4.1-52 GPa reported in a previous study. [150]

The stress-strain curves and RDFs for strain in the y-direction are shown in Fig. 3.8, with corresponding snapshots in Fig. 3.9. Strain in the y-direction is primarily accommodated by the H-bonds between the chains. Therefore, as the crystal is strained, the peak of the H-bonding RDFs decreases in height and shifts to the right in Figs. 3.8c-f, indicating weakening and then breaking of H-bonds. The π-stacking RDF peak shifts to the left with increasing strain, as shown in Figs. 3.8g-j. This reflects Poisson contraction in the z-direction.

In the y-direction, both the Young's modulus and ultimate stress are larger for PPTA than for PAP5. PPTA has stronger H-bonding than PAP5 due to the more favorable chain conformations of PPTA; this conclusion is also supported by the experimental work of Deshmukh et

Properties	PPTA	PAP5
y-direction		
Elastic modulus (GPa)	60	26
Yield strain (%)	3.0	6.5
Yield stress (GPa)	1.21	1.55
Failure strain (%)	24.3	24.8
Ultimate stress (GPa)	1.31	0.90
z-direction		
Elastic modulus (GPa)	8.4	13.2
Yield strain (%)	~5.5	~6.2
Yield stress (GPa)	~0.43	~0.68
Failure strain (%)	25	19
Ultimate stress (GPa)	0.72	0.99

Table 3.2: Mechanical properties calculated from simulations of strain in the y- and z-directions.

al. [46] Since y-direction strain is in the direction of the H-bonding, the higher stiffness and strength of PPTA are directly attributable to its stronger intermolecular H-bonding.

Unlike the x-direction behavior, the crystals exhibited a yield point when strained in the y-direction. Yield occurred at a higher strain and larger stress for PAP5 compared to PPTA, so this trend could not be explained by H-bonding. However, analysis of the deformation (see movies in Supplemental Information) indicated that yield occurred through different mechanisms for these two polymers. For PAP5, yield occurred through breaking of its relatively weaker H-bonds while, for PPTA, the strong H-bonds resisted breaking and, instead, inter-sheet slip occurred at the yield point (see Supplemental Information Fig. 3.10).

Inter-sheet slip resulted in a step-change reduction in the ring-ring angle, which brings the pi-pi stacking into better registry. No such mechanism is active in PAP5, which instead yields by H-bond breaking. Hence, the stress at which slip occurs in PPTA is lower than the stress for H-bond breaking in PAP5.

The stress-strain response and RDFs for strain in the z-direction are shown in Fig. 3.13, with simulation snapshots in Fig. 3.14. The response of the polymers to strain in the z-direction is dominated by the π-stacking interactions between adjacent sheets. So, there is little change in the H-bonding RDFs with strain (Figs. 3.13c-f). In the π-stacking RDFs, the peak is observed to initially shift to the right (0-5% for PPTA and 0-10% strain for PAP5), corresponding to increasing distance between the sheets (Figs. 3.13g-j).

This trend continues until failure for PAP5. However, at about 8% strain, the PPTA chains buckle at alternating amide linkages (Fig. 3.14a). This results in a split of the π-stacking peak for PPTA into two (Figs. 3.13h) since the buckling causes some aromatic rings to move closer

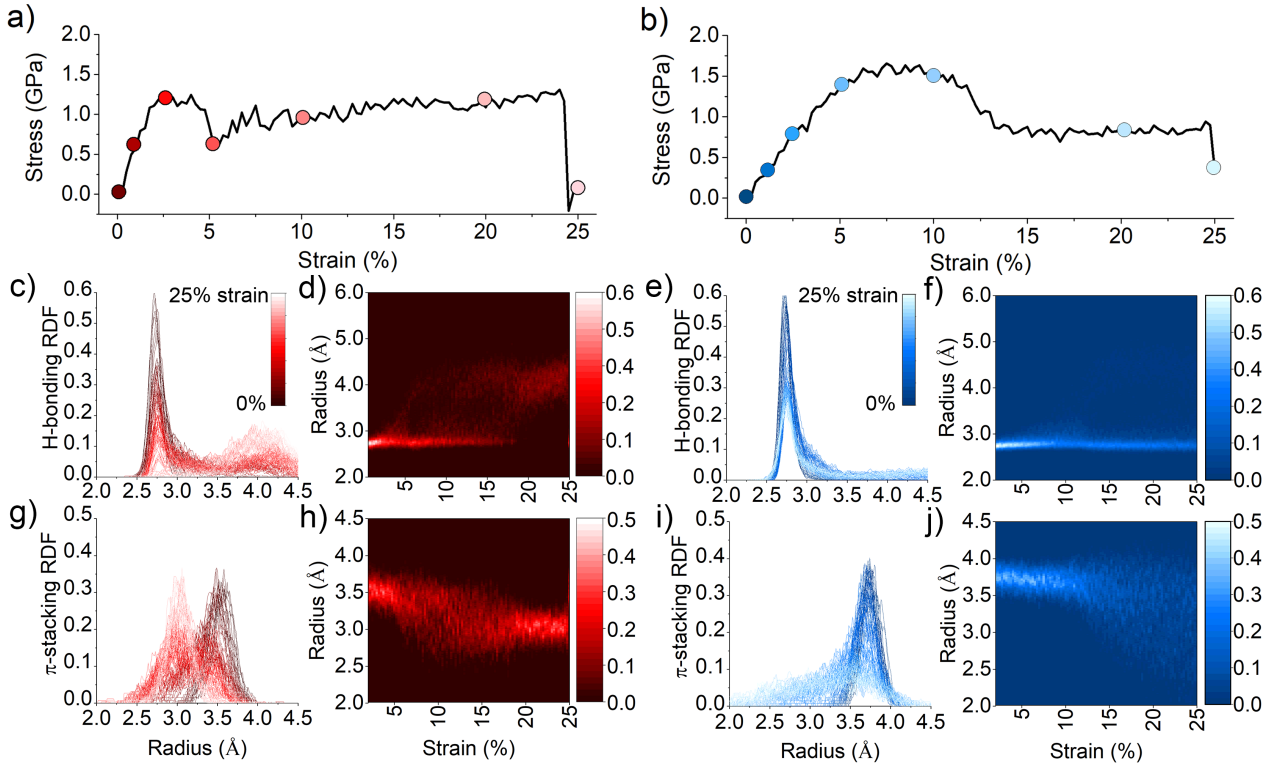

Figure 3.8: Stress-strain behavior (a and b) and RDF profiles and heat maps for H-bonding (c, d, e, and f) and π-stacking (g, h, i, and j) for PPTA (a, c, d, g, and h) and PAP5 (b, e, f, i and j) strained in the y-direction. The RDFs are normalized by the number of bonds per unit cell. Movies S2 and S5 showing the evolution of the stress and RDF distributions as well as the time evolution of the models are available in the Supplemental Information.

together and others farther apart (Fig. 3.11). In contrast, the sheets move gradually apart until around 20% strain, at which point they separate in the middle leaving two groups of sheets with approximately equilibrium π-stacking distance (Fig. 3.14b and 3.13j). These different behaviors of PPTA and PAP5 in response to z-direction strain can be attributed to the better coplanarity of the PAP5 (Fig. 3.12), which corresponds to stronger intermolecular π-stacking interactions that enable it to resist buckling.

The Young's moduli in the z-direction of PPTA and PAP5 are the smallest among the three directions of strain (x, y and z) because π-stacking is weaker than covalent bonding (that resists strain in x) and H-bonding (that resists strain in y). In the z-direction, the stiffness of PAP5 (13 GPa) is slightly larger than that of PPTA (8 GPa). This high stiffness of PAP5 is explained by the fact that its aromatic rings are more coplanar (Fig. 3.12), which corresponds to stronger intermolecular π-stacking interactions and increases the modulus in the z-direction.

As seen in Figs. 3.13a-b, PAP5 exhibits a failure strain at 20%, but PPTA does not fail until

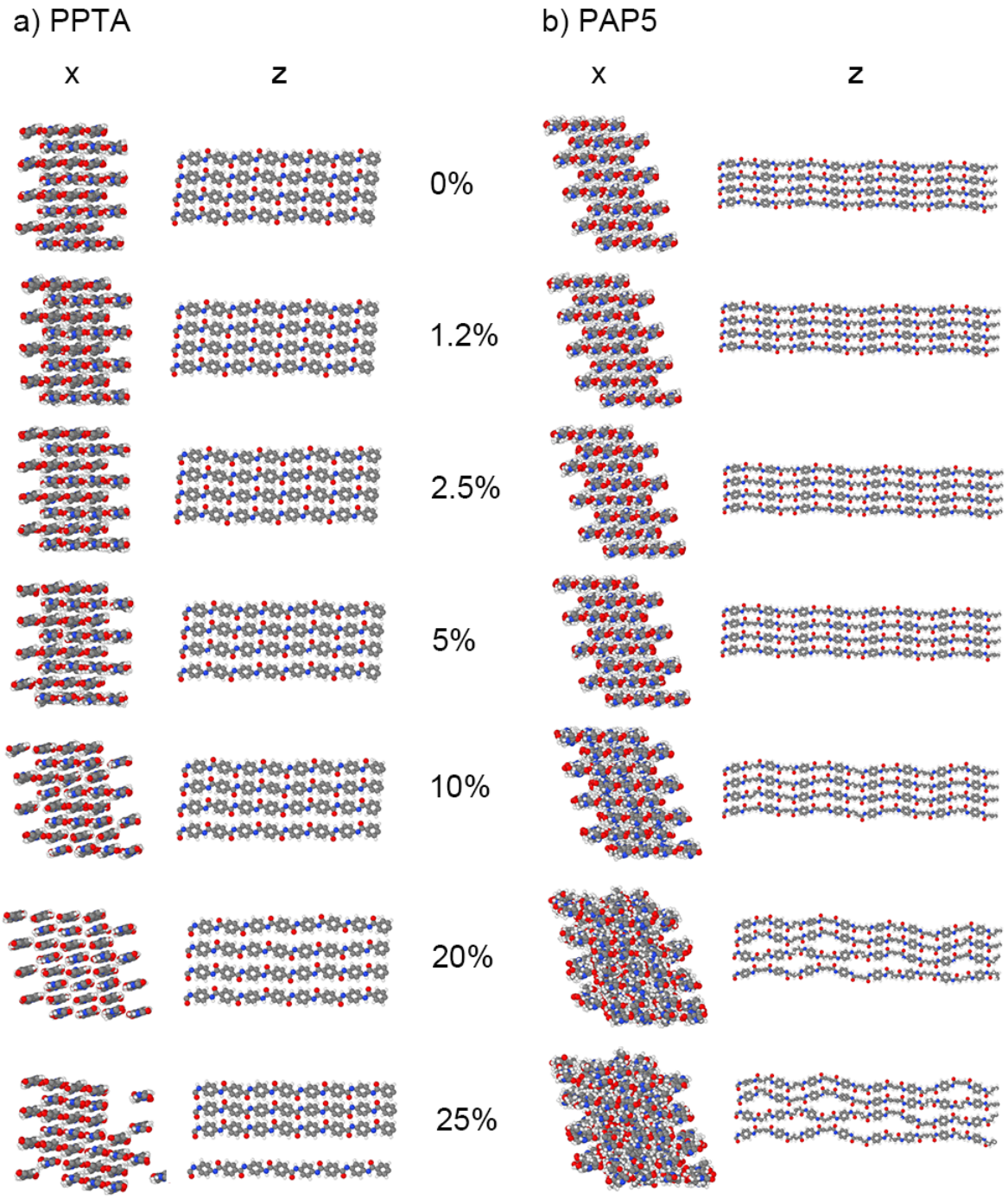

Figure 3.9: Snapshots of (a) PPTA and (b) PAP5 while strained in y-direction with a strain rate of 1×10^{9} s^{-1} at 0, 5, 7.5, 10, 12.5 and 20% strains with the Liu force field as viewed from the x- and z-directions. Snapshots correspond to the solid circles on the stress-strain plots in Fig. 3.8.

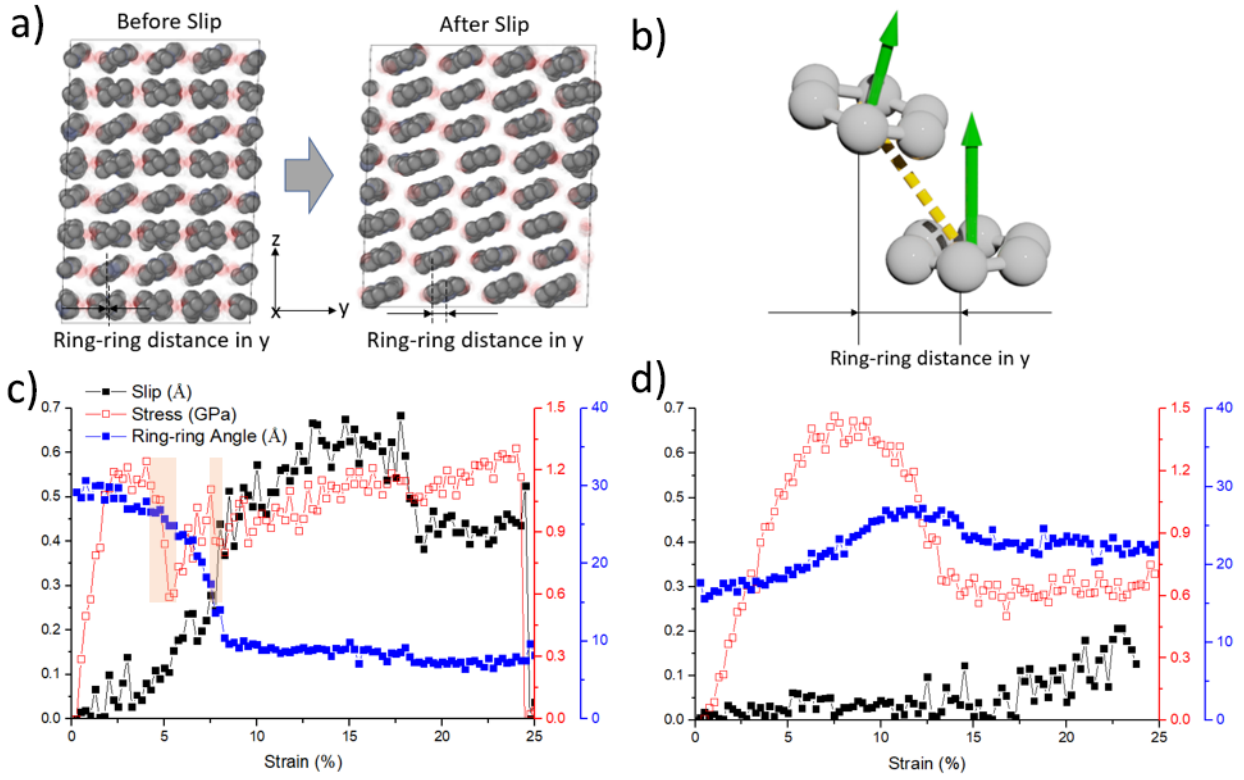

Figure 3.10: (a) Example snapshots of ring-ring distance before and after slip in the y-direction, (b) ring-ring angle as a quantification of coplanarity of aromatic rings. Slip quantified by ring-ring distance in y-direction, stress, and coplanarity quantified by ring-ring angle as functions of strain in the y-direction for (c) PPTA and (d) PAP5. The slip is quantified as the average distance between each pair of adjacent aromatic rings from two adjacent sheets at each strain with reference to the zero strain. For PPTA, after slip and yield, the chains become more ordered as evidenced by the decrease in ring-ring angle (becoming more coplanar). The structural optimization of PPTA by slip allows subsequent strain hardening. Due to the accommodation of strain by slip, the yield stress of PPTA is lower than that of PAP5. In comparison, slip is not observed for PAP5, therefore the H-bonds accommodate all of the strain resulting in a higher yield stress than PPTA.

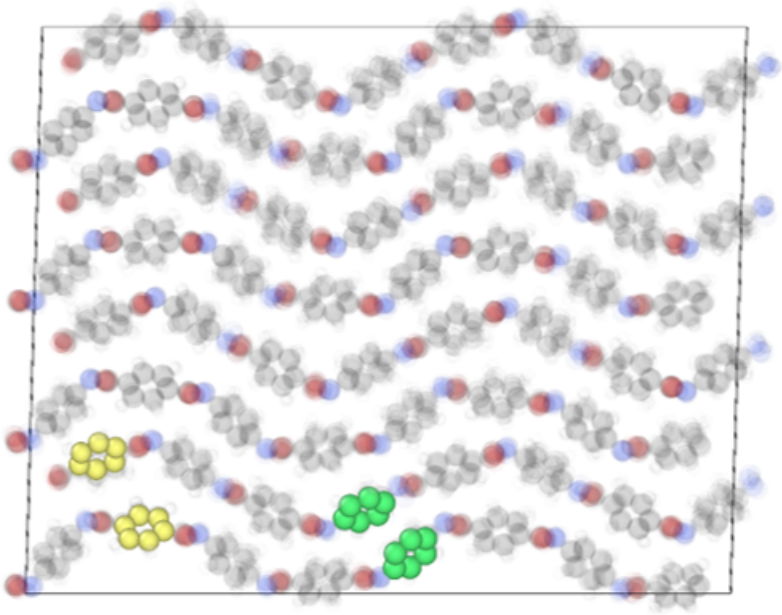

Figure 3.11: Representative snapshot of PPTA strained in the z-direction at 25% strain. Two ring pairs located near peaks (yellow) and between peaks (green) of the buckled chains. The distance between rings at adjacent peaks or valleys of the buckled chains is larger than the equilibrium value, whereas pairs of rings between peaks or valleys have smaller distance than at equilibrium.

25% strain. This is because the buckling in PPTA accommodates some of the strain. In the π-stacking RDFs of PPTA (Figs. 3.13g-h), the average distance decreases with strain but the width of the peak dramatically increases, corresponding to the loss of π-π registry due to strain-induced buckling (Fig. 3.14a). This loss of π-π registry and lower coplanarity weakens the π-stacking interactions, which results in the smaller ultimate stress of PPTA (0.72 GPa) than that of PAP5 (0.99 GPa).

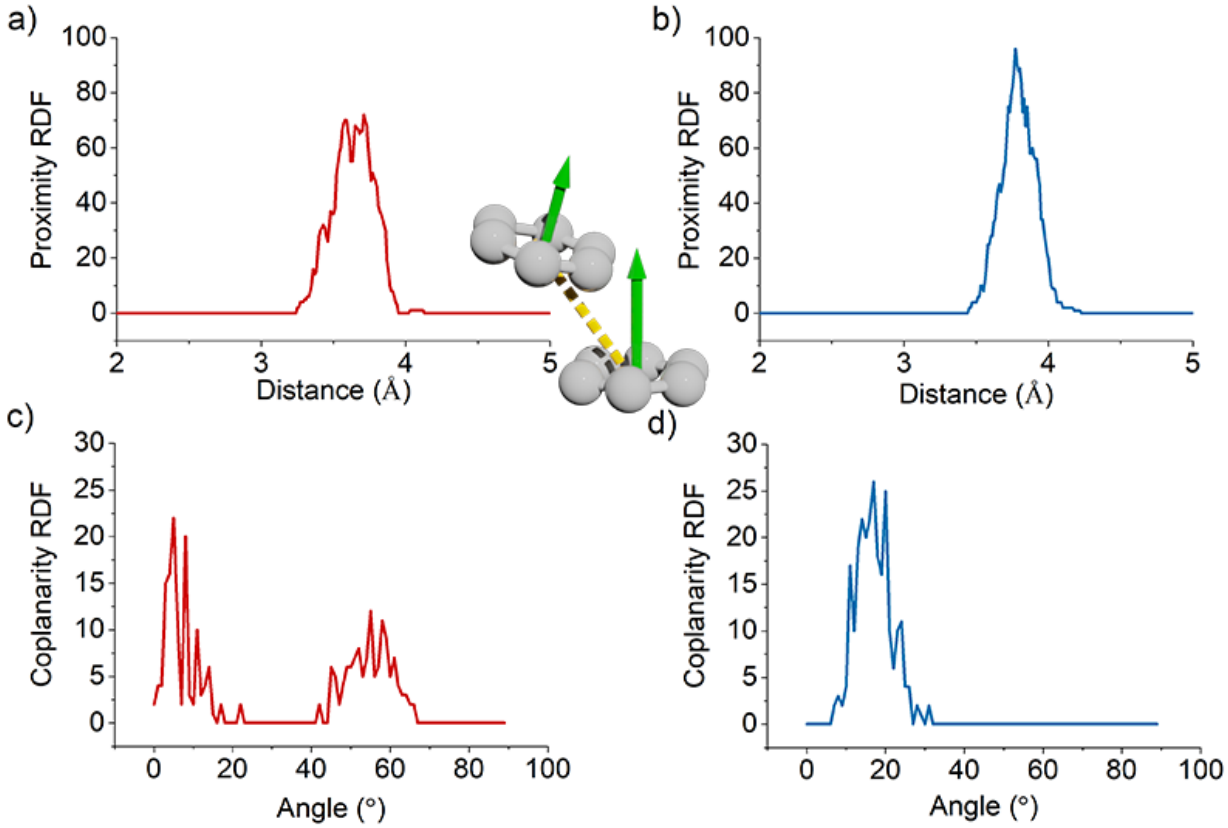

Figure 3.12: RDFs of proximity (a and b) and coplanarity (c and d) of aromatic rings for PPTA (a and c) and PAP5 (b and d). The proximity RDFs are calculated from the distance between every pair of adjacent rings (yellow dotted line in the schematic), and the coplanarity RDFs are calculated from the dihedral angle between every pair of adjacent rings (the angle between the green arrows in the schematic). Smaller proximity and coplanarity are indicators of stronger π-stacking interactions. The results indicate that the ring-ring proximity of PPTA and PAP5 are similar, but PAP5 is more coplanar than PPTA.

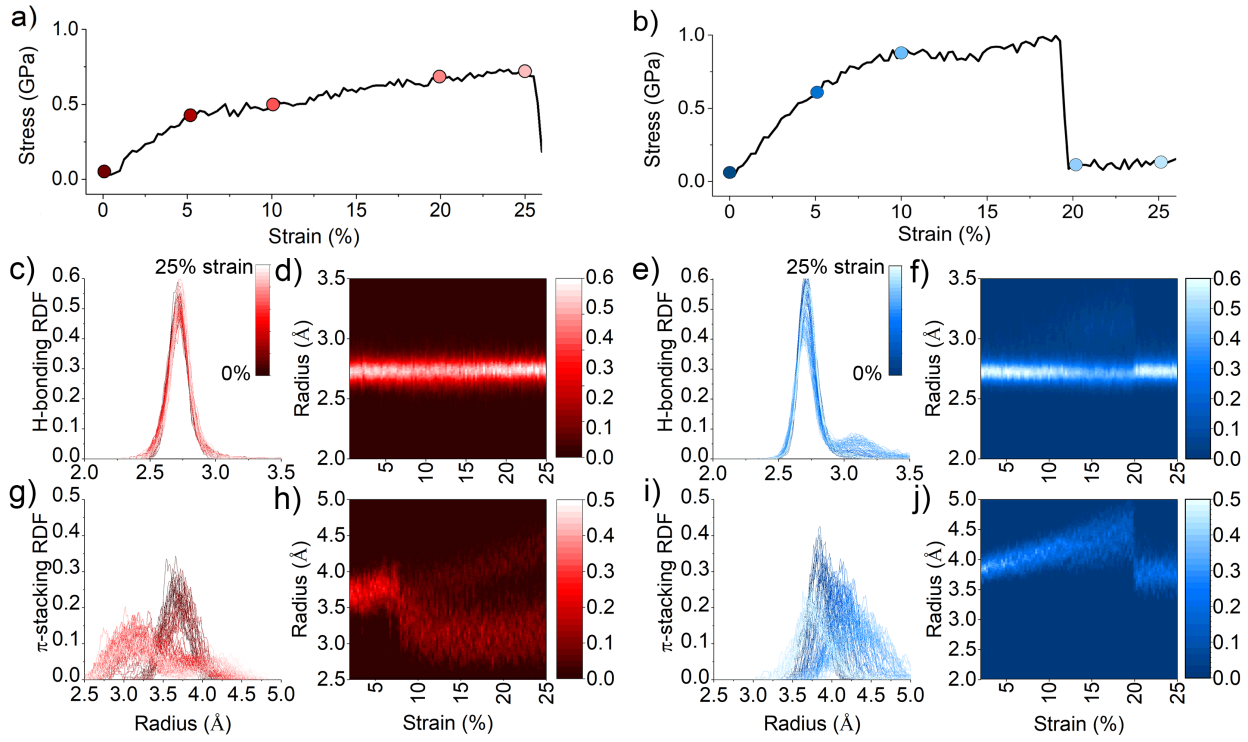

Figure 3.13: Stress-strain behavior (a and b) and RDF profiles and heat maps for H-bonding (c, d, e, and f) and π-stacking (g, h, i, and j) for PPTA (a, c, d, g, and h) and PAP5 (b, e, f, i, and j) strained in the z-direction with Liu force field. The RDFs are normalized by the number of bonds per unit cell. Movies S3 and S6 showing the evolution of the stress and RDF distributions as well as the time evolution of the models are available in the Supplemental Information.

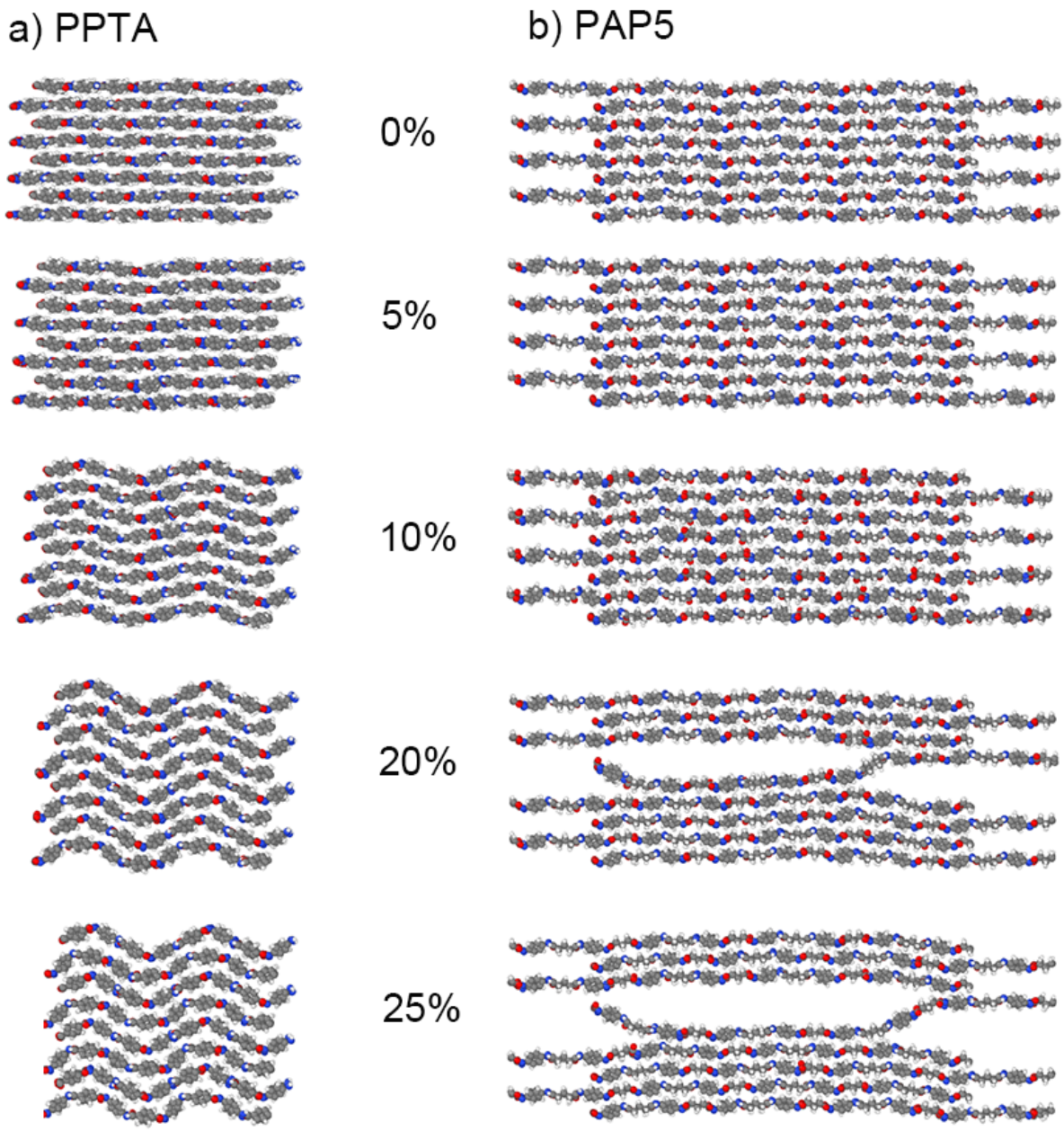

Figure 3.14: Snapshots of (a) PPTA and (b) PAP5 while strained in z-direction with a strain rate of 1×10^{9} s^{-1} at 0, 5, 7.5, 10, 12.5 and 20% strains with the Liu force field as viewed from the y-direction. Snapshots correspond to the solid circles on the stress-strain plots in Fig. 3.13.

3.4 Conclusions

The optimum force field developed by Liu et al. as identified in Chapter 2 was used to simulate stress-strain behavior in the chain and transverse-to-chain directions for aromatic polyamide PPTA and a related aromatic-aliphatic polyamide PAP5. The mechanical properties of the two polymer crystals were calculated, compared to each other and, for PPTA, compared qualitatively to previously reported experimental data. Anisotropy was observed in the stress-strain response of PPTA and PAP5 in the chain and transverse directions.

For strain in the chain-direction, it was found that the ultimate stress and failure strain of PAP5 were larger than those of PPTA, but the low-strain elastic modulus of PAP5 was smaller. These trends were investigated in terms of the waviness at different strains, as well as intramolecular amide and H-bond densities. One key difference between PPTA and PAP5 was found to be the initial (zero strain) conformation which was extended for PPTA and wavy for PAP5. The loose conformation of PAP5 gave it an additional degree of freedom that could accommodate low strain (up to about 4%) without stretching covalent bonds within the chains. This resulted in a smaller stiffness at low strains and a larger failure strain for PAP5 than PPTA. However, different mechanisms explained the high strain behavior leading to a larger high-strain stiffness and ultimate stress for PAP5 than PPTA. This difference was attributed to better alignment of PAP5 chains in the strained conformation.

Simulations of strain in the transverse directions demonstrated significant anisotropy of the mechanical properties, reflecting the anisotropic material structure. In both of the transverse directions, where intermolecular interactions (H-bonding and π-stacking) were dominant, the stiffness and ultimate stress of the crystals were much lower than those in the chain direction which were determined primarily by intramolecular interactions.

The y-direction strain response was dominated by H-bonding between adjacent chains. The stronger H-bonding of PPTA resulted in higher stiffness and larger ultimate strength than PAP5. Both crystals exhibited yield in response to strain in the y-direction. However, yielding of PPTA was due to inter-sheet slip and the yield strength was lower than that of PAP5 where yielding was associated with breaking of H-bond interactions.

Strain in the z-direction was accommodated by π-stacking interactions. In this direction, PPTA had lower stiffness and ultimate stress than PAP5. This was explained by the coplanarity of the rings in PAP5 which resulted in stronger π-π interactions, as well as buckling of the PPTA chains in response to strain in the z-direction.

Further, the comparison of PPTA to PAP5 reported here highlighted how small changes in the polymer structure, in this case substituting an aromatic linker for an aliphatic linker, can have dramatic effects on mechanical properties. Understanding the atomistic mechanisms underlying stress-strain behavior can enable identification of polymers with desired and potentially tunable properties for a variety of emerging applications.

Chapter 4

Effect of Aliphatic Chain Length on the Stress-Strain Response of Polyamides

4.1 Introduction

As can be seen from Chapter 3, even minor changes in the molecular structure of the aromatic-aliphatic polyamides might significantly affect the mechanical behavior. For example, longer spacer lengths for a given aromatic amide system leads to a reduction in H-bonds density which will lower the melting temperature.[120] However, experimentally studying this relationship for polyamide crystals is difficult and time-consuming, and requires sensitive equipment. [38, 142, 162] Obtaining large single crystal materials is challenging (slow evaporation of solvent is used to get large single crystals for modulus measurements [9, 122, 197]), and the morphology of the polymers is complicated due to the presence of amorphous contributions (e.g., non-crystalline regions and defects). In addition, it is difficult with experimental techniques to distinguish the relative contributions of intramolecular (e.g., covalent bonds) interactions and intermolecular interactions (e.g., H-bonding and π-stacking) to bulk mechanical properties. [173].

To overcome these limitations, experimental methods have been complemented by MD simulations to study materials at the atomistic scale. [162] MD simulations can help interpret experimental results, guide the development of new experimental methods, and provide useful information about both the dynamic and static properties of molecular systems. [117, 211, 216] MD simulations have been successfully applied to study aromatic-aliphatic polyamide crystals, including the role of aliphatic and aromatic groups on intermolecular interactions, free volume, and glass transition temperature [27, 104], the origin of melting, [46] and the influence of methylene segments on crystal packing and chain conformation. [46] Understanding the relationship between chemical structure and the emergent physical properties will enable chemists to synthesize polymers with desired thermo-mechanical properties. However, MD simulations have not been used to understand the effect of the length of flexible aliphatic moieties on the mechanical properties of semi-aromatic polyamide crystals. In Chapter 2, we

compared PPTA with one PPTA-related aromatic-aliphatic polyamide, PAP5, where 5 refers to the number of carbon atoms in the diacid monomer used in the reaction with *p*-phenylene diamine. The results showed that some mechanical properties (tensile strength and failure strain) of PAP5 were superior to those of PPTA.

Here, we extended our study in Chapter 3 by modeling PPTA and a homologous set of PPTA-related aromatic-aliphatic polyamides—PAP5, PAP6, PAP7, and PAP8—with 5, 6, 7 or 8 carbon atoms in the diacid monomer. The goal was to characterize the effect of aliphatic chain length on mechanical properties and then correlate differences between polymers to intra- and inter-molecular interactions. Reactive MD simulations showed that the polymer crystals had lower stiffness in the chain direction at low strain than high strain, and the length of the aliphatic segment affected both the low-strain elastic modulus and ultimate stress. The difference between low- and high-strain behavior was attributed to the configurations of the chains in the quiescent state and the aliphatic chain length effect was found to be caused by both intra- and intra-chain processes.

4.2 Methods

Similar to the methods used in Chapter 3, the polymer crystal models of PAP6-PAP8 were initially constructed using Materials Studio [12]. Unit cell dimensions were initialized based on the models for PPTA and PAP5. The crystal structures of PAP6 (which is reported in Ref. [46]) and PAP7 and PAP8 (for which there is no experimental data) were initialized based on the lattice parameters of PAP5 by extending the aliphatic chain length and the unit cell in the chain direction (c-axis) correspondingly. This approach reproduces the salient intra- and intermolecular features of the structures elucidated in Ref. [46]. All five polyamide crystals exhibit two-dimensional, alternately sheared H-bonded sheets (α form) with the carbonyls on each diacid oriented in the same direction for the odd polymers (PAP5 and PAP7) and in opposite directions for the even polymers (PAP6 and PAP8). Moreover, the c-axis dimensions of PPTA, PAP5, and PAP6 agree quantitatively (within 1 Å) and comprise the same number of repeats, indicating that the chain conformation, particularly those of the aliphatic segments, are consistent with the literature. There are some differences in the positions of the aromatic rings. Ref. [46] reports an alternating twist of the phenyl rings and a translation along the c-axis (pseudomonoclinic), which our model does not include. Nevertheless, both models exhibit π-π registry between neighboring chains. Having no experimental basis for initializing the crystal structures of PAP7 and PAP8, we elect to preserve the aforementioned features by using the same scheme for all four semiaromatic polyamides.

The lattice parameters of the initial unit cells are given in Table 4.1. The chemical formulas and atomic-scale models of the PPTA and PAP5-PAP8 unit cells are shown in Fig. 4.1. The chain direction was aligned with the x-axis (corresponding to crystallographic axis *c*), and the H-bonding and π-stacking directions were aligned with the y- and z-axes, respectively. The unit cell was then replicated in the x-, y- and z-directions to create larger simulation boxes (4×4×4) to maintain MD simulation fidelity while maximizing the computational efficiency,

as demonstrated in Chapter 2. Periodic boundary conditions were applied in all three directions to mimic ideal crystalline polymers with infinite chain length and without defects or chain ends. Although the models in this study are approximations of realistic crystalline polymers that have finite length chains with defects and chain ends, the results here represent upper bounds on the mechanical properties and the simulation methods developed form the basis for more realistic models.

In Chapter 2, two non-reactive force fields OPLS [50] and CVFF [42] and seven different ReaxFF parameterizations were tested for PPTA and PAP5. The results indicated that the ReaxFF force field developed by Liu [102] was best for studying structure-property relationships of PPTA and PAP5. Since the structure of PAP6, PAP7, and PAP8 are similar to PPTA and PAP5, we still used the same ReaxFF Liu force field for the simulations here.

All the MD simulations were carried out using the open-source MD simulation package LAMMPS. [141] OVITO [166] was used for model visualization. The MD time step was 0.25 fs for all simulations. Temperature and pressure were controlled using a Nosé-Hoover thermostat [79] and barostat [80] with damping parameters of 25 fs and 250 fs, respectively. Energy minimization was performed after the unit cells were replicated. Then, each polymer crystal was equilibrated by running simulations in the NPT (constant number of atoms, pressure, and temperature) ensemble for 125 ps (until the lattice parameters reached steady state) at 300 K and 1 atm. The unit cell lattice parameters of the equilibrated polymers are shown in Table 4.2. The magnitude of the unit cell dimensions, a, b, and c, each changed by about 2% on average after NPT equilibration. The largest single change was a 4.5% decrease in the a dimension of PAP5. The unit cells remain nearly monoclinic but take on some triclinic character. The lattice angles α and β each change by about 4% on average remain between 80° and 90°. The largest change in the unit cell parameters is in γ, which decreases by 1% for PPTA and 14% on average for the four aromatic-aliphatic polyamides. In summary, the chain packing in the backbone and H-bonded directions are only modestly changed, while the π-π stacking planes are sheared slightly for an average decrease in unit cell volume of 1% for PPTA and 6% for the aromatic-aliphatic polyamides. Next, the system was stretched in the chain direction (x-direction) with a strain rate of 1×10^{9} s^{-1} until the total strain reached 25% (true strain). The details of the method were reported in our previous paper [203]. The low-strain elastic modulus was calculated by applying a linear fit to the stress-strain data from 0-2% strain, and the high-strain modulus was calculated from the last 5% strain before failure. The ultimate stress was the stress at the failure strain. These simulations were repeated three times independently with different random velocity seeds before the NPT simulation.

Lastly, a separate set of simulations was run to model the stress-strain response of individual polyamide chains. All the chains, except the one in the center of the crystal, were removed from the last trajectory of each 4×4×4 model after equilibration in the NPT ensemble. Then, strain was applied to the single chain in the x-direction using the same approach as described above for the crystals until 25% true strain was reached.

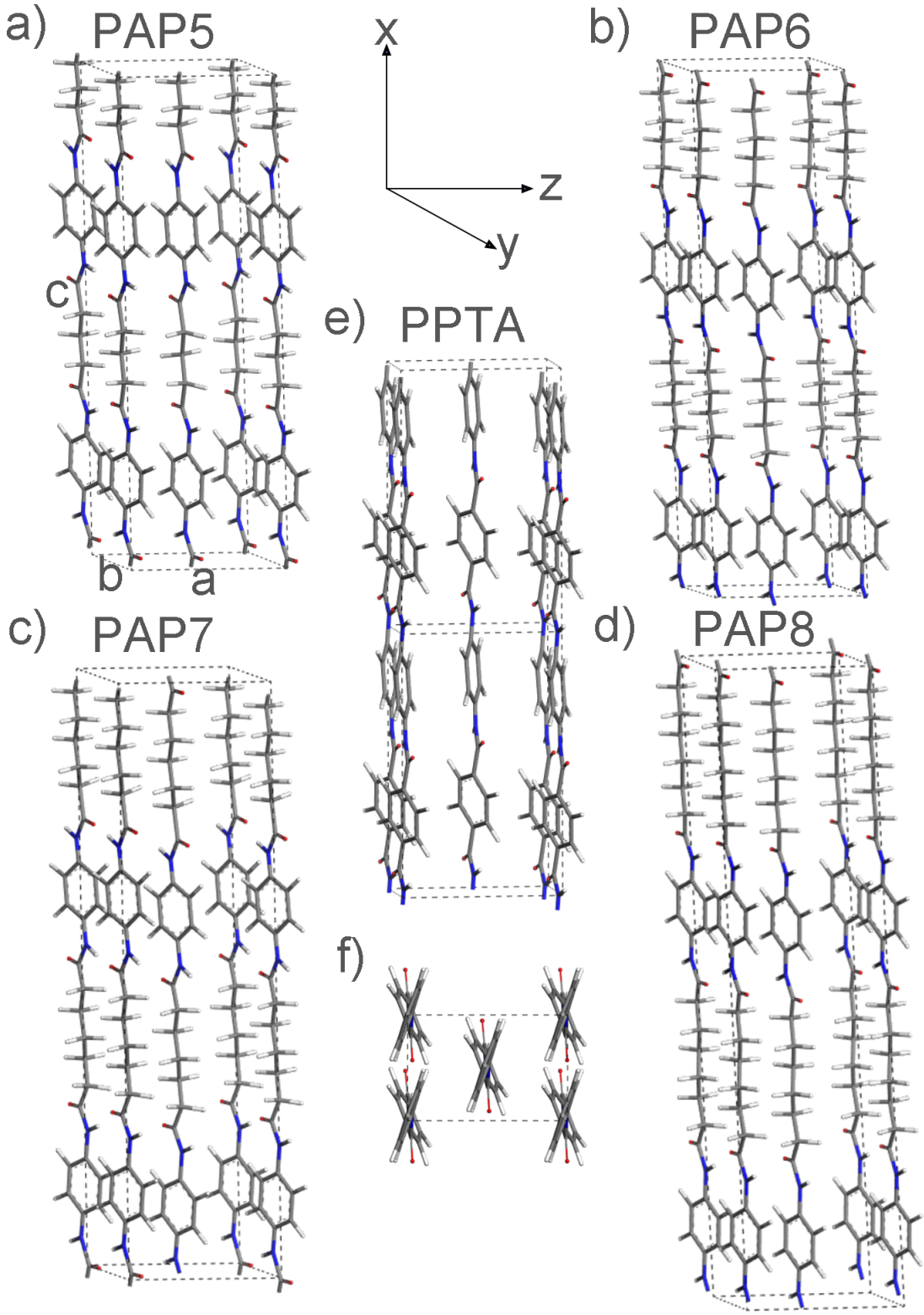

Figure 4.1: Initial unit cells of (a) PAP5, (b) PAP6, (c) PAP7, (d) PAP8, and (e-f) PPTA. The orthogonal directions (x, y, and z) and lattice constants (a, b, and c) are defined with respect to the perspective view of the PPTA. Atom colors correspond to: oxygen, red; nitrogen, blue; carbon, gray; and hydrogen, white.

4.3 Results and Discussion

4.3.1 Lattice Parameters of Polyamides before and after Equilibration

Polymer	a (Å)	b (Å)	c (Å)	α (°)	β (°)	γ (°)
PPTA	7.87	5.18	12.9	90	90	90
PAP5	8.50	4.70	24.8	90	85	90
PAP6	8.50	4.70	27.4	90	85	90
PAP7	8.50	4.70	30.2	90	85	90
PAP8	8.50	4.70	32.8	90	85	90

Table 4.1: Initial unit cell lattice parameters of the polymers. For PPTA and PAP5, the unit cell lattice parameters were set to match those measured from XRD. [46]. The initial PAP6, PAP7, and PAP8 crystals were created based on the lattice parameters of PAP5 by simply extending the aliphatic chain length and the unit cell in the chain direction (lattice constant c) correspondingly.

Polymer	a (Å)	b (Å)	c (Å)	α (°)	β (°)	γ (°)
PPTA	7.66±0.09	5.1±0.2	13.3±0.04	86±2	89±2	89±3
PAP5	8.12±0.01	4.63±0.01	25.39±0.02	89.96±0.07	90.0±0.3	74.2±0.3
PAP6	8.24±0.03	4.78±0.01	27.01±0.03	82.6±0.1	82.4±0.5	75.8±0.4
PAP7	8.41±0.07	4.58±0.02	30.17±0.05	89.8±0.3	89±2	77.6±0.5
PAP8	8.35±0.08	4.67±0.03	32.0±0.2	83±1	88±2	79±1

Table 4.2: Post-NPT unit cell lattice parameters of the polymers. The errors are the standard deviation calculated over three independent repeat simulations.

4.3.2 Explanation of Trend in Low-strain Modulus

The stress response of each aromatic-aliphatic polyamide crystal to strain in the chain-direction is shown in Fig. 4.2a. The moduli of the crystals are shown in Fig. 4.2b. All crystals exhibited strain hardening, transitioning from a low-strain linear regime to a high-strain linear regime. In Fig. 4.2b, the low-strain and high-strain moduli are plotted as functions of the number of non-aromatic carbons in the polymer repeating unit. At high-strain, the modulus is essentially independent of the number of non-aromatic carbon atoms. This result is consistent with the fact that, at high strain, the modulus is mediated by deformation of covalent backbone bonds, and the bond stiffnesses are similar in all five polymers.

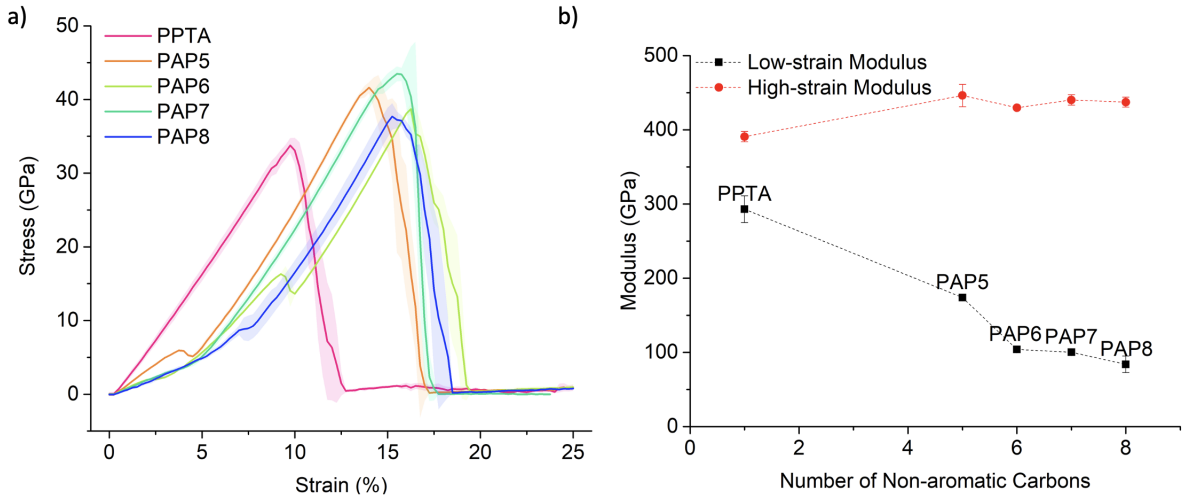

Figure 4.2: (a) Stress-strain curves for 4×4×4 polyamide crystals strained from 0 to 25% strain. The shaded areas reflect standard deviations calculated from three independent simulations. (b) Low-strain and high-strain modulus as functions of the number of non-aromatic carbons in the polymer repeating unit. Low-strain modulus is calculated from the slope of stress-strain curve from 0 to 2% strain. High-strain modulus is calculated from the last 5% strain before failure. Dotted lines are guides to the eye.

In contrast, the low-strain modulus decreases with increasing number of non-aromatic carbon atoms (Fig. 4.2b). In our previous study of PPTA and PAP5, [203] we found that low strain behavior could be correlated with chain waviness (a simple average metric related to the departure from fully extended chain conformations) because wavy chains can accommodate strain without deformation of covalent bonds. Waviness can be quantified from the distribution of the atoms in the polymer in the plane transverse to the chain direction, i.e., the yz plane. Fig. 4.5a is a representative plot of the positions of the non-aromatic backbone atoms in PAP7 with respect to the centroid of each chain, from zero strain to failure. At low strain (darker blue), the atoms are far from the centroid, indicating a wavy structure. Then, as strain increases (lighter blue), the chain is extended, and the atoms are found closer to the centroid. Similar behavior was exhibited by the other polymers (see Fig. 4.3).

Waviness was calculated as the radius of a circle that encompasses 90% of the atomic coordinates closest to the center of the chain such that a larger radius corresponds to atoms further scattered from the centroid and wavier chain. The results for all polymers are shown in Fig. 4.5b, where waviness at 0% strain, R_0, increases with number of non-aromatic carbons. To confirm the use of a radius to approximate distribution size was reasonable even for non-circular atom position distributions, we also calculated the area of an oval fit to the positions of the 90% innermost non-aromatic carbon atoms and nitrogen atoms. Like the radius, the area of the best-fit oval increased with number of non-aromatic carbons (see Fig. 4.4). The

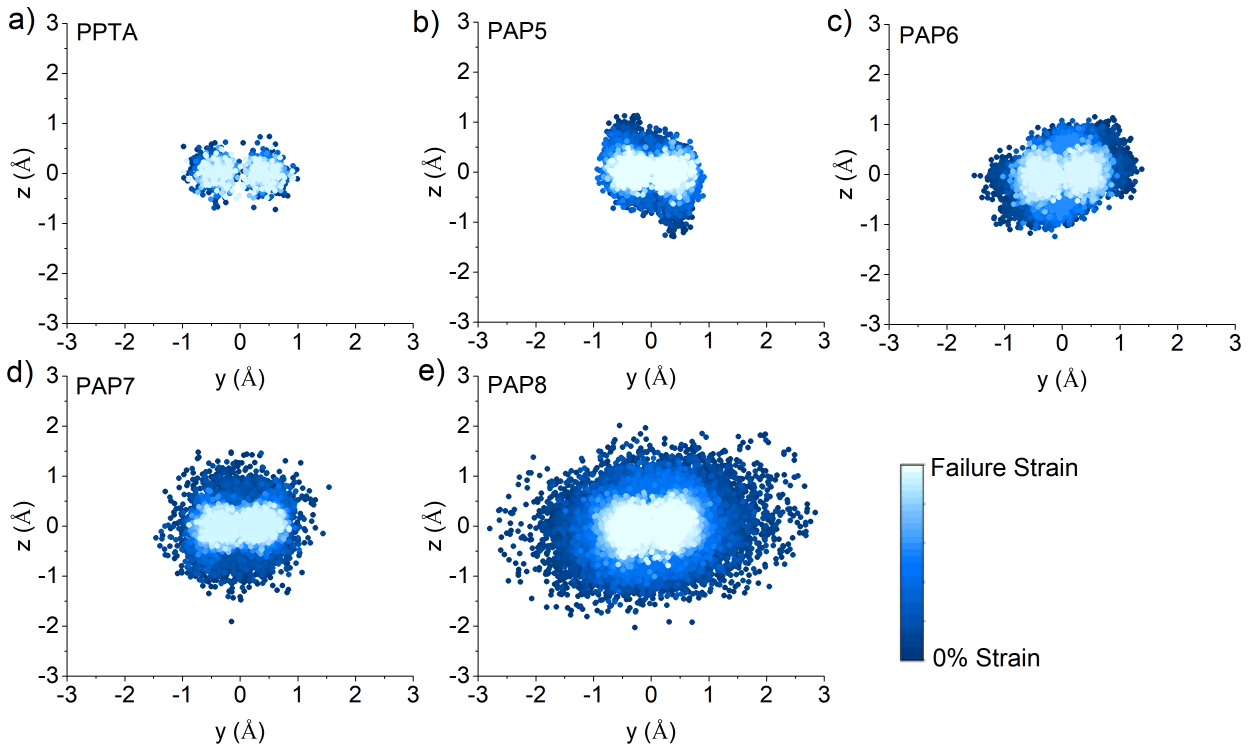

Figure 4.3: Positions of the non-aromatic, backbone atoms in the chains projected on the yz plane, where the centroid of each chain is the origin of the yz plane, for (a) PPTA, (b) PAP5, (c) PAP6, (d) PAP7, and (e) PAP8. Waviness was quantified from the radius of a circle fit to the outline of the 90% innermost non-aromatic carbon atoms and nitrogen atoms.

increasing trend of waviness is due to the methylene groups acting as spacers between the hydrogen-bonded amide groups, which increases the conformational freedom of the polymer chains. [46, 71] The strong negative correlation between the low-strain modulus and waviness is shown in Fig. 4.5b.

To confirm the use of a radius to approximate distribution size was reasonable even for non-circular atom position distributions, we also calculated the area of an oval fit to the positions of the 90% innermost non-aromatic carbon atoms and nitrogen atoms. Like the radius, the area of the best-fit oval increased with number of non-aromatic carbons (see Fig. 4.4).

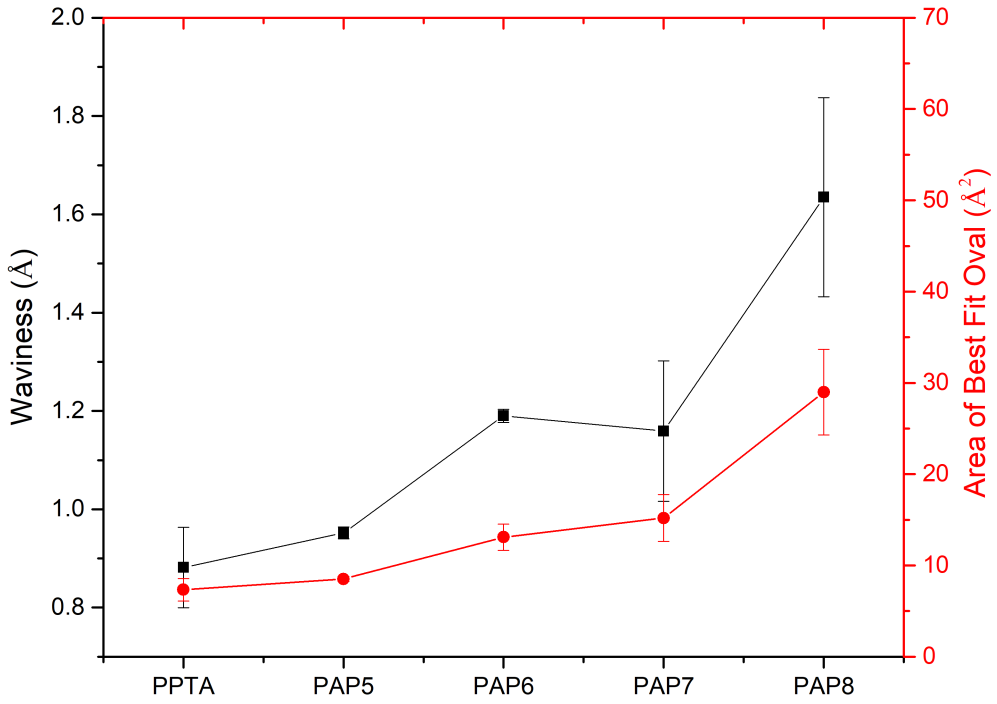

Figure 4.4: Waviness of the polymers calculated as the radius of best fit circle (black) and the cross-sectional area of the chains calculated from of the best fit oval (red) of the atom distribution. In both cases, the calculation is based on the positions of the 90% innermost non-aromatic carbon atoms and nitrogen atoms in the yz plane. The error bars reflect standard deviations calculated from three independent simulations.

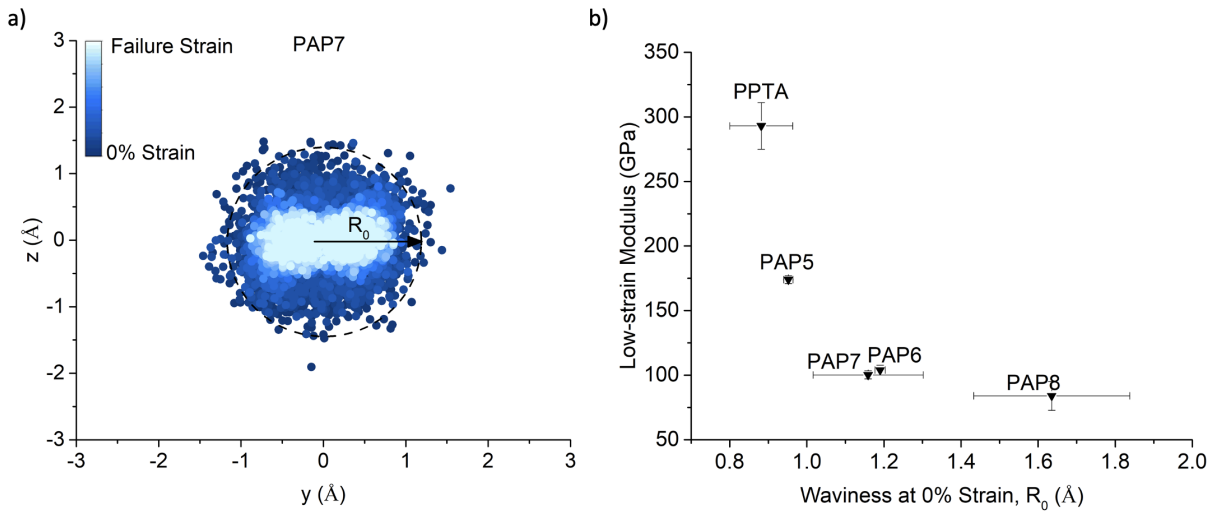

Figure 4.5: (a) Positions of atoms in the chains projected on the yz plane for PAP7 as a function of strain, where the origin corresponds to the centroid of each chain. Similar plots for the other polymers are shown in Fig. 4.3. Waviness is quantified as the radius R_0 of a circle encompassing the coordinates of 90% of the inner-most non-aromatic carbon atoms and nitrogen atoms. (b) Low-strain modulus as a function of the waviness at 0% strain. The error bars reflect the standard deviations calculated from three independent simulations.

4.3.3 Explanation of Trend in High-strain Modulus

4.3.4 Explanation of Trend in the Transition from Low to High Strain

In Fig. 4.2, except for PPTA, all of the polymers exhibit a change in slope between low and high strain in the stress-strain curve. Also, for some polymers, there is a second inflection or shoulder, after the slope change, in the stress-strain curve. To explore the origin of this behavior, stress-strain simulations were performed for single chains taken from the end of the NPT equilibration simulation of each crystal before stretching. Two representative comparisons between crystals and single chains, for PAP6 and PAP7, are shown in Fig. 4.6. Both single chains and crystals exhibit lower stiffness at low strain than at high strain, with the increase in stiffness occurring around 5% strain, indicating that this behavior is due to intra-chain processes. For PAP6 (Fig. 4.6a) and PAP8 (Fig. 4.7e), the second inflection or shoulder after the initial slope change in the stress-strain curve is only observed for the crystals, not the single chains. This indicates that the second transition in the stress-strain response of the even polymers is due to inter-chain effects.

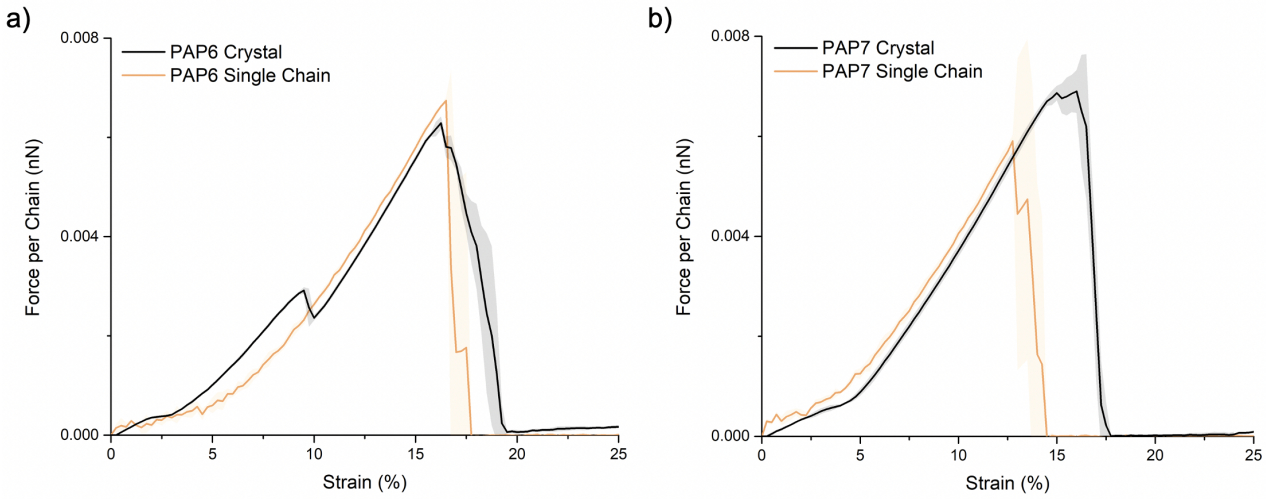

Figure 4.6: Stress-strain response of single chain (orange) and crystal (black) forms of (a) PAP6 and (b) PAP7. The single chain is taken from the end of the NPT equilibration simulation of each crystal before stretching. The force per chain is calculated as the total stress multiplied by the cross-sectional area of the simulation box (orthogonal to the strain direction) and then divided by 32 chains for the crystal and 1 for the single chain. Similar trends for PAP5 and PAP8 are shown in Fig. 4.7. The shaded areas reflect standard deviations calculated from three independent simulations.

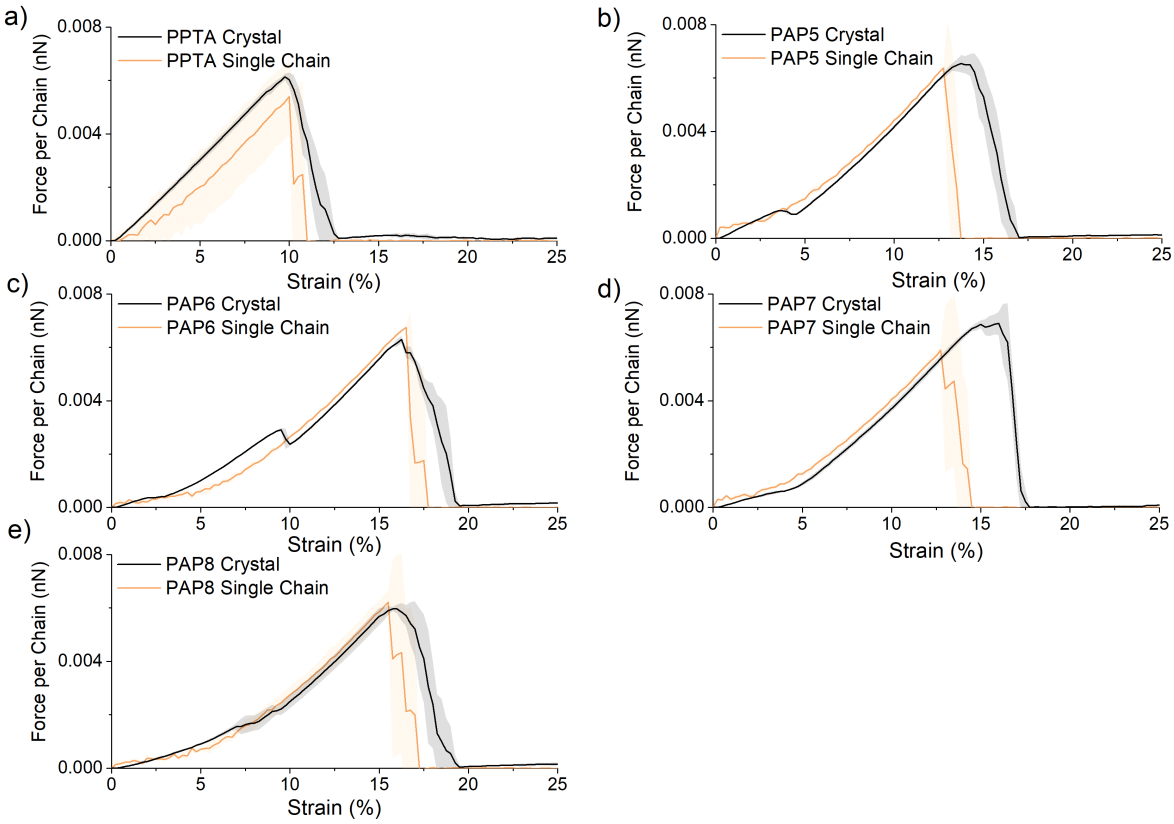

Figure 4.7: Stress-strain response of single chain (orange) and crystal (black) forms of (a) PPTA, (b) PAP5, (c) PAP6, (d) PAP7, and (e) PAP8. The force per chain is calculated as the total stress multiplied by the cross-sectional area of the simulation box (in the strain direction) and then divided by 32 chains for the crystal and 1 for the single chain. The shaded areas reflect standard deviations calculated from three independent simulations.

To understand how inter- and intra-chain interactions affect the stress-strain response of the crystals, the movement of the atoms and aromatic rings was characterized in terms of rotation of dihedral angles and inter-chain slip. First, dihedral rotation was quantified as the dihedral angles (HNCO, NCCC, and OCCC) in the backbones of the chains. The change of the dihedral angles during stretching relative to the equilibrated state at zero strain is plotted as a function of strain in Fig. 4.10. For PAP5-PAP8, the NCCC dihedral angles increase and the OCCC angles decrease gradually in the low-strain regime as the energy barriers for bond rotations are overcome. [177] The gradual increase in stiffness at low-strain exhibited by all polymers, except PPTA, correlates well with changes in the dihedral angles, indicating that small strains are accommodated by straightening wavy chains, i.e., backbone bond rotation. Then, the dihedral angles abruptly increase to near 180° or decrease to near 0° , corresponding

to full extension of the chains, and remain constant until failure. The strain at which these rotational modes are exhausted corresponds closely with the transition out of the low-strain regime for all four aromatic-aliphatic polyamides. In contrast, PPTA adopts the lowest energy fully extended (all-trans) conformation at zero strain, and thus does not undergo conformational rearrangements under tensile deformation.

The predominant inter-chain mechanism observed in the simulations is slip between the chains within each hydrogen-bonded sheet. Inter-chain slip was quantified by the change of average distance (relative to the zero strain distance) in the x-direction between the centers of mass of each pair of adjacent aromatic rings stacked in the z-direction. For PPTA (Movies S7 and S8), PAP5 (Movies S9 and S10), and PAP7 (Movies S13 and S14), the slip remains at zero until failure. However, for PAP6 (Movies S11 and S12) and PAP8 (Movies S15 and S16), the chains undergo a discrete slipping event (the magnitude of which is ~0.5 Å) at the strain corresponding to the second inflection point in the stress data. After this slip event, the relative positions of the chains remain stable until failure.

4.3.5 Origin of Odd-even Effect in Stress-strain Response

The key morphological difference between the even and odd polyamides is the geometry of the H-bonding. The even polymers exhibit a parallelogram H-bonding structure that is less stable than the trapezoid structure of polymers with an odd number of carbon atoms [14, 174, 194]; see Fig. 4.8 for representative snapshots of these structures. This so-called odd-even effect [6, 174] has been observed in the elastic properties of polymers including α,ω-alkanedicarboxylic acids [114] and polyesters [56, 158]. The greater stability of the odd polymers manifests in the strain dependence of the crystal unit cell lattice parameter in the H-bonding direction, b (see Fig. 4.1a for lattice parameter assignments). As shown in Fig. 4.12a, tension in the chain direction caused compression of the lattice in the H-bonding direction for all polymers, corresponding to a gradual decrease of b with strain. This decrease continued for the odd polymers until failure. However, for the even polymers, the lattice constant b abruptly increased at the strain at which inter-chain slip was observed, and then decreased again until failure. The abrupt change of lattice constant b with strain for PAP6 and PAP8 is consistent with the H-bonding trends. A comparison between the average H-bond length and π-π slip in Fig. 4.9 shows that the H-bond length change occurs immediately before the π-π slip for PAP6 and PAP8. This indicates that the π-π slip is driven by an abrupt change in the configuration of the H-bonded sheets.

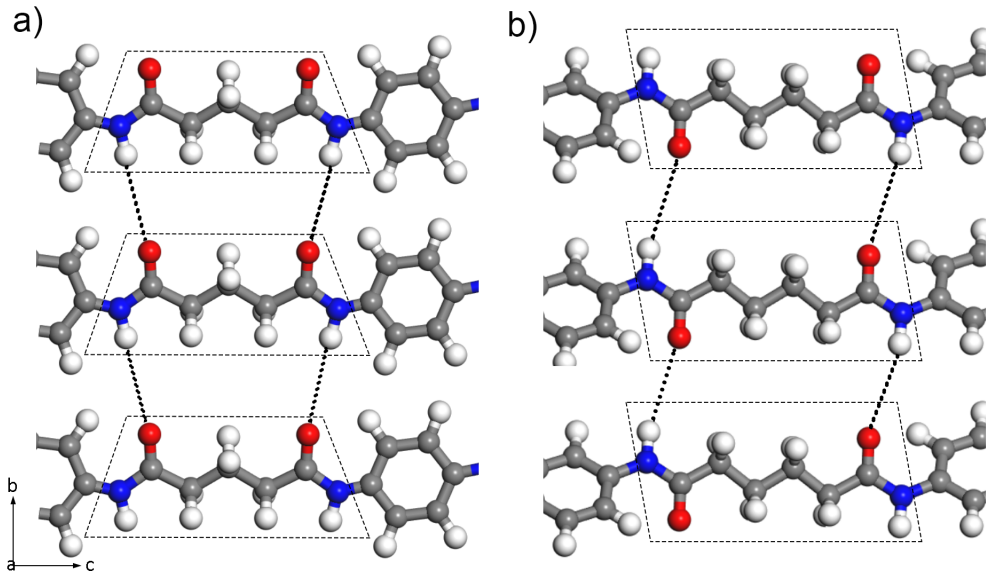

Figure 4.8: Representative snapshots of trapezoid and parallelogram structures in the backbones of (a) odd (PAP5) and (b) even (PAP6) polymers and corresponding H-bonds.

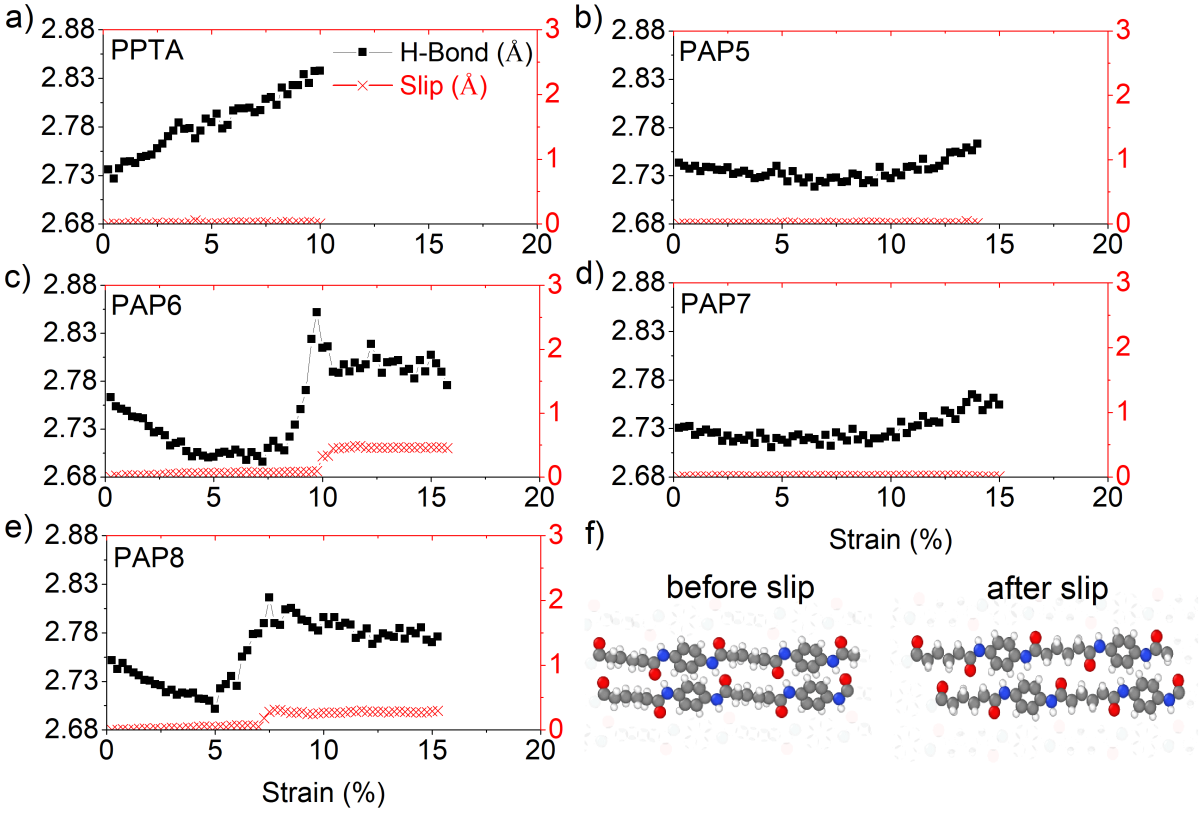

Figure 4.9: Average H-bond length (N-O distance) and inter-chain slip during stretching of (a) PPTA, (b) PAP5, (c) PAP6, (d) PAP7, and (e) PAP8. Data is shown only until failure for each crystal. H-bond length is quantified as the average length of all H-bonds at each strain. Slip is quantified as the change in neighboring ring-ring distance during stretching with respect to 0% strain. Snapshots in (f) show a portion of PAP6 before and after slip occurs.

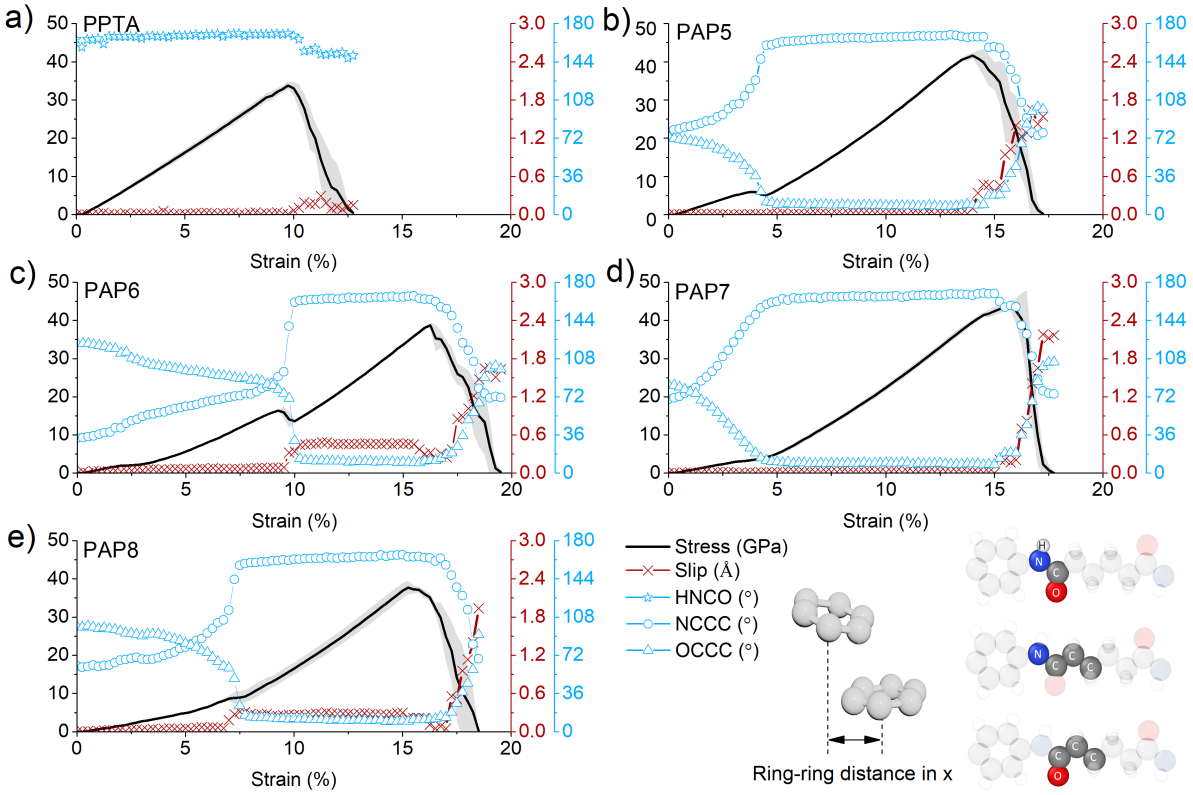

Figure 4.10: Stress, inter-chain slip, and dihedral angles as functions of strain of (a) PPTA, (b) PAP5, (c) PAP6, (d) PAP7, and (e) PAP8. Two of the carbons in the NCCC and OCCC dihedrals are aliphatic and one is the amide carbonyl. Data is shown only until failure for each crystal. Illustrations of the ring-ring distance and the dihedral angles are shown in the lower right corner of the figure. The HNCO dihedral angle distributions are similar for the different polymers (158 ± 7°) at low strains. This angle increases slightly with increasing strain before failure, but the change is very small compared to that exhibited by the other dihedral angles (see Fig. 4.7).

4.3.6 Explanation of Trend in Ultimate Stress

Odd-even effects have also been observed in ultimate properties [144, 158]. As shown in Fig. 4.12b, aromatic-aliphatic polyamides with an even number of carbon atoms have lower ultimate stresses. In all cases the reactive simulations predict that failure occurs by breaking the N-C(O) bond in the amide. DFT calculations were used to probe the bond dissociation energies (BDEs) of the N-C(O) in single repeat units of PPTA and a representative fragment of an aromatic-aliphatic polyamide (Fig. 4.11).

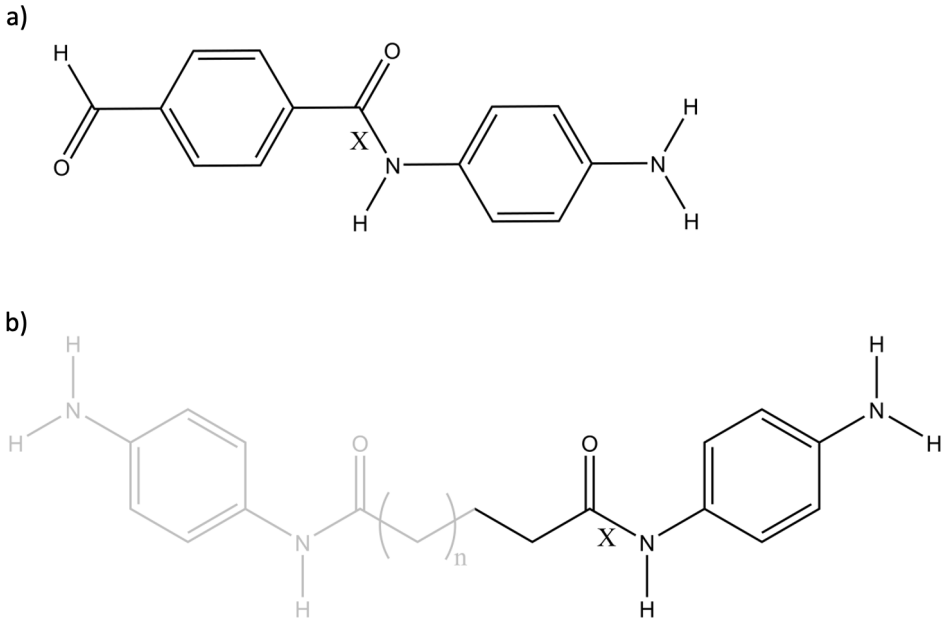

Figure 4.11: Truncated polymer models used to compute the BDE for (a) PPTA and (b) representative aromatic-aliphatic polyamide fragment. X denotes the bond for which the BDE was computed. The gray part of the latter repeat unit was omitted from the DFT calculations because the cleaved bond is not likely to be affected by more distant moieties.

Fig. 4.11 shows the model systems used to compute the lowest BDE of the polymer chains for PPTA and the aromatic-aliphatic polyamides (PAP5 to PAP8). The bond denoted X was selected based on previous work that showed this bond was the weakest in the PPTA system [112], which is also consistent with the current work. To determine the BDE, the bond X was homolytically cleaved leaving two fragments each containing an unpaired electron (doublets). The BDE is then computed from the difference in enthalpy between the whole molecule and the sum of the fragments. These calculations were performed in Gaussian 09 [58] at the M062X/6-311+G(2d,p) level of theory [110, 215].

The computed BDE of bond X was 69.1 kcal/mol for PPTA and 69.3 kcal/mol for the aromatic-

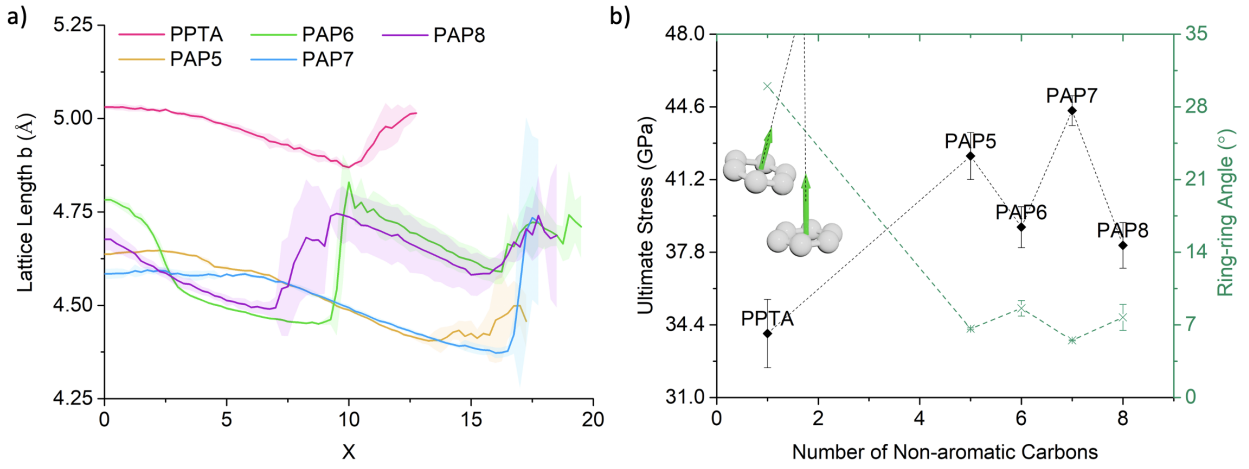

Figure 4.12: (a) Lattice constant in the H-bonding direction, b, for the polymer crystals as a function of strain in the x-direction (chain direction). Data is shown only until failure for each crystal. The shaded areas and errors bars reflect standard deviations from three independent simulations. (b) Ultimate stress and ring-ring angle (averaged over the last 2% before the stress drop for each polymer) as functions of the number of non-aromatic carbons in the polymer repeating unit. The inset schematic defines ring-ring angle.

aliphatic fragment. The 0.2 kcal/mol difference between these two results is within the expected uncertainty of this method, which indicates their BDE is probably equivalent. This calculation was not repeated for longer aliphatic sequences because the longer aliphatic linker in these polymers is not likely to affect the BDE of the amide bond X.

The DFT results showed that the aliphatic segment does not affect bond strength, suggesting the observed odd-even trend in ultimate stress is an inter-chain effect.

Fig. 4.6 and Fig. 4.9 clearly implicate intermolecular interactions for the enhanced strength of the odd polymers. The odd polymer crystals exhibit higher strains and stresses per chain at failure than their single-chain counterparts; on the contrary, the failure properties of the crystals and single chains of the even polymers are indistinguishable. The less stable H-bond structure of the even polymers is one contributing factor. In Fig. 4.12a, prior to failure, the lattice constants b of even polymers are larger than those of the odd polymers, implying that the H-bonds are correspondingly weaker and thus H-bonding contributes less to resisting failure in the even polymers.

It has also been shown that ring-ring interactions (π-stacking) affect the ultimate properties of polyamides, and the strength of these interactions is related to the coplanarity of the rings. [21, 203] The coplanarity of the rings is quantified here by the angle between each pair of aromatic rings in adjacent chains (see inset to Fig. 4.12b) averaged over the last 2% strain before failure. Coplanarity is plotted as a function of the number of non-aromatic carbons in the polymer repeating unit in Fig. 4.12b, where small ring-ring angles correspond to better

registry between the aromatic rings (high coplanarity). The ultimate stress and coplanarity of the polymers exhibit consistent trends where polymers with poorer registry (weaker π-π interactions) have lower strength. The less stable inter-chain interactions of the even polymers is also seen in Fig. 4.7 where the force per chain and failure strain are significantly higher in crystals vs. single chains for odd polymers (PAP5 and PAP7), but there is no statistical difference for even polymers (PAP6 and PAP8).

4.3.7 Strain Rate Dependence of Stress-strain

Finally, it is important to note that the stresses in the simulations are higher than those achievable in experiments. [28, 38, 49, 99, 147]. This is because our model systems have aligned infinite chains (single crystal) without defects (e.g., no chain ends or impurities) or nucleation sites for fracture, which maximizes material strength. In addition, higher order structures that are present in real materials, such as fibrils, amorphous material, as well as chain and/or crystal misorientation, are expected to negatively affect the mechanical properties. Nonetheless, the trends reported here reflect limiting behavior and can be used to understand the effect of the alkyl chain length. Further, the high strain rates of the simulations are necessitated by the inherently short timescale of the simulation method, [103, 159, 175, 218] and have been reported to result in higher predicted strength and modulus. This strain rate-dependence has been attributed to the (in)commensurability between the rate of deformation and the frequency of molecular processes. [162] Although only a limited strain rate range could be tested in the simulations due to the short timescale inherent to reactive force fields, we performed stress-strain simulations for the crystals at two additional strain rates, 1×10^{8} s^{-1} and 1×10^{10} s^{-1}. As shown in Fig. 4.13, the transitions from low- to high-strain regimes shifted to higher stresses with increasing strain rate, which is qualitatively consistent with the effect of strain rate on the yield point of semicrystalline [100] and amorphous polymers.[18, 76] However, the trends exhibited by calculated mechanical properties, shown in Fig. 4.14, were similar at the three strain rates. Specifically, at all strain rates tested, the low-strain modulus decreased with increasing number of non-aromatic carbons, the high-strain moduli were insensitive to the number of non-aromatic carbons and were higher than the low-strain moduli, and the ultimate stress exhibited odd-even effect.

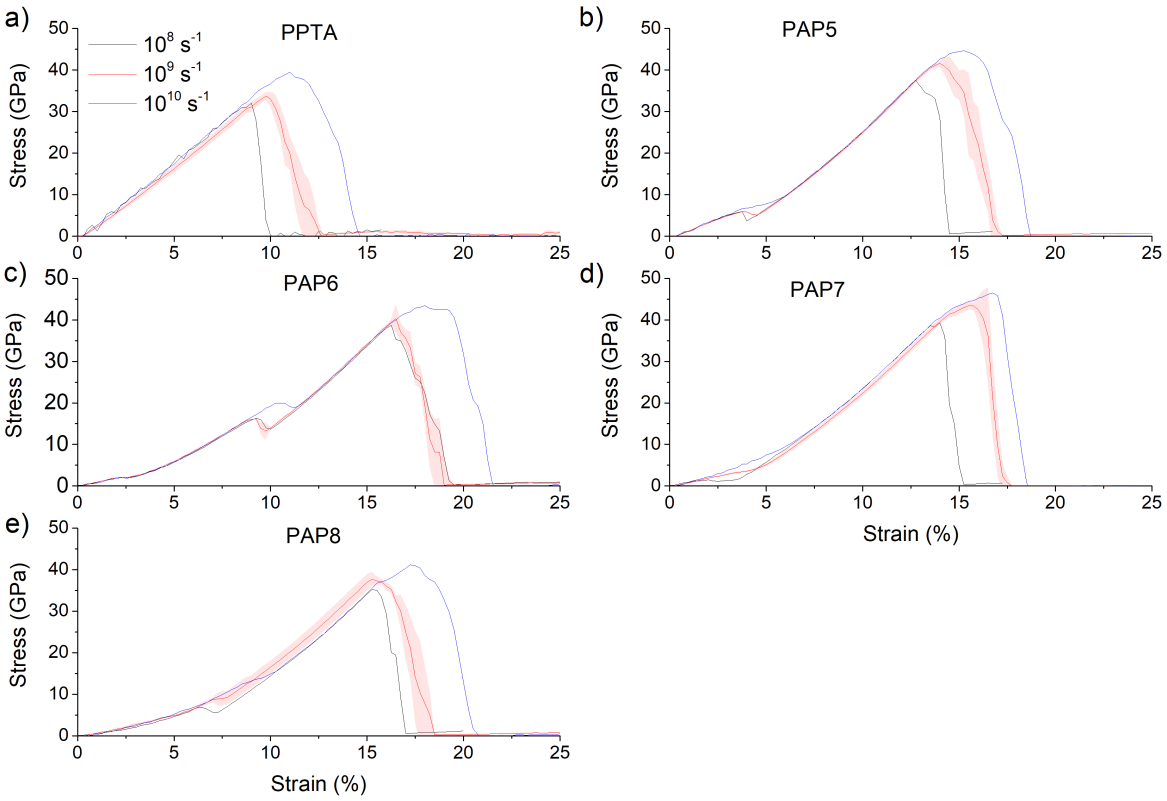

Figure 4.13: Stress-strain curves of (a) PPTA, (b) PAP5, (c) PAP6, (d) PAP7, and (e) PAP8 at three different strain rates: 1×10^8, 1×10^9, and 1×10^{10} s^{-1}. The shaded areas for strain rate 1×10^9 s^{-1} reflect standard deviations calculated from three independent simulations. Similar trends, including the shoulder at the transition between low and high strain behavior, are observed at all strain rates. The shoulder is more distinct at lower strain rates because the model systems have more time for rearrangements resulting in dihedral angle changes and inter-chain slip.

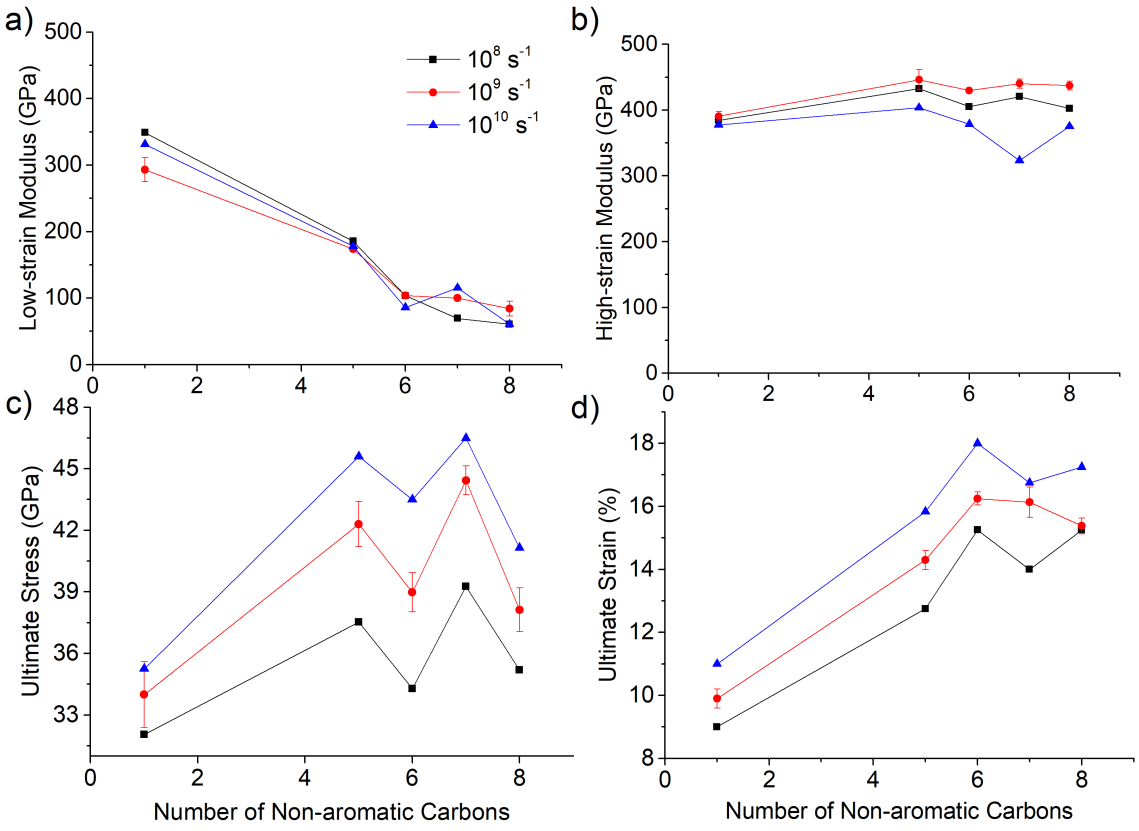

Figure 4.14: (a) Low-strain modulus, (b) high-strain modulus, (c) ultimate stress, and (d) ultimate strain of polyamides (PPTA, PAP5 to PAP8) as functions of the number of non-aromatic carbons in the polymer repeating units at three different strain rates: 1×10^8, 1×10^9, and 1×10^{10} s^{-1}. The error bars at strain rate 1×10^9 s^{-1} reflect the standard deviation calculated from three independent simulations. Although the ultimate stress and ultimate strain increase with increasing strain rate, consistent with previous studies, [111, 112, 159, 188, 191, 203, 218] the trends with respect to number of non-aromatic carbons are similar at the different strain rates.

4.4 Conclusions

MD simulations were performed to study the stress-strain response of PPTA and four related aromatic-aliphatic polyamides with different numbers of non-aromatic carbons in the polymer repeating unit. Two distinct linear stress-strain regimes were observed. It was found that the subtle differences between these polymers lead to distinct elastic and ultimate properties. The low-strain modulus (calculated from 0-2% strain) decreased with increasing aliphatic chain length while the high-strain modulus (calculated from the last 5% strain before failure) was independent of the aliphatic chain length. The trend of low-strain modulus was explained in terms of the departure from the extended chain conformations—waviness—of the polymers at zero strain. Longer aliphatic chains increased the conformational freedom of the chains and thus the waviness of the polymers, which finally decreased the low-strain modulus. The transition from low to high strain behavior was correlated with changing of dihedral angles as the chains were extended, so this behavior was due to intra-chain effects. It was also observed that polymers with an even number of non-aromatic carbon atoms exhibited a discrete inter-chain slip mechanism at the transition between the wavy and extended conformation, which was explained by the instability of the H-bonding structure in these polymers. A similar odd-even effect was observed at failure, where even polymers had lower ultimate stress. Coplanarity of the aromatic rings correlated well with the trend of ultimate stress, i.e., less coplanar rings (larger ring-ring angle) corresponded to lower ultimate stress.

Generally, the results reported here show that aromatic-aliphatic polyamides can be designed with mechanical properties comparable to or better than PPTA, yet even subtle differences in chemical composition can have strong implications for the mechanical response. Further, the correlations between structure and mechanical properties identified herein, as well as the simulation-based approach, may be extended to other similar polymers to enable tuning of mechanical properties through chemical modification.

Chapter 5

Summary and Future Work

5.1 Summary

This research aimed to study the crystal structure, intrachain interactions, and interchain interactions of high-performance polyamides that play an important role in a variety of applications, including aerospace and military applications. We focused on PPTA and four PPTA-related aromatic-aliphatic polyamides.. Since high-performance polyamides have a high performance-to-weight ratio, understanding the mechanical properties of these materials can lead to the discovery of new approaches for tuning and improving their characteristics, thereby opening new avenues for production, assembly and application of these material.

First, molecular dynamics simulations modeled PPTA and a related aromatic-aliphatic polyamide derived from a five-carbon aliphatic diacid (PAP5) with nine different reactive and non-reactive force fields. The ReaxFF force field parameter set developed by Liu et al. was identified to be the optimum for our systems after evaluating all of the nine candidate force fields based on crystal lattice parameters, intermolecular hydrogen-bonding and π-π interactions, as well as XRD patterns. Different model sizes were also compared to identify the smallest possible system, 4×4×4, capable of accurately modeling these material properties.

Next, the ReaxFF Liu force field was used to simulate stress-strain behavior in the chain and transverse-to-chain directions for PPTA and PAP5. In the chain direction, PAP5 had higher ultimate stress and failure strain than PPTA; however, the stiffness of PAP5 was lower than PPTA at low-strain (0-2%) while the reverse was observed at high-strain (last 5% before failure). This contrast, and differences in the transverse direction properties, were explained by the methylene segments of PAP5 that confer conformational freedom, enabling accommodation of low strain without stretching covalent bonds.

Lastly, in order to study the aliphatic chain length effect on the stress-strain response, we extended the models pool by varying the numbers of carbon atoms in the aliphatic chain to obtain another three aromatic-aliphatic polyamides, i.e., PAP6, PAP7, and PAP8. Tensile strain was applied to each polymer crystal in the chain direction and the mechanical response was characterized. All the polymers with aliphatic segments exhibited strain hardening, transi-

tioning from a low-strain linear regime to a high-strain linear regime. The modulus at high strain was similar for all polymers, but the modulus calculated at low strain decreased with increasing aliphatic chain length. The decrease in the low-strain modulus with increasing chain length was explained by the observation that polymers with longer aliphatic chains were wavier in the quiescent state such that they could accommodate low strain without deforming covalent bonds. Extension of wavy chains occurred through an intra-chain process for all polymers, quantified by the bond dihedral angles. In addition, for polymers with an even number of non-aromatic carbons, the strain response involved slip between chains within the hydrogen bonded sheets. The ultimate stress of the polymers exhibited an odd-even effect which was explained by differences in hydrogen bonding and ring-ring coplanarity prior to failure; polymers with an even number of carbon atoms had less favorable H-bonding and poorer ring alignment. The results revealed direct correlations between aliphatic chain length, intra- and inter-chain interactions, and the mechanical properties of polyamide crystals.

Overall, the results of this dissertation contribute to establishing the framework of fundamental knowledge needed to design and optimize high-performance polyamides for various applications.

5.2 Effect of Functional Groups on Stress-strain Response

The functional group refers to the chemical groups introduced into the polymer chain other than the aliphatic and aromatic components, which affect the inter/intra interactions and microstructure of polyamides. Examples of the chemical structures of polyamides with different functional groups are shown in Fig. 5.1.

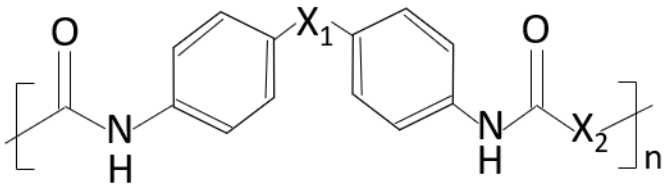

Figure 5.1: Representative chemical structures of polyamides where the X_1 and X_2 can be different functional groups. Different functional groups are expected to have different effects on the mechanical properties of the polyamide.

Side group functionality affects the polymers' molecular packing and crystallinity, thus enabling different structures to have different properties. [4, 189] The tensile strength of amine-terminated polyamides decreases with increasing number of end functional groups. [123] Some types of low T_g segments were incorporated in the polymers: modified poly(tetramethyle-

neoxide) (methyl side groups), poly(oxyethyleneglycol) and poly(ethylene/butylene). Researchers have also studied copolyetheresteramides with different hard segments. [59, 124, 125, 126, 127, 128] They found that control of the sequence distribution, the nature of the hard segments, and the flexibility and molecular weight of the soft segments allow the design of materials with reasonable low melting points and good mechanical properties, possibly allowing the polymers to be transformed by conventional extrusion or injection methods. End-group modification of hyperbranched polymers greatly affects their properties, such as the solubility, T_g, film-forming ability, and contact angle. [83] Polymers that have less pronounced bulky groups have higher T_g values, because the existence of the bulky side groups prevents the polymer chains from becoming ordered. [91] However, there is limited information available about the effects of functional groups on the mechanical properties of polyamides. Fig. 5.2 and 5.3 show functional group candidates for the polyamides to be studied in this proposed work. A slight change in the functional groups could result in different mechanical properties of the polyamides. For example, from PAP5 to PAP8, with the number of methylene units in X_1 increases, the chain is expected to be more flexible, as what we have observed from the comparison between PPTA and PAP5 in our preliminary results.

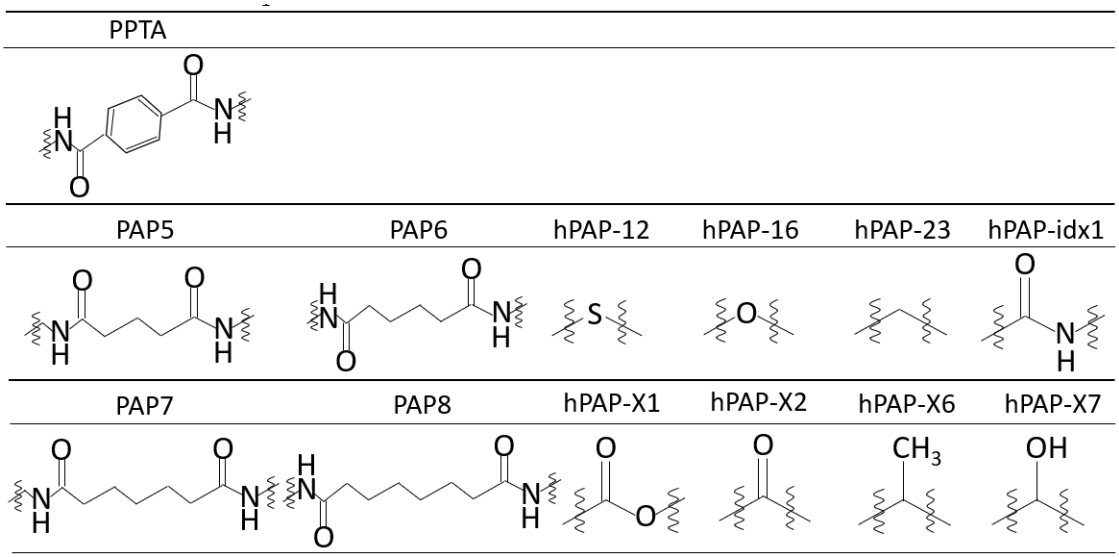

Figure 5.2: Potential functional groups in X_1 portion.

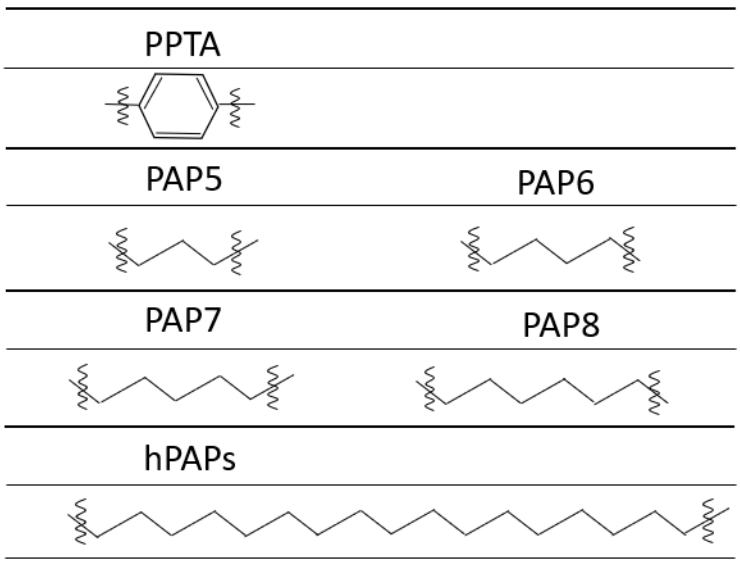

Figure 5.3: Potential functional groups in X_2 portion.

5.3 Prediction of Mechanical Properties Using Machine Learning

The ability to accurately design new molecules with targeted properties is a long-standing problem with potential applications in the design of catalysts, polymers, polymeric composites, solvents, detergents, drugs, pesticides, etc. At the heart of the problem is quantitatively determining the relationship between the structure and properties of materials. As revealed by our preliminary results, a slight change in the structure can have significant change in the mechanical properties of polyamides. Although, as pointed out in the previous two sub-sections, the length of aliphatic chain and the functional group might be factors affecting the mechanical properties of polyamides, they are probably not the only factors. Therefore, more factors should be taken into consideration, which requires a larger number of structures to be involved in the study. However, taking more factors taken into consideration will increase the complexity of the analysis because some factors might not be linearly correlated with the mechanical properties. In addition, some mechanical properties might be determined by the combined effects of multiple factors. Lastly, the number of simulations that can be run is limited due to the time and computational expense. Therefore, a new method is needed to integrate all possible factors and, at the same time, increase the efficiency and minimize the computational cost.

What we propose to use here is machine learning, which is a powerful method that is becoming more and more popular in different fields. Machine learning can be defined as a computer program which is able to learn from experience by being trained using examples, to im-

prove its performance at a certain task. [115] According to this definition, in our study, the task is predicting the mechanical properties of polyamides based on given structural information; performance is how accurate the predicted properties is relative to the actual properties (simulation or experimental); and experience is training the program using either experimental or simulation data of structures and mechanical properties. Such combination of machine learning with experiments and MD simulations can result in quick and efficient design and improvement of polyamides.

Such a strategy has been successfully applied by materials scientists in a variety of studies. Examples include predicting the intrinsic electrical breakdown strength of solids, [89] classifying binary inorganic compounds into different crystal structure types, [138, 139] predicting the band gap of insulators by training on available experimental data, [192] estimating the mechanical and thermal properties of polymers based on group contributions, [184] and rapidly calculating forces on atoms in any given configuration for accelerating molecular dynamics. [15]

However, there is no study focusing on predicting the mechanical properties of polyamides using the combination of machine learning and MD simulations. Given the important role polyamides play in different applications due to their superior properties, it is beneficial to develop a model to quantitatively correlate the mechanical properties to the molecular descriptors. Ideally, eventually it will be possible to develop new polyamides with desired mechanical properties based on the applications.

To build quantitative structure-property relationship for polyamides, the first question that arises is how to describe the structures. Fortunately, molecular descriptors can serve for this purpose, which translates the chemical information of a molecular structure into a series of useful numbers. [176] The numerical values of molecular descriptors are used to quantitatively describe the physical and chemical information of the molecules.

Converting data of the descriptors and properties (either from experiments or simulations) of polymers into a useful database, and applying machine learning method to train polyamide design models is what we hope to achieve. This idea is aligned well with the goals of the Materials Genome Initiative, [63] launched by the United States government in 2009—to discover, manufacture and deploy advanced materials twice as fast with a lower cost.

5.4 Concluding Remarks

Overall, we studied the stress-strain response of a high-performance polyamide PPTA and four PPTA-related aromatic-aliphatic polyamides.

This dissertation has: (i) provided insight into the important fundamental question of how the processibility of high-performance polyamide PPTA can be improved by modification without compromising the mechanical properties; (ii) contributed significantly to the high-performance polyamides from the unexplored structure-properties perspective; (iii) explained the strong anisotropy in stress-strain response observed on crystalline polyamides via a new mechanism; (iv) provided new insight into how inter and intrachain interactions affect

the stress-strain response at the atomic scale; (v) emphasized the critical role of the odd-even effect observed in both the elastic and ultimate properties of polyamides; (vi) explained the origin of the odd-even effect by attributing it to the structure of hydrogen bonding network; (vii) established a force field selection framework that can be applied to other polymeric crystals; and (viii) shed light on the mechanisms by which atomic structure can alter atomic interactions to affect the mechanical properties of crystalline polymers.

Various industries including aerospace and military have been using high-performance polymers, such as PPTA, in many applications, but a lack of fundamental understanding restricts their design for harsher environments and applications demanding higher performance. This dissertation aimed to establish and quantify relationships between structure, processing, and mechanical properties of high-performance polyamides to ultimately enable rational design of components, devices, and systems with improved performance.

Supporting Information

- Movie S1: Time evolution of stress-strain response, radial distribution functions, and model snapshots for PPTA strained in the x-direction
- Movie S2: Time evolution of stress-strain response, radial distribution functions, and model snapshots for PPTA strained in the y-direction
- Movie S3: Time evolution of stress-strain response, radial distribution functions, and model snapshots for PPTA strained in the z-direction
- Movie S4: Time evolution of stress-strain response, radial distribution functions, and model snapshots for PAP5 strained in the x-direction
- Movie S5: Time evolution of stress-strain response, radial distribution functions, and model snapshots for PAP5 strained in the y-direction
- Movie S6: Time evolution of stress-strain response, radial distribution functions, and model snapshots for PAP5 strained in the z-direction
- Movie S7-8: the stress-strain simulations of PPTA shown from the x- and y-directions (chain and H-bond directions)
- Movie S9-10: the stress-strain simulations of PAP5 shown from the x- and y-directions (chain and H-bond directions)
- Movie S11-12: the stress-strain simulations of PAP6 shown from the x- and y-directions (chain and H-bond directions)
- Movie S13-14: the stress-strain simulations of PAP7 shown from the x- and y-directions (chain and H-bond directions)
- Movie S15-16: the stress-strain simulations of PAP8 shown from the x- and y-directions (chain and H-bond directions)

Bibliography

[1] Tatyana Ageyeva, Ilya Sibikin, and József Gábor Kovács. "A review of thermoplastic resin transfer molding: Process modeling and simulation". In: *Polymers* 11.10 (2019), p. 1555.

[2] Satyam Agrawalla and Adri CT Van Duin. "Development and application of a ReaxFF reactive force field for hydrogen combustion". In: *The Journal of Physical Chemistry A* 115.6 (2011), pp. 960–972.

[3] Dawelbeit Ahmed et al. "Microstructural developments of poly (p-phenylene terephthalamide) fibers during heat treatment process: a review". In: *Materials Research* 17 (2014), pp. 1180–1200.

[4] Ozcan Altintas and Christopher Barner-Kowollik. "Single chain folding of synthetic polymers by covalent and non-covalent interactions: current status and future perspectives". In: *Macromolecular rapid communications* 33.11 (2012), pp. 958–971.

[5] Seyed Mojtaba Amininasab et al. "Preparation and characterization of novel thermostable polyamides bearing different photoactive pendent architectures with antibacterial properties". In: *Chinese Journal of Polymer Science* 34.6 (2016), pp. 766–776.

[6] Adolf Baeyer. "Ueber regelmässigkeiten im schmelzpunkt homologer verbindungen". In: *Berichte der deutschen chemischen Gesellschaft* 10.2 (1877), pp. 1286–1288.

[7] Camille Bakkali-Hassani et al. "Synthesis of polyamide 6 with aramid units by combination of anionic ring-opening and condensation reactions". In: *European Polymer Journal* 102 (2018), pp. 231–237.

[8] Parthasarthi Bandyopadhyay et al. "Di-tert-butyl containing semifluorinated poly (ether amide) s: Synthesis, characterization and gas transport properties". In: *Journal of membrane science* 447 (2013), pp. 413–423.

[9] RH Baughman, H Gleiter, and N Sendfeld. "Deformation and microstructure of extended-chain polydiacetylene crystals". In: *Journal of Polymer Science: Polymer Physics Edition* 13.10 (1975), pp. 1871–1879.

[10] Vernon L Bell, Billy L Stump, and Helen Gager. "Polyimide structure–property relationships. II. Polymers from isomeric diamines". In: *Journal of Polymer Science: Polymer Chemistry Edition* 14.9 (1976), pp. 2275–2291.

[11] Debaditya Bera, Venkat Padmanabhan, and Susanta Banerjee. “Highly gas permeable polyamides based on substituted triphenylamine”. In: *Macromolecules* 48.13 (2015), pp. 4541–4554.

[12] BIOVIA. *BIOVIA Material Studio*. Last accessed 16 February 2021. 2020. URL: http://www.3ds.com/products-services/biovia/products/molecular-modeling-simulation/biovia-materials-studio.

[13] Soumendu Bisoi et al. “Aromatic polyamides containing trityl substituted triphenylamine: Gas transport properties and molecular dynamics simulations”. In: *Journal of Membrane Science* 522 (2017), pp. 77–90.

[14] Andrew D Bond. “On the crystal structures and melting point alternation of the n-alkyl carboxylic acids”. In: *New journal of chemistry* 28.1 (2004), pp. 104–114.

[15] Venkatesh Botu and Rampi Ramprasad. “Adaptive machine learning framework to accelerate ab initio molecular dynamics”. In: *International Journal of Quantum Chemistry* 115.16 (2015), pp. 1074–1083.

[16] Bernard R Brooks et al. “CHARMM: the biomolecular simulation program”. In: *Journal of computational chemistry* 30.10 (2009), pp. 1545–1614.

[17] JR Brown and BC Ennis. “Thermal analysis of Nomex® and Kevlar® fibers”. In: *Textile Research Journal* 47.1 (1977), pp. 62–66.

[18] Benoît Brulé, Jean Louis Halary, and Lucien Monnerie. “Molecular analysis of the plastic deformation of amorphous semi-aromatic polyamides”. In: *Polymer* 42.21 (2001), pp. 9073–9083.

[19] John Andrew Brydson. *Plastics materials*. Elsevier, 1999.

[20] Joanne Budzien, Aidan P Thompson, and Sergey V Zybin. “Reactive molecular dynamics simulations of shock through a single crystal of pentaerythritol tetranitrate”. In: *The Journal of Physical Chemistry B* 113.40 (2009), pp. 13142–13151.

[21] Stefano Burattini et al. “A supramolecular polymer based on tweezer-type π-π stacking interactions: molecular design for healability and enhanced toughness”. In: *Chemistry of Materials* 23.1 (2011), pp. 6–8.

[22] Wallace H Carothers and Gerard J Berchet. “Studies on polymerization and ring formation. VIII. Amides from ε-aminocaproic acid”. In: *Journal of the American Chemical Society* 52.12 (1930), pp. 5289–5291.

[23] David A Case et al. “The Amber biomolecular simulation programs”. In: *Journal of computational chemistry* 26.16 (2005), pp. 1668–1688.

[24] Patrick E Cassidy. “Thermally stable polymers, synthesis and properties”. In: (1980).

[25] AJ Castro. *Method for making microporous products. US Pat: 4247498*. 1981.

[26] Fidel Castro-Marcano et al. “Combustion of an Illinois No. 6 coal char simulated using an atomistic char representation and the ReaxFF reactive force field”. In: *Combustion and Flame* 159.3 (2012), pp. 1272–1285.

[27] Tanya L Chantawansri, In-Chul Yeh, and Alex J Hsieh. "Investigating the glass transition temperature at the atom-level in select model polyamides: A molecular dynamics study". In: *Polymer* 81 (2015), pp. 50–61.

[28] Ming Cheng, Weinong Chen, and Tusit Weerasooriya. "Experimental investigation of the transverse mechanical properties of a single Kevlar® KM2 fiber". In: *International Journal of Solids and Structures* 41.22-23 (2004), pp. 6215–6232.

[29] Ming Cheng, Weinong Chen, and Tusit Weerasooriya. "Mechanical properties of Kevlar® KM2 single fiber". In: *J. Eng. Mater. Technol.* 127.2 (2005), pp. 197–203.

[30] Kimberly Chenoweth, Adri CT Van Duin, and William A Goddard. "ReaxFF reactive force field for molecular dynamics simulations of hydrocarbon oxidation". In: *The Journal of Physical Chemistry A* 112.5 (2008), pp. 1040–1053.

[31] Kimberly Chenoweth, Adri CT Van Duin, and William A Goddard III. "The ReaxFF Monte Carlo reactive dynamics method for predicting atomistic structures of disordered ceramics: application to the Mo3VOx Catalyst". In: *Angewandte Chemie International Edition* 48.41 (2009), pp. 7630–7634.

[32] H Cherdron. "Tailoring of thermotropic liquid-crystalline main-chain polymers". In: *Makromolekulare Chemie. Macromolecular Symposia*. Vol. 33. 1. Wiley Online Library. 1990, pp. 85–95.

[33] H Cherdron et al. "Miscible blends of polybenzimidazole and polyaramides with polyvinylpyrrolidone". In: *Journal of applied polymer science* 53.5 (1994), pp. 507–512.

[34] Sanjib C Chowdhury and John W Gillespie Jr. "A molecular dynamics study of the effects of hydrogen bonds on mechanical properties of Kevlar® crystal". In: *Computational Materials Science* 148 (2018), pp. 286–300.

[35] Sanjib C Chowdhury, Subramani Sockalingam, and John W Gillespie. "Molecular dynamics modeling of the effect of axial and transverse compression on the residual tensile properties of ballistic fiber". In: *Fibers* 5.1 (2017), p. 7.

[36] Terry L St Clair and David A Yamaki. *Process for preparing solvent resistant, thermoplastic aromatic poly (imidesulfone)*. US Patent 4,489,027. 1984.

[37] Terry L St Clair and David A Yamaki. *Solvent resistant, thermoplastic aromatic poly (imidesulfone) and process for preparing same*. US Patent 4,398,021. 1983.

[38] Julia Cline, Vincent Wu, and Paul Moy. *Assessment of the Tensile properties for single fibers*. Tech. rep. US Army Research Laboratory Aberdeen Proving Ground United States, 2018.

[39] National Research Council et al. *Polymer science and engineering: the shifting research frontiers*. National Academies Press, 1994.

[40] IG Crouch et al. "Fibres, textiles and protective apparel". In: *The science of armour materials*. Elsevier, 2017, pp. 269–330.

[41] Mariana-Dana Damaceanu et al. “Organosoluble asymmetric aromatic polyamides bearing pendent phenoxy groups”. In: *Polymer international* 60.8 (2011), pp. 1248–1258.

[42] Pnina Dauber Osguthorpe et al. “Structure and energetics of ligand binding to proteins: Escherichia coli dihydrofolate reductase-trimethoprim, a drug-receptor system”. In: *Proteins: Structure, Function, and Bioinformatics* 4.1 (1988), pp. 31–47.

[43] J De Abajo and JG De la Campa. “Processable aromatic polyimides”. In: *Progress in polyimide chemistry I* (1999), pp. 23–59.

[44] Emmanuel Debeaupte et al. “In situ polycondensation for synthesis of composites of elastomeric matrixes and wholly aromatic polyamides”. In: *Chemistry of materials* 4.5 (1992), pp. 1123–1128.

[45] BL Deopura et al. *Polyesters and polyamides*. Elsevier, 2008.

[46] Yogesh S Deshmukh et al. “Conformational and structural changes with increasing methylene segment length in aromatic–aliphatic polyamides”. In: *Macromolecules* 49.3 (2016), pp. 950–962.

[47] Ram Devanathan, Matthias Krack, and Marjorie Bertolus. *Classical molecular dynamics simulation of nuclear fuels*. Tech. rep. 2015.

[48] Ram Devanathan et al. “Modeling and simulation of nuclear fuel materials”. In: *Energy & Environmental Science* 3.10 (2010), pp. 1406–1426.

[49] MG Dobb, DJ Johnson, and BP Saville. “Compressional behaviour of Kevlar fibres”. In: *Polymer* 22.7 (1981), pp. 960–965.

[50] Leela S Dodda et al. “LigParGen web server: an automatic OPLS-AA parameter generator for organic ligands”. In: *Nucleic acids research* 45.W1 (2017), W331–W336.

[51] Fernando L Dri et al. “Evaluation of reactive force fields for prediction of the thermomechanical properties of cellulose Iβ”. In: *Computational Materials Science* 109 (2015), pp. 330–340.

[52] Maher Z Elsabee, Mohamed A Nassar, and EM Salah. “Preparation and characterization of some aromatic/aliphatic polyamides”. In: *American Journal of Polymer Science* 2.1 (2012), pp. 7–13.

[53] Wutong Feng et al. “Effect of Aliphatic Diacid Chain Length on Properties of Semiaromatic Copolyamides Based on PA10T and Their Theoretical Study”. In: *Industrial & Engineering Chemistry Research* 58.17 (2019), pp. 7217–7226.

[54] Juan J Ferreiro et al. “Polyisophthalamides with heteroaromatic pendent rings: synthesis, physical properties, and water uptake”. In: *Journal of Polymer Science Part A: Polymer Chemistry* 43.21 (2005), pp. 5300–5311.

[55] E Ferrero et al. “Synthesis and characterization of aromatic polyamides containing alkylphthalimido pendent groups”. In: *Journal of Polymer Science Part A: Polymer Chemistry* 40.21 (2002), pp. 3711–3724.

[56] Irma Flores et al. “Unexpected Structural Properties in the Saturation Region of the Odd–Even Effects in Aliphatic Polyethers: Influence of Crystallization Conditions”. In: *Macromolecules* (2022).

[57] Joseph C Fogarty et al. “A reactive molecular dynamics simulation of the silica-water interface”. In: *The Journal of chemical physics* 132.17 (2010), p. 174704.

[58] M. J. Frisch et al. *Gaussian˜09 Revision E.01*. Gaussian Inc. Wallingford CT. 2013.

[59] José M García et al. “High-performance aromatic polyamides”. In: *Progress in polymer science* 35.5 (2010), pp. 623–686.

[60] RJ Gaymans and Sybolt Harkema. “Melting behavior of aliphatic and aromatic diamides”. In: *Journal of Polymer Science: Polymer Physics Edition* 15.3 (1977), pp. 587–590.

[61] Feliciano Giustino. *Materials modelling using density functional theory: properties and predictions*. Oxford University Press, 2014.

[62] William A Goddard et al. “Structures, mechanisms, and kinetics of selective ammoxidation and oxidation of propane over multi-metal oxide catalysts”. In: *Topics in catalysis* 50.1 (2008), pp. 2–18.

[63] U.S. Federal government. *Materials Genome Initiative*. Last accessed 4 January 20221. 2009. URL: `https://www.mgi.gov/`.

[64] Jeff Greeley et al. “Computational high-throughput screening of electrocatalytic materials for hydrogen evolution”. In: *Nature materials* 5.11 (2006), pp. 909–913.

[65] JH Greenwood and PG Rose. “Compressive behaviour of Kevlar 49 fibres and composites”. In: *Journal of materials science* 9.11 (1974), pp. 1809–1814.

[66] M Grujicic et al. “Filament-level modeling of aramid-based high-performance structural materials”. In: *Journal of materials engineering and performance* 20.8 (2011), pp. 1401–1413.

[67] Mica Grujicic et al. “Molecular-level computational investigation of mechanical transverse behavior of p-phenylene terephthalamide (PPTA) fibers”. In: *Multidiscipline Modeling in Materials and Structures* 9.4 (2013), pp. 462–498.

[68] J Hafner. “Atomic-scale computational materials science”. In: *Acta Materialia* 48.1 (2000), pp. 71–92.

[69] Mohsen Hajibeygi, Meisam Shabanian, and Majid Khodaei-Tehrani. “New heat resistant nanocomposites reinforced silicate nanolayers containing triazine rings based on polyamide: synthesis, characterization, and flame retardancy study”. In: *Polymer Composites* 37.1 (2016), pp. 188–198.

[70] WE Hanford and RM Joyce. “Polymeric amides from epsilon-caprolactam”. In: *Journal of Polymer Science* 3.2 (1948), pp. 167–172.

[71] Michael Ryan Hansen, Robert Graf, and Hans Wolfgang Spiess. “Solid-state NMR in macromolecular systems: insights on how molecular entities move”. In: *Accounts of chemical research* 46.9 (2013), pp. 1996–2007.

[72] John WS Hearle and William Ernest Morton. *Physical properties of textile fibres*. Woodhead Publishing Limited: Cambridge, 2008.

[73] Paul M Hergenrother. "High performance thermoplastics". In: *Die Angewandte Makromolekulare Chemie: Applied Macromolecular Chemistry and Physics* 145.1 (1986), pp. 323–341.

[74] Friedrich Herold and Arnold Schneller. "High-Performance Polymers". In: *Advanced Materials* 4.3 (1992), pp. 143–152.

[75] R Hill and EE Walker. "Polymer constitution and fiber properties". In: *Journal of polymer science* 3.5 (1948), pp. 609–630.

[76] Janet Ho, Leon Govaert, and Marcel Utz. "Plastic deformation of glassy polymers: correlation between shear activation volume and entanglement density". In: *Macromolecules* 36.19 (2003), pp. 7398–7404.

[77] Pierre Hohenberg and Walter Kohn. "Inhomogeneous electron gas". In: *Physical review* 136.3B (1964), B864.

[78] Christopher W Hollars, Stephen M Lane, and Thomas Huser. "Controlled non-classical photon emission from single conjugated polymer molecules". In: *Chemical physics letters* 370.3-4 (2003), pp. 393–398.

[79] William G Hoover. "Canonical dynamics: Equilibrium phase-space distributions". In: *Physical review A* 31.3 (1985), p. 1695.

[80] William G Hoover. "Constant-pressure equations of motion". In: *Physical Review A* 34.3 (1986), p. 2499.

[81] Ying-Chi Huang et al. "Solvent Response and Protonation Effects of Novel Aramides Containing Pyridine and Unsymmetrical Carbazole Moieties". In: *Macromolecules* 46.18 (2013), pp. 7443–7450.

[82] JY Jadhav, J Preston, and WR Krigbaum. "Aromatic rigid chain copolymers. I. Synthesis, structure, and solubility of phenyl-substituted para-linked aromatic random copolyamides". In: *Journal of Polymer Science Part A: Polymer Chemistry* 27.4 (1989), pp. 1175–1195.

[83] Mitsutoshi Jikei and Masa-aki Kakimoto. "Dendritic aromatic polyamides and polyimides". In: *Journal of Polymer Science Part A: Polymer Chemistry* 42.6 (2004), pp. 1293–1309.

[84] Chuan-Ming Jin et al. "Ag (I) coordination polymers with flexible bis-imidazole ligands: 2D interwoven structure and wavy layer network based on silver–silver interactions". In: *Journal of Molecular Structure* 921.1-3 (2009), pp. 58–62.

[85] Amar M Kamat, Adri CT van Duin, and Alexei Yakovlev. "Molecular dynamics simulations of laser-induced incandescence of soot using an extended ReaxFF reactive force field". In: *The Journal of Physical Chemistry A* 114.48 (2010), pp. 12561–12572.

[86] P Kanakalatha et al. "Some studies on polyblends of poly (p-phenyleneterephthalamide) and nylon-6". In: *Polymer* 24.5 (1983), pp. 621–625.

[87] Kisuk Kang et al. “Electrodes with high power and high capacity for rechargeable lithium batteries”. In: *Science* 311.5763 (2006), pp. 977–980.

[88] Saeed Khademinejad et al. “Poly (ether ether sulfone amide) s as a new category of processable heat-resistant polymers”. In: *Designed Monomers and Polymers* 19.6 (2016), pp. 553–559.

[89] Chiho Kim, Ghanshyam Pilania, and Ramamurthy Ramprasad. “From organized high-throughput data to phenomenological theory using machine learning: the example of dielectric breakdown”. In: *Chemistry of Materials* 28.5 (2016), pp. 1304–1311.

[90] J Kim et al. “The modified-single fiber test: A methodology for monitoring ballistic performance”. In: *Journal of applied polymer science* 108.2 (2008), pp. 876–886.

[91] Oliver Kreye et al. “Structurally diverse polyamides obtained from monomers derived via the Ugi multicomponent reaction”. In: *Chemistry–A European Journal* 18.18 (2012), pp. 5767–5776.

[92] WR Krigbaum et al. “Nematogenic aromatic block copolymers of rigid and flexible units. II. Phase equilibria”. In: *Journal of Polymer Science Part B: Polymer Physics* 25.5 (1987), pp. 1043–1055.

[93] K Krishnan et al. “Numerical simulation of ceramic composite armor subjected to ballistic impact”. In: *Composites Part B: Engineering* 41.8 (2010), pp. 583–593.

[94] Abdulaziz Kurdi and Li Chang. “Recent advances in high performance polymers—tribological aspects”. In: *Lubricants* 7.1 (2019), p. 2.

[95] Abdulaziz Kurdi, Wen Hao Kan, and Li Chang. “Tribological behaviour of high performance polymers and polymer composites at elevated temperature”. In: *Tribology International* 130 (2019), pp. 94–105.

[96] Ming Li. “Study on melting and polymorphic behavior of poly (decamethylene terephthalamide)”. In: *Journal of Polymer Science Part B: Polymer Physics* 57.8 (2019), pp. 465–472.

[97] S-G Li et al. “Wet spinning of integrally skinned hollow fiber membranes by a modified dual-bath coagulation method using a triple orifice spinneret”. In: *Journal of membrane science* 94.1 (1994), pp. 329–340.

[98] Youyong Li and William A Goddard. “Nylon 6 crystal structures, folds, and lamellae from theory”. In: *Macromolecules* 35.22 (2002), pp. 8440–8455.

[99] Jaeyoung Lim et al. “Effects of gage length, loading rates, and damage on the strength of PPTA fibers”. In: *International Journal of Impact Engineering* 38.4 (2011), pp. 219–227.

[100] Szu-Hui Lim, Zhong-Zhen Yu, and Yiu-Wing Mai. “Effects of loading rate and temperature on tensile yielding and deformation mechanisms of nylon 6-based nanocomposites”. In: *Composites Science and Technology* 70.13 (2010), pp. 1994–2002.

[101] Guey-Sheng Liou, Yi-Kai Fang, and Hung-Ju Yen. "Synthesis and properties of non-coplanar rigid-rod aromatic polyamides containing phenyl or naphthyl substituents". In: *Journal of Polymer Research* 14.2 (2007), pp. 147–155.

[102] Lianchi Liu et al. "ReaxFF-lg: Correction of the ReaxFF reactive force field for London dispersion, with applications to the equations of state for energetic materials". In: *The Journal of Physical Chemistry A* 115.40 (2011), pp. 11016–11022.

[103] CW Lomicka et al. "Improving ballistic fiber strength: insights from experiment and simulation". In: *Dynamic Behavior of Materials, Volume 1*. Springer, 2014, pp. 187–193.

[104] Jia-Wei Long et al. "Tuning the Pendent Groups of Semiaromatic Polyamides toward High Performance". In: *Macromolecules* 53.9 (2020), pp. 3504–3513.

[105] Bernard Lotz. "Original Crystal Structures of Even–Even Polyamides Made of Pleated and Rippled Sheets". In: *Macromolecules* 54.2 (2021), pp. 551–564.

[106] Hegoi Manzano et al. "Confined water dissociation in microporous defective silicates: mechanism, dipole distribution, and impact on substrate properties". In: *Journal of the American Chemical Society* 134.4 (2012), pp. 2208–2215.

[107] Keith Marchildon. "Polyamides–still strong after seventy years". In: *Macromolecular reaction engineering* 5.1 (2011), pp. 22–54.

[108] Thomas R Mattsson et al. "First-principles and classical molecular dynamics simulation of shocked polymers". In: *Physical Review B* 81.5 (2010), p. 054103.

[109] Stephen L Mayo, Barry D Olafson, and William A Goddard. "DREIDING: a generic force field for molecular simulations". In: *Journal of Physical chemistry* 94.26 (1990), pp. 8897–8909.

[110] A. D. McLean and G. S. Chandler. "Contracted Gaussian basis sets for molecular calculations. I. Second row atoms, Z=11–18". In: *The Journal of Chemical Physics* 72.10 (1980), pp. 5639–5648.

[111] Brian Mercer, Edward Zywicz, and Panayiotis Papadopoulos. "A molecular dynamics-based analysis of the influence of strain-rate and temperature on the mechanical strength of PPTA crystallites". In: *Polymer* 129 (2017), pp. 92–104.

[112] Brian Mercer, Edward Zywicz, and Panayiotis Papadopoulos. "Molecular dynamics modeling of PPTA crystallite mechanical properties in the presence of defects". In: *Polymer* 114 (2017), pp. 329–347.

[113] Brian Scott Mercer. "Molecular Dynamics Modeling of PPTA Crystals in Aramid Fibers". PhD thesis. UC Berkeley, 2016.

[114] Manish Kumar Mishra et al. "Odd–even effect in the elastic modulii of α,ω-alkanedicarboxylic acids". In: *Journal of the American Chemical Society* 135.22 (2013), pp. 8121–8124.

[115] Tom Mitchell. "Machine learning". In: (1997).

[116] Hajime Miyake et al. “Molecular weight dependence of tensile properties in poly (vinyl alcohol) fibers”. In: *Polymer journal* 32.12 (2000), pp. 1049–1051.

[117] Neil E Moe and MD Ediger. “Molecular dynamics computer simulation of polyisoprene local dynamics in dilute toluene solution”. In: *Macromolecules* 28.7 (1995), pp. 2329–2338.

[118] Susanna Monti et al. “Exploring the conformational and reactive dynamics of biomolecules in solution using an extended version of the glycine reactive force field”. In: *Physical Chemistry Chemical Physics* 15.36 (2013), pp. 15062–15077.

[119] PW Morgan. “Synthesis and properties of aromatic and extended chain polyamides”. In: *Macromolecules* 10.6 (1977), pp. 1381–1390.

[120] PW Morgan and SL Kwolek. “Polymides from phenylenediamines and aliphatic diacids”. In: *Macromolecules* 8.2 (1975), pp. 104–111.

[121] Jonathan E Mueller, Adri CT Van Duin, and William A Goddard III. “Application of the ReaxFF reactive force field to reactive dynamics of hydrocarbon chemisorption and decomposition”. In: *The Journal of Physical Chemistry C* 114.12 (2010), pp. 5675–5685.

[122] Shinsuke Nakamoto, Kohji Tashiro, and Akikazu Matsumoto. “Vibrational spectroscopic study on the molecular deformation mechanism of a poly (trans-1, 4-diethyl muconate) single crystal subjected to tensile stress”. In: *Macromolecules* 36.1 (2003), pp. 109–117.

[123] A Sultan Nasar, Mitsutoshi Jikei, and Masa-aki Kakimoto. “Synthesis and properties of polyurethane elastomers crosslinked with amine-terminated AB2-type hyperbranched polyamides”. In: *European polymer journal* 39.6 (2003), pp. 1201–1208.

[124] MCEJ Niesten, H Bosch, and RJ Gaymans. “Influence of extenders on thermal and elastic properties of segmented copolyetheresteraramides”. In: *Journal of applied polymer science* 81.7 (2001), pp. 1605–1613.

[125] MCEJ Niesten and RJ Gaymans. “Tensile and elastic properties of segmented copolyetheresteramides with uniform aramid units”. In: *Polymer* 42.14 (2001), pp. 6199–6207.

[126] MCEJ Niesten, JW Ten Brinke, and RJ Gaymans. “Segmented copolyetheresteraramids with extended poly (tetramethyleneoxide) segments”. In: *Polymer* 42.4 (2001), pp. 1461–1469.

[127] MCEJ Niesten, R Tol, and RJ Gaymans. “Influence of type of uniform aromatic amide units on segmented copolyetheresteramides”. In: *Polymer* 42.3 (2001), pp. 931–939.

[128] MCEJ Niesten et al. “Structural changes of segmented copolyetheresteramides with uniform aramid units induced by melting and deformation”. In: *Polymer* 42.3 (2001), pp. 1131–1142.

[129] Piyarat Nimmanpipug, Kohji Tashiro, and Orapin Rangsiman. “Factors governing the three-dimensional hydrogen-bond network structure of poly (m-phenylene isophthalamide) and a series of its model compounds. 3. Energy terms indispensable to the crystal structure prediction”. In: *The Journal of Physical Chemistry B* 107.33 (2003), pp. 8343–8350.

[130] Piyarat Nimmanpipug et al. “Factors governing the three-dimensional hydrogen bond network structure of poly (m-phenylene isophthalamide) and a series of its model compounds:(1) Systematic classification of structures analyzed by the X-ray diffraction method”. In: *The Journal of Physical Chemistry B* 106.27 (2002), pp. 6842–6848.

[131] Takashi Nishino, Kiyofumi Takano, and Katsuhiko Nakamae. “Elastic modulus of the crystalline regions of cellulose polymorphs”. In: *Journal of Polymer Science Part B: Polymer Physics* 33.11 (1995), pp. 1647–1651.

[132] Yunyin Niu, Hongwei Hou, and Yu Zhu. “Self-assembly of d 10 metal adduct polymers bridged by bipyridyl-based ligands”. In: *Journal of Cluster Science* 14.4 (2003), pp. 483–493.

[133] MG Northolt. “X-ray diffraction study of poly (p-phenylene terephthalamide) fibres”. In: *European Polymer Journal* 10.9 (1974), pp. 799–804.

[134] MG Northolt and JJ Van Aartsen. “On the crystal and molecular structure of poly-(p-phenylene terephthalamide)”. In: *Journal of Polymer Science: Polymer Letters Edition* 11.5 (1973), pp. 333–337.

[135] Xianqiang Pei and Klaus Friedrich. “Sliding wear properties of PEEK, PBI and PPP”. In: *Wear* 274 (2012), pp. 452–455.

[136] Shumin Peng et al. “A novel synthetic strategy for preparing semi-aromatic components modified polyamide 6 polymer”. In: *Journal of Polymer Science Part A: Polymer Chemistry* 56.9 (2018), pp. 959–967.

[137] SJ Picken, S Van der Zwaag, and MG Northolt. “Molecular and macroscopic orientational order in aramid solutions: a model to explain the influence of some spinning parameters on the modulus of aramid yarns”. In: *Polymer* 33.14 (1992), pp. 2998–3006.

[138] Ghanshyam Pilania, James E Gubernatis, and TJPRB Lookman. “Structure classification and melting temperature prediction in octet AB solids via machine learning”. In: *Physical Review B* 91.21 (2015), p. 214302.

[139] Ghanshyam Pilania, JE Gubernatis, and T Lookman. “Classification of octet AB-type binary compounds using dynamical charges: a materials informatics perspective”. In: *Scientific reports* 5.1 (2015), pp. 1–9.

[140] Michael C Pitman and Adri CT Van Duin. “Dynamics of confined reactive water in smectite clay–zeolite composites”. In: *Journal of the American Chemical Society* 134.6 (2012), pp. 3042–3053.

[141] Steve Plimpton. "Fast parallel algorithms for short-range molecular dynamics". In: *Journal of computational physics* 117.1 (1995), pp. 1–19.

[142] Dusan C Prevorsek, Young D Kwon, and Hong B Chin. "Analysis of the temperature rise in the projectile and extended chain polyethylene fiber composite armor during ballistic impact and penetration". In: *Polymer Engineering & Science* 34.2 (1994), pp. 141–152.

[143] R Bruce Prime, Bernhard Wunderlich, and Louis Melillo. "Extended-chain crystals. V. Thermal analysis and electron microscopy of the melting process in polyethylene". In: *Journal of Polymer Science Part A-2: Polymer Physics* 7.12 (1969), pp. 2091–2097.

[144] Cristina Prisacariu and Elena Scortanu. "Influence of the type of chain extender and urethane group content on the mechanical properties of polyurethane elastomers with flexible hard segments". In: *High Performance Polymers* 23.4 (2011), pp. 308–313.

[145] Obaidur Rahaman et al. "Development of a ReaxFF reactive force field for glycine and application to solvent effect and tautomerization". In: *The Journal of Physical Chemistry B* 115.2 (2011), pp. 249–261.

[146] Y Rao, AJ Waddon, and RJ Farris. "Structure–property relation in poly (p-phenylene terephthalamide)(PPTA) fibers". In: *Polymer* 42.13 (2001), pp. 5937–5946.

[147] Y Rao, AJ Waddon, and RJ Farris. "The evolution of structure and properties in poly (p-phenylene terephthalamide) fibers". In: *Polymer* 42.13 (2001), pp. 5925–5935.

[148] David Raymand et al. "Water adsorption on stepped ZnO surfaces from MD simulation". In: *Surface science* 604.9-10 (2010), pp. 741–752.

[149] Christiaan de Ruijter et al. "Synthesis and characterization of rod- coil poly (amide-block-aramid) alternating block copolymers". In: *Macromolecules* 39.11 (2006), pp. 3824–3829.

[150] GC Rutledge and UW Suter. "Calculation of Mechanical Properties of Poly (p-phenylene terephthalamide) by Atomistic Modelling". In: *Polymer* 32.12 (1991), pp. 2179–2189.

[151] GC Rutledge, UW Suter, and CD Papaspyrides. "Analysis of structure of polymorphism in poly (p-phenyleneterephthalamide) through correlation of simulation and experiment". In: *Macromolecules* 24.8 (1991), pp. 1934–1943.

[152] S-P Rwei et al. "Synthesis and characterization of copolyamides derived from novel aliphatic bio-based diamine". In: *Journal of Applied Polymer Science* 135.48 (2018), p. 46878.

[153] Syang-Peng Rwei et al. "Synthesis of low melting temperature aliphatic-aromatic copolyamides derived from novel bio-based semi aromatic monomer". In: *Polymers* 10.7 (2018), p. 793.

[154] Ichiro Sakurada and Keisuke Kaji. "Relation between the polymer conformation and the elastic modulus of the crystalline region of polymer". In: *Journal of Polymer Science Part C: Polymer Symposia*. Vol. 31. 1. Wiley Online Library. 1970, pp. 57–76.

[155] Katja Schmitz and Ute Schepers. "Polyamides as artificial transcription factors: novel tools for molecular medicine?" In: *Angewandte Chemie International Edition* 43.19 (2004), pp. 2472–2475.

[156] Markus Scholl, Zuzana Kadlecova, and Harm-Anton Klok. "Dendritic and hyperbranched polyamides". In: *Progress in Polymer Science* 34.1 (2009), pp. 24–61.

[157] Thomas P Senftle et al. "The ReaxFF reactive force-field: development, applications and future directions". In: *npj Computational Materials* 2.1 (2016), pp. 1–14.

[158] Yong Shen et al. "Facile preparation of bio-based polyesters from furandicarboxylic acid and long chain diols via asymmetric monomer strategy". In: *Green Chemistry* 19.20 (2017), pp. 4930–4938.

[159] VPW Shim, CT Lim, and KJ Foo. "Dynamic mechanical properties of fabric armour". In: *International Journal of Impact Engineering* 25.1 (2001), pp. 1–15.

[160] J Singletary et al. "The transverse compression of PPTA fibers Part I Single fiber transverse compression testing". In: *Journal of Materials Science* 35.3 (2000), pp. 573–581.

[161] John K Smith and David A Hounshell. "Wallace H. Carothers and fundamental research at Du Pont". In: *Science* 229.4712 (1985), pp. 436–442.

[162] Subramani Sockalingam et al. "Recent advances in modeling and experiments of Kevlar ballistic fibrils, fibers, yarns and flexible woven textile fabrics–a review". In: *Textile Research Journal* 87.8 (2017), pp. 984–1010.

[163] Paul N Stockmann et al. "Biobased chiral semi-crystalline or amorphous high-performance polyamides and their scalable stereoselective synthesis". In: *Nature communications* 11.1 (2020), pp. 1–12.

[164] Alejandro Strachan et al. "Shock waves in high-energy materials: The initial chemical events in nitramine RDX". In: *Physical Review Letters* 91.9 (2003), p. 098301.

[165] Alejandro Strachan et al. "Thermal decomposition of RDX from reactive molecular dynamics". In: *The Journal of chemical physics* 122.5 (2005), p. 054502.

[166] Alexander Stukowski. "Visualization and analysis of atomistic simulation data with OVITO–the Open Visualization Tool". In: *Modelling and Simulation in Materials Science and Engineering* 18.1 (2009), p. 015012.

[167] Huai Sun. "COMPASS: an ab initio force-field optimized for condensed-phase applications overview with details on alkane and benzene compounds". In: *The Journal of Physical Chemistry B* 102.38 (1998), pp. 7338–7364.

[168] Huai Sun et al. "An ab initio CFF93 all-atom force field for polycarbonates". In: *Journal of the American Chemical Society* 116.7 (1994), pp. 2978–2987.

[169] Motowo Takayanagi et al. "Polymer composites of rigid and flexible molecules: system of wholly aromatic and aliphatic polyamides". In: *Journal of Macromolecular Science, Part B: Physics* 17.4 (1980), pp. 591–615.

[170] Masafumi Tasaki et al. "Microscopically-viewed relationship between the chain conformation and ultimate Young's modulus of a series of arylate polyesters with long methylene segments". In: *Polymer* 55.7 (2014), pp. 1799–1808.

[171] Kohji Tashiro and Masamichi Kobayashi. "Theoretical evaluation of three-dimensional elastic constants of native and regenerated celluloses: role of hydrogen bonds". In: *Polymer* 32.8 (1991), pp. 1516–1526.

[172] Kohji Tashiro, Masamichi Kobayashi, and Hiroyuki Tadokoro. "Calculation of three-dimensional elastic constants of polymer crystals. 2. Application to orthorhombic polyethylene and poly (vinyl alcohol)". In: *Macromolecules* 11.5 (1978), pp. 914–918.

[173] Kohji Tashiro, Masamichi Kobayashi, and Hiroyuki Tadokoro. "Elastic moduli and molecular structures of several crystalline polymers, including aromatic polyamides". In: *Macromolecules* 10.2 (1977), pp. 413–420.

[174] Venkat R Thalladi, Markus Nüsse, and Roland Boese. "The melting point alternation in α, ω-alkanedicarboxylic acids". In: *Journal of the American Chemical Society* 122.38 (2000), pp. 9227–9236.

[175] John A Thomas et al. "Multiscale modeling of high-strength fibers and fabrics". In: *Micro- and Nanotechnology Sensors, Systems, and Applications IV*. Vol. 8373. International Society for Optics and Photonics. 2012, 83731S.

[176] Roberto Todeschini and Viviana Consonni. *Handbook of molecular descriptors*. Vol. 11. John Wiley Sons, 2008.

[177] Alan E Tonelli and Jack F Edwards. "Are poly (p-phenylene terephthalamide)(Kevlar®) and other liquid crystalline polymers conformationally rigid?" In: *Polymer* 193 (2020), p. 122342.

[178] Mark A. Tschopp. *Uniaxial Tension*. Last accessed 19 February 2021. 2020. URL: `https://icme.hpc.msstate.edu/mediawiki/index.php/Uniaxial_Tension.html`.

[179] Ahmed Jalal Uddin et al. "Hydration in a new semiaromatic polyamide observed by humidity-controlled dynamic viscoelastometry and X-ray diffraction". In: *Journal of Polymer Science Part B: Polymer Physics* 43.13 (2005), pp. 1640–1648.

[180] Magnus Ullner and Clifford E Woodward. "Orientational correlation function and persistence lengths of flexible polyelectrolytes". In: *Macromolecules* 35.4 (2002), pp. 1437–1445.

[181] Adri CT Van Duin et al. "Development and validation of a ReaxFF reactive force field for Cu cation/water interactions and copper metal/metal oxide/metal hydroxide condensed phases". In: *The Journal of Physical Chemistry A* 114.35 (2010), pp. 9507–9514.

[182] Adri CT Van Duin et al. "ReaxFF: a reactive force field for hydrocarbons". In: *The Journal of Physical Chemistry A* 105.41 (2001), pp. 9396–9409.

[183] Adri CT Van Duin et al. "ReaxFFSiO reactive force field for silicon and silicon oxide systems". In: *The Journal of Physical Chemistry A* 107.19 (2003), pp. 3803–3811.

[184] Dirk Willem Van Krevelen and Klaas Te Nijenhuis. *Properties of polymers: their correlation with chemical structure; their numerical estimation and prediction from additive group contributions*. Elsevier, 2009.

[185] Aniruddh Vashisth et al. "Accelerated ReaxFF simulations for describing the reactive cross-linking of polymers". In: *The Journal of Physical Chemistry A* 122.32 (2018), pp. 6633–6642.

[186] Leo Vollbracht and Teunis J Veerman. *Process for the preparation of poly-p-phenyleneterephthalamide*. US Patent 4,308,374. 1981.

[187] Peijian Wang et al. "Preparation of poly (p-phenylene terephthalamide) in a microstructured chemical system". In: *RSC advances* 5.79 (2015), pp. 64055–64064.

[188] Yang Wang and Yuanming Xia. "The effects of strain rate on the mechanical behaviour of kevlar fibre bundles: an experimental and theoretical study". In: *Composites Part A: Applied Science and Manufacturing* 29.11 (1998), pp. 1411–1415.

[189] Yao-Zong Wang et al. "One-pot synthesis of polyamides with various functional side groups via Passerini reaction". In: *Polymer Chemistry* 4.3 (2013), pp. 444–448.

[190] Zi-Yuan Wang et al. "Precise tracking and modulating aggregation structures of conjugated copolymers in solutions". In: *Polymer Chemistry* 11.22 (2020), pp. 3716–3722.

[191] YXYM Wang and YM Xia. "Experimental and theoretical study on the strain rate and temperature dependence of mechanical behaviour of Kevlar fibre". In: *Composites Part A: Applied Science and Manufacturing* 30.11 (1999), pp. 1251–1257.

[192] Logan Ward et al. "A general-purpose machine learning framework for predicting properties of inorganic materials". In: *npj Computational Materials* 2.1 (2016), pp. 1–7.

[193] Michael R Weismiller et al. "ReaxFF reactive force field development and applications for molecular dynamics simulations of ammonia borane dehydrogenation and combustion". In: *The Journal of Physical Chemistry A* 114.17 (2010), pp. 5485–5492.

[194] Nicole AS White and Henry A Ellis. "Room temperature structures and odd–even behaviour of a homologous series of anhydrous lithium n-alkanoates". In: *Journal of Molecular Structure* 888.1-3 (2008), pp. 386–393.

[195] Malte Winnacker and Bernhard Rieger. "Biobased polyamides: recent advances in basic and applied research". In: *Macromolecular rapid communications* 37.17 (2016), pp. 1391–1413.

[196] Mitchell A Wood, Adri CT Van Duin, and Alejandro Strachan. "Coupled thermal and electromagnetic induced decomposition in the molecular explosive αHMX; a reactive molecular dynamics study". In: *The Journal of Physical Chemistry A* 118.5 (2014), pp. 885–895.

[197] Gang Wu, Koji Tashiro, and Masamichi Kobayashi. "Vibrational spectroscopic study on molecular deformation of polydiacetylene single crystals: stress and temperature dependences of Young's modulus". In: *Macromolecules* 22.1 (1989), pp. 188–196.

[198] Qiuju Wu et al. “Synthesis and characterization of PAn/clay nanocomposite with extended chain conformation of polyaniline”. In: *Polymer* 41.6 (2000), pp. 2029–2032.

[199] Xiawa Wu, Robert J Moon, and Ashlie Martini. “Crystalline cellulose elastic modulus predicted by atomistic models of uniform deformation and nanoscale indentation”. In: *Cellulose* 20.1 (2013), pp. 43–55.

[200] Xiawa Wu, Robert J Moon, and Ashlie Martini. “Tensile strength of Iβ crystalline cellulose predicted by molecular dynamics simulation”. In: *Cellulose* 21.4 (2014), pp. 2233–2245.

[201] HH Yang. *Kevlar aramid fiber*. Wiley, 1993.

[202] Quanpeng Yang et al. “Effect of Aliphatic Chain Length on the Stress–Strain Response of Semiaromatic Polyamide Crystals”. In: *Macromolecules* (2022).

[203] Quanpeng Yang et al. “Molecular Dynamics Simulation of the Stress–Strain Behavior of Polyamide Crystals”. In: *Macromolecules* 54.18 (2021), pp. 8289–8302.

[204] Xinhua Yang, Tao Zhou, and Chuanyao Chen. “Effective elastic modulus and atomic stress concentration of single crystal nano-plate with void”. In: *Computational materials science* 40.1 (2007), pp. 51–56.

[205] Hung-Ju Yen and Guey-Sheng Liou. “Solution-processable triarylamine-based electroactive high performance polymers for anodically electrochromic applications”. In: *Polymer Chemistry* 3.2 (2012), pp. 255–264.

[206] Hung-Ju Yen and Guey-Sheng Liou. “Solution-processable triarylamine-based high-performance polymers for resistive switching memory devices”. In: *Polymer Journal* 48.2 (2016), pp. 117–138.

[207] Dundar E Yilmaz and Adri CT van Duin. “Investigating structure property relations of poly (p-phenylene terephthalamide) fibers via reactive molecular dynamics simulations”. In: *Polymer* 154 (2018), pp. 172–181.

[208] Dündar E Yılmaz. “Modeling failure mechanisms of poly (p-phenylene terephthalamide) fiber using reactive potentials”. In: *Computational Materials Science* 109 (2015), pp. 183–193.

[209] RJ Young et al. “Relationship between structure and mechanical properties for aramid fibres”. In: *Journal of materials science* 27.20 (1992), pp. 5431–5440.

[210] Rui Yu et al. “Molecular dynamics simulation of the mechanical properties of single-crystal bulk Mg 2 Si”. In: *Journal of electronic materials* 41.6 (2012), pp. 1465–1469.

[211] Bin Zhang et al. “MesoDyn simulation study of phase behavior for dye–polyether derivatives in aqueous solutions”. In: *Computational and Theoretical Chemistry* 1091 (2016), pp. 8–17.

[212] Gang Zhang et al. “Effects of a trans-or cis-cyclohexane unit on the thermal and rheological properties of semi-aromatic polyamides”. In: *Polymer Chemistry* 7.1 (2016), pp. 44–53.

[213] Luzheng Zhang et al. “Thermal decomposition of hydrazines from reactive dynamics using the ReaxFF reactive force field”. In: *The Journal of Physical Chemistry B* 113.31 (2009), pp. 10770–10778.

[214] Qing Zhang et al. “Adhesion and nonwetting-wetting transition in the Al/α- Al 2 O 3 interface”. In: *Physical Review B* 69.4 (2004), p. 045423.

[215] Yan Zhao and Donald G. Truhlar. “The M06 suite of density functionals for main group thermochemistry, thermochemical kinetics, noncovalent interactions, excited states, and transition elements: two new functionals and systematic testing of four M06-class functionals and 12 other functionals”. In: *Theoretical Chemistry Accounts* 120.1 (2008), pp. 215–241.

[216] Oleksii S Zhelavskyi and Alexander Kyrychenko. “Atomistic molecular dynamics simulations of the LCST conformational transition in poly (N-vinylcaprolactam) in water”. In: *Journal of Molecular Graphics and Modelling* 90 (2019), pp. 51–58.

[217] Sheng Zhou et al. “Synthesis and characterization of new aramids based on o-(m-triphenyl)-terephthaloyl chloride and m-(m-triphenyl)-isophthaloyl chloride”. In: *Polymer* 109 (2017), pp. 49–57.

[218] Deju Zhu, Barzin Mobasher, and Subramaniam D Rajan. “Dynamic tensile testing of Kevlar 49 fabrics”. In: *Journal of materials in civil engineering* 23.3 (2011), pp. 230–239.

[219] Feihua Zou et al. “Synthesis and properties of novel soluble aromatic polyamides containing 4-aryl-2, 6-diphenylpyridine moieties and pendant fluorinated phenoxy groups”. In: *Journal of Polymer Research* 23.11 (2016), pp. 1–10.

[220] Sonia Zulfiqar, Muhammad Ishaq, and Muhammad Ilyas Sarwar. “Synthesis and characterization of soluble aromatic–aliphatic polyamide”. In: *Advances in Polymer Technology* 29.4 (2010), pp. 300–308.